Vibrational dynamics in semiconductor compounds and alloys

Dissertation
zur Erlangung des akademischen Grades
doctor rerum naturalium (Dr. rer. nat.)

vorgelegt dem Rat der Physikalisch-Astronomischen Fakultät
der Friedrich-Schiller-Universität Jena

von M. Sc. Stefanie Eckner geb. Kosan
geboren am 26.01.1990 in Jena

Gutachter

1. PD Dr. Claudia S. Schnohr (Friedrich-Schiller-Universität Jena)
2. Prof. Dr. Dirk Lützenkirchen-Hecht (Bergische Universität Wuppertal)
3. Prof. Olivier Pagès (Université de Lorraine)

Tag der Disputation: 05.03.2019

Schwingungsdynamik komplexer Verbindungshalbleiter

Viele Materialeigenschaften technisch wichtiger III-V-Halbleiter sind gut erforscht [1, 2]. Allerdings erfordern immer detailreichere Modellierungen von Halbleiterbauelementen auch immer präziseres Wissen über die grundlegenden mikroskopischen Eigenschaften. Von besonderem Interesse sind unter anderem die Kraftkonstanten für Änderungen von Bindungslängen und Bindungswinkeln, welche die lokale Struktur in Mischverbindungen, in Nanopartikeln, und an Grenzflächen bestimmen [3, 4]. Während die Kraftkonstanten binärer Verbindungshalbleiter aus gemessenen makroskopischen elastischen Konstanten berechnet werden können [5, 6], verhindert die gemischte Besetzung der Gitterplätze dieses Vorgehen für die Bestimmung elementspezifischer Kraftkonstanten in ternären Mischverbindungen. Eine Alternative ist in diesem Fall die Ermittlung der elementspezifischen effektiven Kraftkonstanten über temperaturabhängige Messungen der Feinstruktur des Röntgenabsorptionskoeffizienten (extended x-ray absorption fine structure spectroscopy – EXAFS).

In dieser Arbeit wurden die binären III-V-Halbleiter GaP, GaAs, GaSb, InP, InAs, und InSb, sowie die ternären Mischverbindungen (In,Ga)P und (In,Ga)As mithilfe temperaturabhängiger EXAFS-Messungen untersucht. Für die Mischverbindungen wurden die elementspezifischen effektiven Kraftkonstanten für das Strecken und Stauchen der Bindungen als Funktion der Komposition bestimmt. In die Diskussion der Ergebnisse wurden zusätzlich Literaturwerte der II-VI-Mischverbindung Zn(Se,Te) [7] einbezogen. Es ergeben sich unterschiedliche Kompositionsabhängigkeiten für (In,Ga)P auf der einen und (In,Ga)As und Zn(Se,Te) auf der anderen Seite. Interessanterweise zeigen die meisten der sechs untersuchten Bindungsarten (Ga–P, In–P, Ga–As, In–As, Zn–Se, und Zn–Te) die gleiche relative Änderung der Kraftkonstanten als Funktion der relativen Bindungslängenänderung. Darüber hinaus stimmt dieser Verlauf mit den Ergebnissen einer druckabhängigen EXAFS-Untersuchung an CdTe [8] überein. Es konnte damit gezeigt werden, dass die Kompositionsabhängigkeit der elementspezifischen effektiven Kraftkonstanten für das Strecken und Stauchen der Bindungen in ternären Mischverbindungen mit Zinkblende-Struktur hauptsächlich durch die erzwungene Bindungslängenänderung hervorgerufen wird. Die Ladungsumverteilungen und die Änderung der Massenverhältnisse in der Umgebung der Bindung spielen hingegen keine Rolle.

Für die binären Materialien wurden neben der effektiven Kraftkonstante für das Strecken und Stauchen der Bindung auch die effektive Kraftkonstante für die Änderung der Bindungswinkel ermittelt. Beide Kraftkonstanten lassen sich durch jeweils eine Funktion der Ionizität und der reduzierten Masse der Bindung beschreiben. Großer Wert wurde im Rahmen der Auswertung auf eine korrekte Abschätzung aller Ergebnisunsicherheiten gelegt. Die dafür notwendigen umfassenden Testszenarien ermöglichen dabei auch eine Einschätzung der prinzipiellen Möglichkeiten, die temperaturabhängige EXAFS-Messungen zur Bestimmung interatomarer Kraftkonstanten bieten.

Contents

List of Figures

List of Tables

Abbreviations

1NN	first-nearest neighbour
2NN	second-nearest neighbour
AS	Australian Synchrotron
BN	boron nitride
DFT	density functional theory
EDX	energy-dispersive x-ray analysis
EXAFS	extended x-ray absorption fine structure spectroscopy
HASYLAB	Hamburger Synchrotronstrahlungslabor
LO	longitudinal optical
MOCVD	metal organic chemical vapour deposition
MREI	modified random element isodisplacement
NTE	negative thermal expansion
PF	Photon Factory
RBS	Rutherford backscattering spectroscopy
SEM	scanning electron microscopy
SLS	Swiss Light Source
TO	transversal optical
VCA	virtual crystal approximation
VFF	valence force field
XRD	x-ray diffraction

1 Introduction

III-V semiconductors are a technically important material class for electronic and opto-electronic devices [9, 10] such as high-performance transistors [11], light emitting diodes [12], photo-detectors [13–15], nano-lasers [16], high-efficiency solar cells [17–19], and solar water splitting devices [20, 21]. Compared to silicon, III-V semiconductors have the advantage that many material properties, like lattice constants and band gap energies, can be specifically tailored through alloying. In ternary alloys one crystallographic site of the zinc-blende structure is occupied by two different elements. In quaternary alloys both crystallographic sites are mixedly occupied. In most cases the different atom species are randomly distributed on the respective sub-lattice, leading to the formation of random alloys [2]. While many properties of binary III-V compounds and their ternary and quaternary alloys are well known [1, 2], some aspects, like the vibrational behaviour, are still not fully understood.

The thermal vibrations of atoms in a material are governed by the force constants of the interatomic bonds which describe the resistance to stretching and bending of the bond. Stretching and bending of the bond correspond to relative atomic vibrations parallel and perpendicular to the bond direction, respectively. The relative strengths of both types of vibrations are thought to determine whether negative thermal expansion (NTE), which is observed at low temperatures for many III-V semiconductors and other materials crystallising in zinc-blende structure, occurs [22–24]. The bond-stretching and bond-bending force constants also describe the response of the material to static stress and strain. Hence, these force constants play a crucial role for the local atomic structure at interfaces between materials with different lattice constants, in nano-particles, and in random alloys [3, 4]. In order to precisely understand and predict macroscopic properties of interfaces, nano-particles and alloys, substantiated knowledge of the microscopic bond properties, including bond strengths, is thus imperative.

While force constants in compound materials can be determined from their elastic constants [5, 6], this approach fails for random alloys, where several atom species share one crystallographic lattice site. However, element-specific force constants in random alloys are of particular interest, since they determine the local structure of the material, which

in turn heavily influences technically important properties like the band gap energy [4]. A tool to obtain element-specific force constants, even in random alloys, is temperature-dependent extended x-ray absorption fine structure spectroscopy (EXAFS). EXAFS is typically used to study the local structure of materials independently for each atom species. A range of zinc-blende semiconductor alloys were investigated during the last four decades [7, 25–30], revealing the fundamental difference between local atomic and long-range crystallographic structure. In addition to the structural information, temperature-dependent EXAFS studies provide an opportunity to gain information on the vibrational behaviour of the atoms, from which force constants of the interatomic bonds can be deduced. Such temperature-dependent measurements were already performed for a couple of binary III-V and II-VI semiconductors [24, 31–33], yielding effective bond-stretching and bond-bending force constants. However, the differing experimental and data analysis conditions limit the comparability of force constants stemming from different studies. A systematic comparison of the vibrational dynamics in III-V semiconductors therefore needs a homogeneously analysed dataset to disentangle the influence of different material parameters and to scrutinise the trends in force constants, for example with respect to the atom mass ratio or the ionicity of the bond, which are reported in the literature [34]. Only one study in the literature reports temperature-dependent measurements of a ternary alloy, Zn(Se,Te) [7]. Therefore, more experimental investigations of selected random alloys with zinc-blende structure are needed to understand the composition dependence of element-specific effective bond-stretching force constants in these materials. Elucidating this mechanism will also help to make substantiated predictions for other members of this technically important class of materials.

In this work III-V compound semiconductors and their alloys were investigated using temperature-dependent EXAFS measurements to obtain element-specific information of the force constants governing the vibrational behaviour. The two main aspects studied comprise the element-specific effective force constants in ternary alloys and the vibrational anisotropy in binary compounds. The goal of this investigation was to gain insight into the mechanism governing the composition dependence of element-specific effective bond-stretching force constants in ternary semiconductor alloys. The force constants determined here and the force constants predicted based on this knowledge for other materials could then be used to precisely model the structural properties of random alloys in complex semiconductor devices. Additionally, a systematic comparison of the vibrational behaviour in binary III-V semiconductors forms the basis of the search for correlations between the effective force constants of the bonds and other material properties, including

the strength of low-temperature NTE.

This work is structured as follows: In the second chapter, the origin of the fine structure of the x-ray absorption coefficient is explained and the requirements for a successful EXAFS measurement are detailed. A short overview of the data analysis methods currently used in EXAFS studies is given, together with the theoretical description of the effects of thermal vibrations of atoms visible in EXAFS measurements. Chapter three summarises current literature and studies of vibrational dynamics in zinc-blende semiconductors and related material properties. Details of the sample preparation, the sample characterisation, the EXAFS measurements, and the general data analysis are reported in chapter four. Chapter five covers the study of the composition dependence of the element-specific effective bond-stretching force constants in ternary zinc-blende semiconductor alloys. The results are compared to other measures of bond strength, namely Raman mode frequencies and force constants determined from elastic constants. Similarities and differences in the underlying mechanisms driving the composition dependence are discussed. In chapter six, the investigation of the effective bond-stretching and bond-bending force constants in binary III-V compound semiconductors is described. The correlation of force constants and other bond properties, like reduced mass and ionicity, is investigated in detail to elucidate systematic trends. The results are summarised and a brief outlook on possible future research directions is given in chapter seven.

2 Extended x-ray absorption fine structure spectroscopy

The properties of solid materials crucially depend on their atomic structure. Therefore, measurement methods like x-ray diffraction (XRD) studying the crystallographic structure often lay the foundation of a comprehensive sample characterisation needed to correlate new fascinating physical effects with fundamental material properties. However, not all materials exhibit a long-range crystallographic structure and even for those who do, the local short-range structure can be significantly different from it. Hence, experimental methods yielding information about the local structure of materials significantly enrich the portfolio of techniques in basic research. One such method is the extended x-ray absorption fine structure spectroscopy (EXAFS).

EXAFS measures the dependence of the x-ray absorption coefficient on the energy of the incident x-ray photons just above an absorption edge. Since the K-shell absorption edges of most elements lie between a few keV and 100 keV, EXAFS is usually applied in this energy range [35].

In the first part of this chapter the fundamental processes governing the formation of the fine structure of the absorption coefficient are explained and the theoretical description is presented briefly. Consecutively, the experimental implementation and the analysis of the data obtained are described in general. The specific experimental and data analysis details applying to this work are given later on in chapter 4.

2.1 X-ray absorption fine structure

The absorption of radiation passing through a material can be quantified by the absorption coefficient μ. The x-ray absorption process, on which EXAFS is based, is the photoelectric effect. It can occur when the energy of the incoming x-ray photon is high enough to overcome the binding energy of an electron. This gives rise to a sudden increase of the absorption coefficient $\mu(E)$ as a function of photon energy E, which is called the absorption edge. The freed electron travels outwards from the absorbing atom as a wave. Its

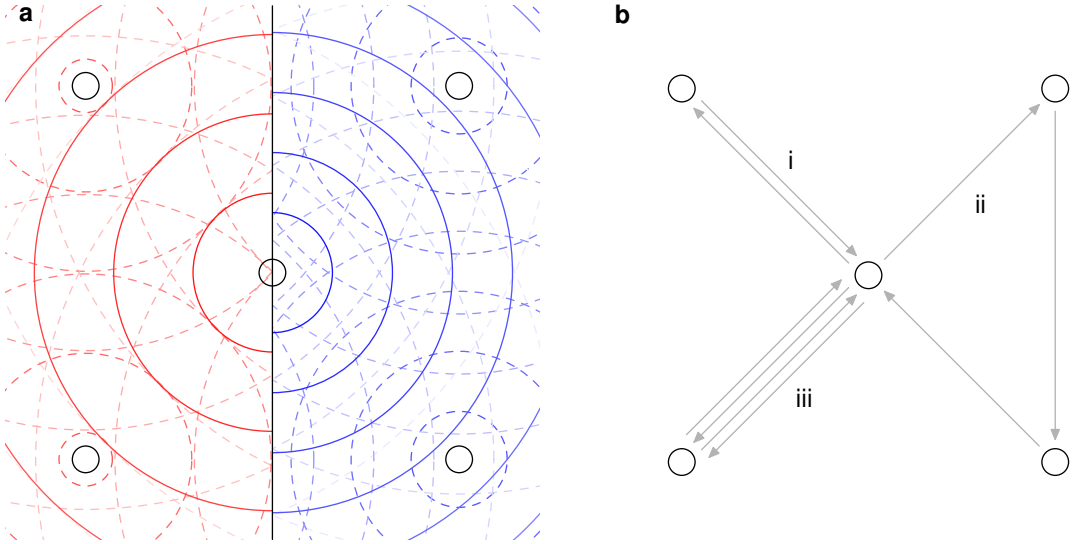

Figure 2.1: Schematic showing the scattering of the photo-electron. **a,** The photo-electron travels outwards as a wave and is scattered at the neighbouring atoms. The superposition of outgoing (solid lines) and backscattered (dashed lines) electron waves leads to constructive or destructive interference at the position of the absorbing atom. Since the occurrence of constructive or destructive interference depends on the wave length (energy) of the electron (left versus right side of panel a), the absorption coefficient changes as a function of photon energy, causing the fine structure above the absorption edge. **b,** Beside the single scattering path including the next nearest neighbour (i), each possible scattering path contributes to the fine structure, including double paths (like iii), triangular paths (like ii), paths to more distant atoms, and paths involving more scattering events. However, the largest contributions come from scattering paths with small lengths and including few scattering events.

wave length depends on the incident photon's energy. If the absorbing atom is embedded in a solid, the electron wave is scattered at surrounding atoms as shown schematically in Fig. 2.1a. The interference of the outgoing and backscattered photo-electron waves leads to the fine structure of the absorption coefficient visible above the absorption edge as shown in Fig. 2.2a. In theory, the fine structure χ(E) is defined through the normalised difference between the absorption coefficient of the embedded absorbing atom with and without the scattering from neighbouring atoms, μ(E) and μ_0(E), respectively.

$$\chi(E) = \frac{\mu(E) - \mu_0(E)}{\mu_0(E)} \tag{2.1}$$

As the absorption coefficient without scattering, μ_0(E), is not accessible experimentally, the fine structure is extracted from the experimentally determined μ(E) using a fitted

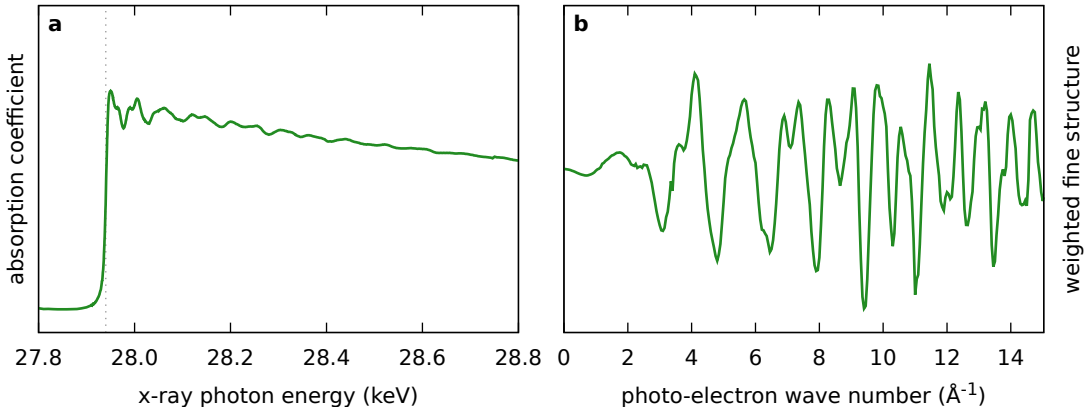

Figure 2.2: X-ray absorption fine structure of the In-K edge measured on InP. a, The x-ray absorption coefficient measured as a function of photon energy shows a characteristic fine structure above the absorption edge. The edge energy is indicated by the dotted grey line. **b,** The fine structure $\chi(k_e)$ extracted from the absorption coefficient $\mu(E)$ in panel a using eqs. 2.2 and 2.3 was weighted with the squared photo-electron wave number k_e^2 to enhance the visibility of the features. The maximum wave number plotted corresponds to the maximum energy shown in panel a.

smooth background curve $\mu_{bkg}(E)$.

$$\chi(E) = \frac{\mu_{exp}(E) - \mu_{bkg}(E)}{\Delta\mu_{exp}} \tag{2.2}$$

The use of the edge step $\Delta\mu_{exp}$ in contrast to the energy dependent $\mu_{bkg}(E)$ in the denominator of this expression ensures that $\chi(E)$ is well defined. However, this approximation leads to a small artificial contribution to the EXAFS Debye-Waller factors also called *McMaster correction* [36–38]. The extracted fine structure is usually displayed as a function of photo-electron wave number k_e as is done in Fig. 2.2b. The relation between k_e and the photon energy E follows from the classical dispersion relation of massive particles as

$$k_e = \frac{1}{\hbar}\sqrt{2m_e(E - E_0)}\,, \tag{2.3}$$

with E_0 indicating the absorption edge energy and m_e being the electron rest mass. Employing Fermi's golden rule, one can relate the distance distribution of neighbouring atoms $\varrho(r)$ with the fine structure $\chi(k_e)$ to obtain the EXAFS equation [36, 37, 39]

$$\chi(k_e) = S_0^2 \sum_j N_j \frac{|f_j(k_e)|}{k_e R_j^2}\, e^{-2R_j/\lambda(k_e)}\, e^{-2k_e^2\sigma_j^2 + \frac{2}{3}k_e^4 C_j^{(4)}}\, \sin\left[2k_e R_j - \frac{4}{3}k_e^3 C_j^{(3)} + 2\delta_c(k_e) + \delta_j(k_e)\right]. \tag{2.4}$$

Here, $f_j(k_e) = |f_j(k_e)|\, e^{i\delta_j(k_e)}$ represents the complex backscattering amplitude, δ_c is the phase shift of the photo-electron wave due to the potential of the absorbing atom, and $\lambda(k_e)$ denotes the energy dependent mean free path of the photo-electron. The amplitude reduction factor S_0^2 covers theoretical and experimental effects reducing the amplitude of the oscillations independent of photo-electron wave number k_e and mean interatomic distance R [36]. The distance distribution $\varrho(r)$ was split up in contributions from different scattering paths j to account for all possible scattering events as sketched in Fig, 2.1b. The distance distribution for each scattering path j was then expanded in cumulants [39, 40] to the fourth order as

$$\int_0^\infty e^{2ik_e r} \varrho_j(r)\, \mathrm{d}r = \exp\left[\sum_{n=0}^{\infty} \frac{(2ik_e)^n}{n!} C_j^{(n)}\right] \tag{2.5}$$

$$= \exp\left[0 + 2ik_e R_j - 2{k_e}^2\sigma_j^2 - \frac{4}{3}i{k_e}^3 C_j^{(3)} + \frac{2}{3}{k_e}^4 C_j^{(4)}\right]. \tag{2.6}$$

The main structural parameters accessible by EXAFS include the mean of the distance distribution $C_j^{(1)} = R_j$ (interatomic distance), the variance of the distance distribution $C_j^{(2)} = \sigma_j^2$, the asymmetry parameter (skewness) $C_j^{(3)}$, and the kurtosis cumulant $C_j^{(4)}$. Since at each absorption edge only one element contributes to the measured signal, the structural information obtained with EXAFS is element-specific. Additionally, EXAFS is very sensitive to the local environment, while no long-range structure is needed. This makes EXAFS a powerful tool complementary to methods probing the crystallographic structure, like XRD.

2.2 EXAFS measurement

After the first theoretical description of the fine structure of the x-ray absorption coefficient in 1971 [41], the new method to gain information about structural properties was rapidly developed and its use facilitated by the dramatically improving technical conditions regarding x-radiation generation and detection [36].

2.2.1 X-radiation sources

EXAFS measurements require a high intensity monochromatised x-ray beam with variable photon energy. Therefore, EXAFS experiments are usually carried out at synchrotron radiation facilities, although laboratory-based instruments have been used succesfully [42].

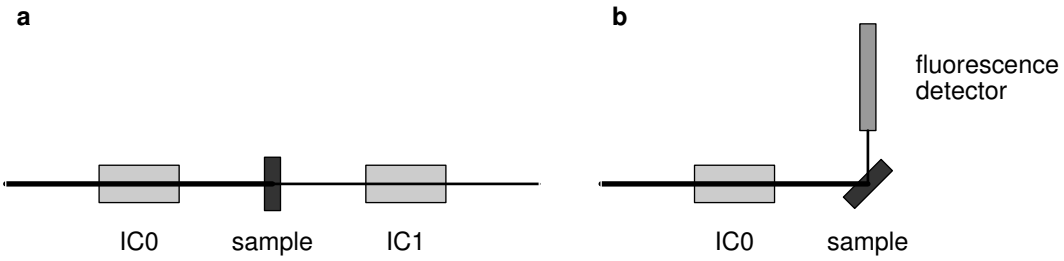

Figure 2.3: Measurement setup for transmission and fluorescence mode. a, In transmission mode the transmitted fraction of radiation is determined using ionisation chambers before (IC0) and after (IC1) the sample. **b,** In fluorescence mode the sample is usually tilted by 45°. The fluorescence radiation is detected perpendicular to the incoming beam.

Synchrotron radiation arises when fast travelling charged particles are forced on a circular path. To use this effect, light particles, in most cases electrons, are circulated in a large storage ring with velocities close to the speed of light. In the simplest case, radiation generated at the bending magnets of the storage ring can be used. The use of insertion devices, i.e. wigglers or undulators, significantly enhances the brilliance of the x-ray beam, which improves the signal-to-noise ratio but may raise requirements on sample stability and homogeneity [36].

To select the x-radiation of a particular energy from the beam with a bandwidth of tens of eV (undulators) to thousands of eV (bending magnets and wigglers) [35] a monochromator is needed. Often a silicon double crystal monochromator, which can be slightly detuned to suppress harmonics of the selected energy, is used. An alternative is a channel-cut monochromator, where the two reflecting planes are perfectly aligned. In this case the suppression of harmonics is achieved by additional x-ray mirrors [35].

In the end, beamlines at synchrotron radiation facilities deliver an energy-tunable x-ray beam with a bandwidth of approximately 1 eV [35].

2.2.2 Measurement modes

The absorption coefficient describes which fraction of the x-ray beam is absorbed in the sample. As the absorption itself is not measurable, it is determined experimentally by the measurement of a related property like transmission, fluorescence or Auger electron yield [36]. In this work, measurements were done partly in transmission and partly in fluorescence mode.

The setup for an EXAFS measurement in transmission mode is sketched in Fig. 2.3a. The intensity of the incoming x-ray beam is detected by an ionisation chamber (IC0) before it

passes through the sample. The transmitted intensity is measured by a second ionisation chamber (IC1) to enable the determination of the attenuation coefficient α according to the Beer-Lambert law

$$I_1 = e^{-\alpha d} I_0, \tag{2.7}$$

where d denotes the sample thickness which is constant for a given sample and geometry. Effects other than photo-absorption at the element under consideration only give slowly varying contributions to $\alpha(E)$. Therefore, the attenuation coefficient can, after suitable background subtraction, be regarded as equal to the absorption coefficient $\mu(E)$.

As an alternative, the fluorescence radiation, occurring when the core hole at the absorbing atom is refilled, can be detected. The setup for fluorescence mode is depicted in Fig. 2.3b. The fluorescence detector usually is positioned perpendicular to the incoming beam to minimise contributions of elastic and inelastic scattering, with the sample tilted by 45° [36].

2.2.3 Requirements for samples

Requirements for samples differ in transmission and fluorescence mode. Samples for EXAFS measurements in transmission mode need to be very homogeneous since lateral inhomogeneities lead to averaging over different sample thicknesses d in eq. 2.7 which distorts the spectrum. Additionally, there exists an ideal sample thickness. If the sample is too thick, very few photons reach the second ionisation chamber increasing the noise of I_1. Furthermore, harmonics of the monochromator may distort the measurement, since they are transmitted through the sample easier than the selected fundamental wave and can therefore contribute significantly to the signal in IC1. If the sample is too thin, the edge step will be small leading to a poor signal-to-noise ratio. Additionally, a thin sample may intensify problems arising from non-homogeneity [36]. The optimal thickness of the sample therefore depends on both the exact beamline setup and the sample material properties, but usually ranges between 0.5 and 2.5 absorption lengths [36], meaning that, above the absorption edge, 40% to 90% of the incoming x-ray beam is absorbed in the sample.

In fluorescence mode, the sample should contain enough of the element under consideration to produce sufficient fluorescence radiation to reach a high signal to noise ratio. On the other hand, if the studied element is the main absorber in the sample, over-absorption can distort the signal considerably, as is discussed in appendix C.6. To optimise both aspects for a given material, the measurement setup shown in Fig. 2.3b can be altered to a

grazing-incident or grazing-exit design [36].

Additional requirements arise from the technical implementation of the measurement. The sample should not be altered by the applied x-ray beam and measurements at defined temperatures are simplified by a good thermal conductivity of the sample [36].

2.3 Analysis of EXAFS spectra

Parallel to the technical development of the measurement method, the quantitative theoretical description and analysis methods for EXAFS spectra greatly improved [37]. This section shortly introduces the two main approaches to EXAFS analysis, namely the ratio method and the path fitting technique. Additionally, the influence of atomic motions on EXAFS spectra is described and the correlated Einstein model, used in this work to study the vibrational properties of semiconductors, is presented.

2.3.1 Ratio Method

Data analysis using the ratio method is based on the assumption that two sufficiently similar EXAFS spectra share the same backscattering amplitude $f_j(k_e)$, phase shift δ_c, and photo-electron mean free path $\lambda(k_e)$ with all differences arising from different distance distributions $\varrho(r)$ [35]. First, the fine structure $\chi(k_e)$ is Fourier transformed into non-phase-corrected radial distance space r. From the resulting $\chi(r)$, one coordination shell sufficiently distant to all other scattering atoms is selected using a window function. The Fourier back-transform than yields a filtered fine structure consisting only of contributions from the chosen coordination shell. This procedure works especially well for the first shell of neighbouring atoms, where the single-scattering approximation is valid [43]. In a second step, the filtered fine structure is split in amplitude and phase to extract the differences in cumulants of the distance distributions.

The logarithm of the amplitude ratio of the filtered fine structures contains information about the even cumulants in the EXAFS equation (eq. 2.4) [35].

$$\ln \frac{|\chi_1|}{|\chi_2|} = \ln\left(\frac{N_1}{N_2}\right) - 2\ln\left(\frac{R_2}{R_1}\right) - 2\frac{R_1 - R_2}{\lambda(k_e)} - 2k_e^2(\sigma_1^2 - \sigma_2^2) + \frac{2}{3}k_e^4(C_1^{(4)} - C_2^{(4)}) \qquad (2.8)$$

Assuming only a small difference $R_1 - R_2$, the term containing the photo-electron mean free path $\lambda(k_e)$ is negligible, enabling a polynomial fit in k_e to determine the cumulant differences $\sigma_1^2 - \sigma_2^2$ and $C_1^{(4)} - C_2^{(4)}$. The difference of the phases of the filtered fine

structures provides the differences of the odd cumulants of the distance distribution.

$$\Phi_1 - \Phi_2 = 2k_e(R_1 - R_2) - \frac{4}{3}k_e^3(C_1^{(3)} - C_2^{(3)}) \tag{2.9}$$

While the ratio method is limited to the analysis of scattering contributions separated in non-phase-corrected radial distance, it has the advantage that no *a priori* knowledge about the structure of the material is necessary. Additionally, it enables precise relative comparisons within one common dataset, since many experimental and data processing errors cancel out when comparing similar spectra [35].

2.3.2 Path fitting

If some information is available about the sample's structure, path fitting provides an alternative procedure to analyse EXAFS data. This analysis approach is independent on the separability of different scattering contributions [44]. Starting point for the path fitting procedure is an educated guess about the structure of the sample material. For this structure, the functions of k_e, that appear in the EXAFS equation 2.4, are calculated for all required scattering paths using programs like FEFF [36, 45]. This theoretical standard is then fit to the data by allowing small variations of the cumulants of the distance distribution and additional parameters like the amplitude reduction factor S_0^2 and the absorption edge energy to provide physically meaningful information about the sample [36].

This mode of analysis has the advantage of yielding absolute values for the cumulants of several scattering paths compared to the relative values for the first shell determined by the ratio method. While the path fitting procedure is in principle independent from experimental references, systematic errors may be reduced when relying only on the comparison of different spectra. As a disadvantage, a good estimate of the structure is needed in the theoretical calculation in order to get meaningful results [36].

2.3.3 Thermal vibration of atoms

Since all electronic processes involved in x-ray absorption are much faster than the atomic motion, EXAFS measurements provide a sum of snapshots of the local configuration of atoms. Therefore, the distance distribution contains not only static disorder but is also broadened by the thermal vibration of atoms. To gain insight into the influence of thermal vibrations on the cumulants of the distance distribution, it is useful to reconstruct the distribution from the average of instantaneous displacements. The instantaneous interatomic

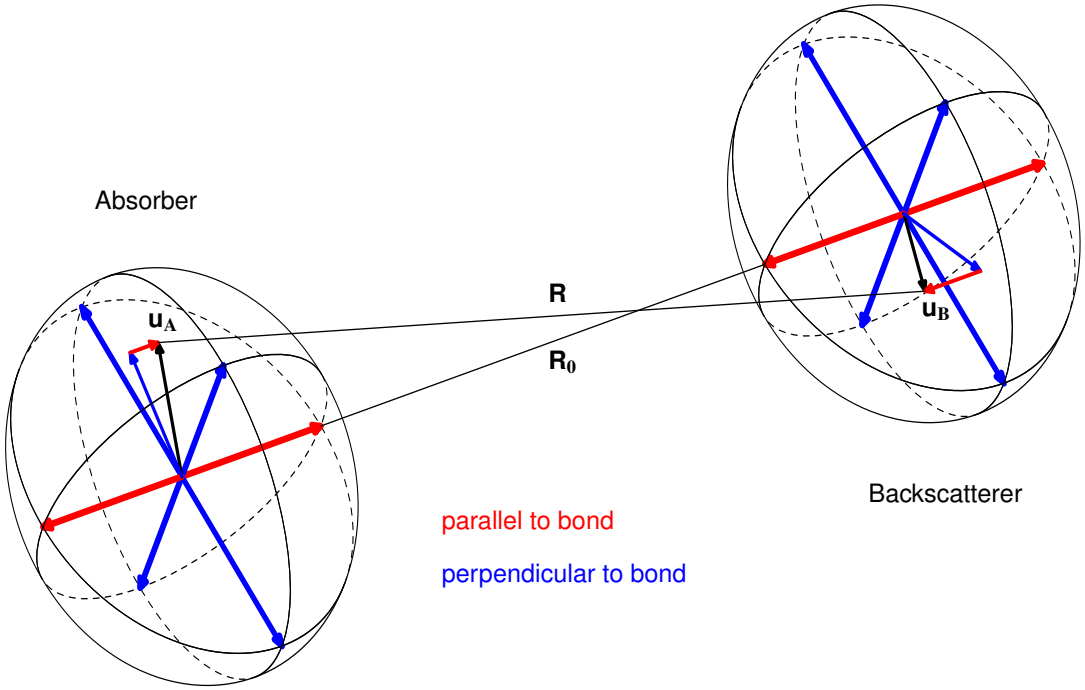

Figure 2.4: Ellipsoids describing the thermal motion of atoms. Both the absorbing and the backscattering atom are displaced from their ideal lattice site. The instantaneous interatomic distance R thus differs from the equilibrium interatomic distance R_0. The distribution of displacements is assumed to be axially symmetric with respect to the bond direction and is therefore visualised by the ellipsoids enclosing the lattice sites. The instantaneous displacements $\mathbf{u}_A$ and $\mathbf{u}_B$ are split in a contribution parallel (red) and a contribution perpendicular to the bond (blue).

distance $\mathbf{R}$ depends on the displacements $\mathbf{u}$ of both the absorber A and the backscatterer B from their respective ideal lattice site [39, 46] as depicted in Fig. 2.4.

$$\mathbf{R} = \mathbf{R_0} + \mathbf{u_B} - \mathbf{u_A} = \mathbf{R_0} + \Delta\mathbf{u} \tag{2.10}$$

Because EXAFS gives information about the interatomic distances in a material, it is convenient to analyse all displacements with respect to the direction of the interatomic distance, i.e. when describing first nearest neighbour relations, with respect to the direction of the bond. The displacements are assumed to be distributed axially symmetric to the bond, leading to the ellipsoids depicted in Fig. 2.4. The difference of instantaneous displacements $\Delta\mathbf{u}$ can thus be split into a contribution parallel and a contribution perpendicular to the bond, $\Delta u_{\parallel}$ and $\Delta u_{\perp}$, respectively, with

$$|\Delta\mathbf{u}|^2 = \Delta u_{\parallel}^2 + \Delta u_{\perp}^2. \tag{2.11}$$

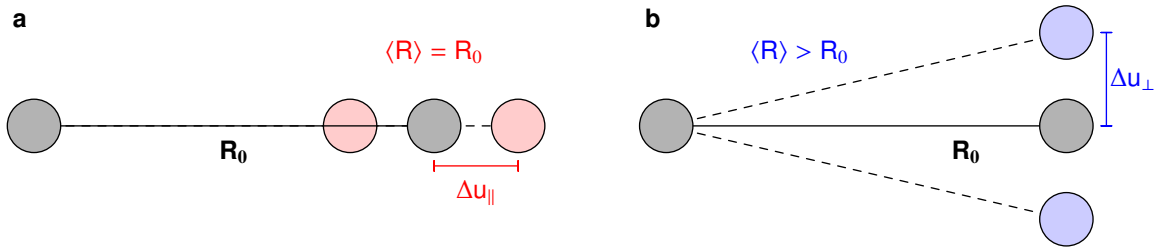

Figure 2.5: Impact of the vibration of atoms on the mean of the distance distribution. a, Vibrations parallel to the bond decrease and increase the interatomic distance, so that the average of the instantaneous distances $\langle R \rangle$ equals the equilibrium distance R_0 for small distortions, where the harmonic approximation is valid. **b,** Vibrations perpendicular to the bond always increase the interatomic distance. Therefore the average of instantaneous distances is larger than the equilibrium distance.

The effect of both contributions is sketched in Fig. 2.5. Using eq. 2.10 and the second degree Taylor polynomial at $\Delta u = 0$ (assumption of $\Delta u \ll R_0$) the absolute value of **R** is then given as [39, 46]

$$R = \left[(R_0 + \Delta u_\parallel)^2 + \Delta u_\perp^2\right]^{\frac{1}{2}} = R_0 \left[1 + \frac{2\Delta u_\parallel}{R_0} + \frac{\Delta u_\parallel^2 + \Delta u_\perp^2}{R_0^2}\right]^{\frac{1}{2}} \tag{2.12}$$

$$\approx R_0 \left[1 + \frac{\Delta u_\parallel}{R_0} + \frac{\Delta u_\perp^2}{2R_0^2}\right] = R_0 + \Delta u_\parallel + \frac{\Delta u_\perp^2}{2R_0}\,. \tag{2.13}$$

The first cumulant of the distance distribution corresponding to the bond length (R_{EXAFS}) can now be expressed using the average of instantaneous displacements and neglecting cross correlations between $u_\parallel$ and $u_\perp$ as [47]

$$R_{EXAFS} = \langle R \rangle \approx R_0 + \langle \Delta u_\parallel \rangle + \frac{\langle \Delta u_\perp^2 \rangle}{2R_0}\,. \tag{2.14}$$

In harmonic approximation $\langle \Delta u_\parallel \rangle$ vanishes, but in actual crystals, with an anharmonic interatomic potential, an anharmonic contribution $\langle \Delta u_\parallel \rangle^{anharm}$ remains [39, 48]. While R_0 corresponds to the minimum of the interatomic potential, the distance between lattice sites expressed in an anharmonic crystal and measurable through XRD is $R_C = R_0 + \langle u_\parallel \rangle^{anharm}$. The difference to eq. 2.14, $\langle \Delta u_\perp^2 \rangle / 2R_0$, is always positive meaning that bond lengths obtained by EXAFS are larger than bond lengths obtained from XRD [48].

The analogue expressions for the higher cumulants of the distance distribution, i.e. the variance σ^2, the asymmetry parameter (skewness) C_3, and kurtosis cumulant C_4, are given

by [47]

$$C_2 = \sigma^2 = \left\langle (R - \langle R \rangle)^2 \right\rangle = \langle R^2 \rangle - \langle R \rangle^2 \approx \langle \Delta u_{\parallel}^2 \rangle - \langle \Delta u_{\parallel} \rangle^2 \tag{2.15}$$

$$C_3 = \left\langle (R - \langle R \rangle)^3 \right\rangle \approx \langle u_{\parallel}^3 \rangle - \langle u_{\parallel} \rangle^3 - 3\langle u_{\parallel} \rangle C_2 \tag{2.16}$$

$$C_4 = \left\langle (R - \langle R \rangle)^4 \right\rangle - 3C_2^2 \approx \langle u_{\parallel}^4 \rangle - 3\langle u_{\parallel} \rangle^4 - 3C_2^2 + 6C_2 \langle u_{\parallel} \rangle^2 - 4\langle u_{\parallel}^3 \rangle \langle u_{\parallel} \rangle \,. \tag{2.17}$$

Since thermal vibrations increase with increasing temperature, the cumulants show a temperature-dependence which can be related to the interatomic potential. A simple yet powerful model for relative atomic vibrations is the correlated Einstein model, which assumes one single vibrational frequency (Einstein frequency ω_E) for each type of bond present in the crystal. In the scope of this model the frequency spectrum is thus approximated by its weighted average. Assuming the interatomic potential as

$$V(R) = V_0 + \frac{k_0}{2}(R - R_0)^2 - k_3(R - R_0)^3 + k_4(R - R_0)^4 \tag{2.18}$$

with the harmonic force constant k_0 and the anharmonic force constants k_3 and k_4, the anharmonic contributions can be considered as small perturbations of the Harmonic oscillator [47, 49]. Formulas describing the temperature dependence of the cumulants up to third or fourth order perturbation can be found elsewhere [47, 49]. Their implementation in the analysis scripts are printed in appendix C.1. The basic temperature dependence of the second cumulant (variance) can already be demonstrated in the harmonic approximation, where the thermal contribution takes the form [46]

$$\sigma^2(T) = \frac{\hbar}{2\mu\omega_E} \coth\left(\frac{\hbar\omega_E}{2k_B T}\right), \tag{2.19}$$

with the Einstein frequency related to the harmonic force constant via the reduced mass of the bond $\mu = (m_A m_B)/(m_A + m_B)$ as $k_0 = \mu\omega_E^2$. This temperature dependence yields finite values at 0 K corresponding to zero-point vibrations. Both the zero-point value and the slope at higher temperatures depend on the Einstein frequency as depicted in Fig. 2.6a. Figure 2.6b shows the effect of including anharmonic contributions to the variance of the distance distribution by a positive k_3.

A relation very similar to eq. 2.19 is valid for the vibrations perpendicular to the bond, the only difference being a factor of 2, because displacements perpendicular to the bond directions happen in a plane, while parallel displacements are projections onto a line [4, 34]. In general, the Einstein frequencies or force constants describing parallel and per-

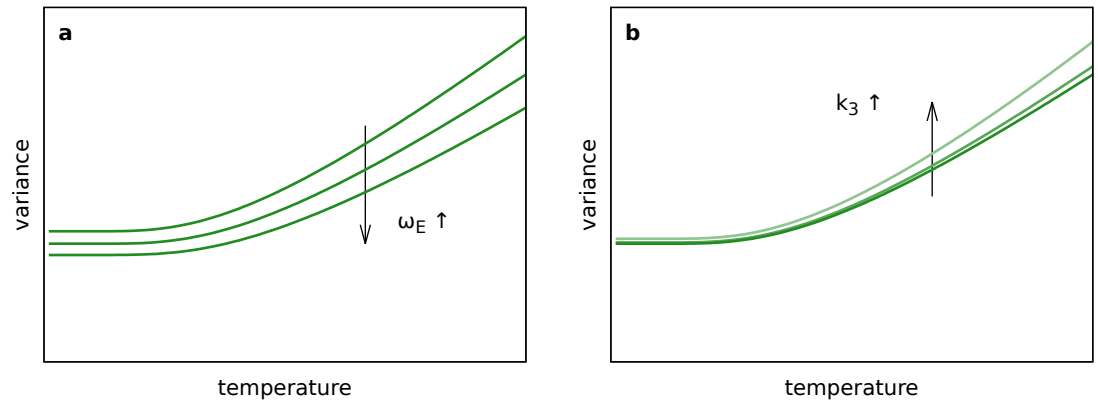

Figure 2.6: Thermal contribution to the variance of the distance distribution using the correlated Einstein model. a, In the harmonic approximation the variance is described by eq. 2.19. Increasing the Einstein frequency ω_E reduces the zero-point values of the variance as well as its slope at higher temperatures. Also, the onset of the rise in variance is shifted to higher temperatures for a larger Einstein frequency. **b,** Additional anharmonic contributions by a positive anharmonic force constant k_3 increase the variance especially at higher temperatures.

pendicular vibrations are not equal. This leads to the ellipticity of instantaneous displacements depicted in Fig. 2.4. To quantify the difference, the anisotropy parameter $\xi = k_{\parallel}/k_{\perp}$ can be defined [50].

3 Properties of zinc-blende semiconductors

In this chapter a short overview of the existing knowledge about the structural and vibrational properties of binary zinc-blende semiconductors and their ternary alloys is given.

3.1 Structural properties

Experimental information about structural properties like lattice constants and bond lengths stems mostly from XRD and EXAFS measurements. Additionally, theoretical calculations are typically applied to search for deviations from common assumptions yet too small in scale for experimental detection.

3.1.1 Crystal structure and lattice constants

In the zinc-blende structure, which is exhibited by many technically important III-V and II-VI semiconductors, every cation is tetrahedrally coordinated by four anions and vice versa (see Fig. 3.1a). Hence, there exists only one bond species in these binary compound semiconductors. The lattice constants vary from 3.616 Å in BN to 6.481 Å in CdTe [1]. While the lattice constants normally increase with increasing temperature, many zinc-blende semiconductors show negative thermal expansion (NTE) below 100 K [1, 23]. The effect is related to atomic vibrations perpendicular to the bond (see Fig. 2.5b) [4, 23, 44, 50], since these can unite increasing mean distances between atoms (bond lengths) with decreasing distances of mean atomic positions (lattice constants). Beside the vibrational anisotropy, the magnitude of NTE depends also on the ionicity of the bonds present in the material [23, 50].

Many III-V and II-VI random ternary alloys crystallise in zinc-blende structure with the lattice constant varying nearly linearly between the binary compounds [2, 4]. Small deviations from this linear behaviour, which is also known as Vegard's law, were predicted theoretically for several alloys [51–54], but the experimental verification remains difficult due to the existing measurement uncertainties in both lattice constant and composition [2, 55]. An overview of existing predictions and experimentally determined deviations from

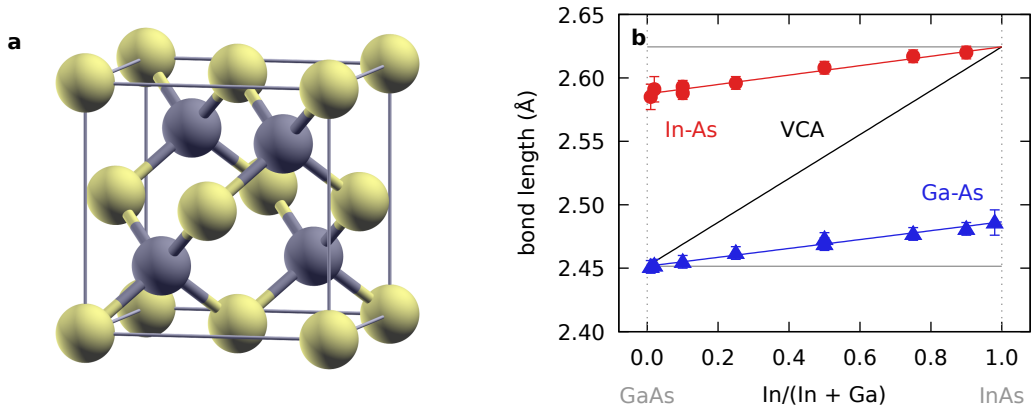

Figure 3.1: Zinc-blende structure and characteristic composition dependence of bond lengths in ternary alloys. a, In the zinc-blende structure every atom is tetrahedrally coordinated by the opposing atom species. **b,** The In-As (red circles) and Ga-As (blue triangles) bond lengths in (In,Ga)As [25] stay close to their respective binary values and deviate significantly from the behaviour proposed by the virtual crystal approximation (black line).

Vegard's law is given in appendix A.

3.1.2 Bond lengths of ternary alloys

In the description of ternary alloys, one simple assumption is the virtual crystal approximation (VCA), where it is assumed that all atoms stay on their ideal lattice site, meaning that all bond lengths are equal and, neglecting vibrational contributions, can be deduced solely from the lattice constant [4]. However, EXAFS studies of ternary zinc-blende alloys show that the bond lengths are nearly constant over the whole compositional range, with the change in the bond lengths amounting only to approximately 20% of the change expected based on the lattice constant [2, 4, 25, 29]. This behaviour is illustrated for (In,Ga)As in Fig. 3.1b and clearly disagrees with the VCA.

To accommodate two bond species with differing bond lengths in the ternary material, the atoms of the species occupying the separate sub-lattice are displaced from their ideal lattice site, while the atoms of species on the shared sub-lattice retain their original positions in good approximation [56]. Therefore, the bond lengths can remain (nearly) unaltered but the bond angles change. This demonstrates that bond bending is energetically favoured over bond stretching in these tetrahedrally coordinated alloy systems, causing the local atomic arrangements to differ fundamentally from the long-range crystallographic structure [4].

3.2 Bond strength and vibrational properties

Besides the bond length, a second important property of an interatomic bond is its strength. As a fundamental parameter it describes the response to static stress and strain as well as the vibrational behaviour of atoms in a material. Different properties are used to describe these different effects of the bond strength, including elastic constants, phonon mode frequencies, and EXAFS force constants. An overwiew of these material properties is given in this section.

3.2.1 Elastic constants and deduced material parameters

Elastic constants of binary zinc-blende semiconductors are usually determined by Brillouin-scattering [2] or sound velocity measurements [57, 58]. Such elastic constants can be related to bond-stretching and bond-bending force constants, α and β, respectively, via valence force field (VFF) models like the Keating potential [5, 59]. These elastic force constants differ from the force constants $k_{\parallel} = k_0$ and $k_{\perp}$ often used in temperature-dependent EXAFS studies (see Fig. 2.5 and eq. 2.18), but similar quantities k_r and k_θ can be derived using [4, 5]

$$k_r = 3\alpha + \frac{1}{2}\beta \tag{3.1}$$

$$k_\theta = \frac{2}{3}\beta\,. \tag{3.2}$$

Force constants α determined from elastic constants of different III-V and II-VI semiconductors decrease with increasing bond length or lattice constant [5, 6], as depicted in Fig. 3.2a and tabulated in appendix A. This bond-length dependence can be described by an empirical law including also the ionic charges of the atoms constituting the material [60]. Under hydrostatic pressure the elastic constants are predicted to increase [61–67]. Some studies are available that measure or predict the composition dependence of elastic constants in ternary zinc-blende alloys [2, 51, 68–76], mostly reporting a parabolic bowing between the values of the binary compounds. From the ternary elastic constants it is possible to calculate effective medium force constants [77] describing the interatomic potential averaged over both bond species.

In VFF calculations of random $In_{0.5}Ga_{0.5}P$ [78] the bond-specific force constants α_{Ga-P} and α_{In-P} show a remarkable inversion with respect to their binary values. According to

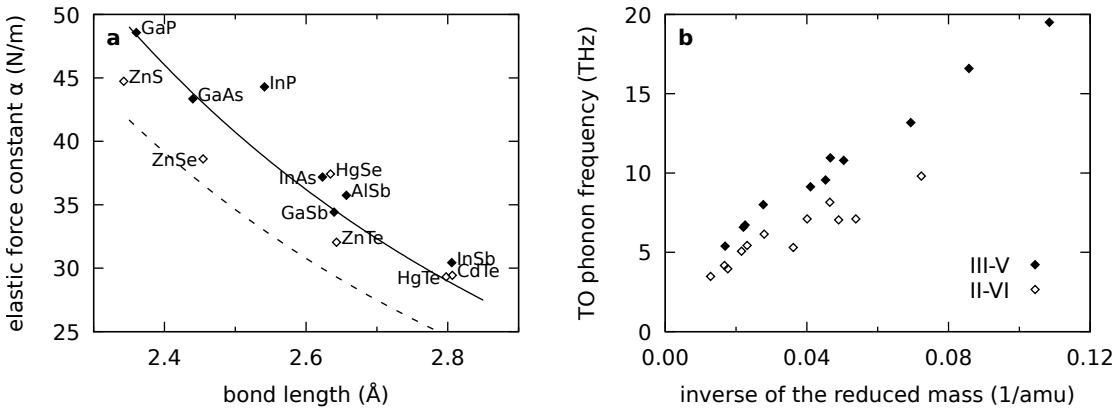

Figure 3.2: Elastic force constants and transversal optical phonon frequencies. a, The force constants deduced from elastic constants of binary III-V (full symbols) and II-VI (open symbols) semiconductors [6] roughly decrease with increasing bond length. This is incorporated in the empirical law proposed for the bond-length dependence of force constants [60] for III-V (solid line) and II-VI (dashed line) materials. **b,** The TO phonon frequencies of III-V (full symbols) and II-VI (open symbols) semiconductors [1] increase with decreasing reduced mass of the constituting bond. While phonon mode frequencies in the literature discussing Raman spectroscopy results are usually given in cm^{-1}, all frequencies in this work will be given in THz for consistency with the Einstein vibrational frequencies from temperature-dependent EXAFS studies.

the theoretical prediction $\alpha_{Ga-P} < \alpha_{In-P}$ in $In_{0.5}Ga_{0.5}P$ while $\alpha_{Ga-P} > \alpha_{In-P}$ comparing the binary parent compounds [78]. Because the focus of that work was the calculation of mixing enthalpies, no explanation is given for this surprising behaviour of the elastic force constants.

3.2.2 Phonon mode frequencies

Phonon mode frequencies at the Brillouin zone center (Γ-point) are accessible by Raman and infrared spectroscopy, while mapping of the phonon modes over the whole Brillouin zone is possible by inelastic neutron scattering [1, 79]. Phonon dispersion curves for a range of III-V and II-VI semiconductors measured by inelastic neutron scattering are available in the literature [80–86]. Their phonon densities of states show strong contributions from optical phonon modes [87, 88].

The frequency of the TO mode at the Brillouin zone center increases with decreasing reduced mass of the bond [1], as depicted in Fig. 3.2b for a number of III-V and II-VI materials. The dependence of the mode frequency on hydrostatic pressure can be described by the Grüneisen relation, where the change of the mode frequency is correlated

to the crystal volume or bond length [1, 89].

$$\gamma_i(\mathbf{q}) = -\frac{V}{\omega_i(\mathbf{q})}\frac{\mathrm{d}\omega_i(\mathbf{q})}{\mathrm{d}V} = -\frac{1}{3}\frac{R}{\omega_i(\mathbf{q})}\frac{\mathrm{d}\omega_i(\mathbf{q})}{\mathrm{d}R} \tag{3.3}$$

The mode Grüneisen parameter $\gamma_\mathrm{i}(\mathbf{q})$ may differ for different modes i and different phonon wave-vectors $\mathbf{q}$. For zinc-blende semiconductors and at the Brillouin zone center ($\mathbf{q} = 0$) the Grüneisen parameter is usually positive for optical phonon modes and often negative for acoustic phonon modes [1]. Hence, when the bond lengths decrease under hydrostatic pressure, optical phonon frequencies increase, while acoustic phonon frequencies decrease.

Raman and infrared spectroscopy studies show that random ternary alloys (A,B)C of zinc-blende semiconductors exhibit different phonon mode behaviours [90–94]. A distinction is drawn between one-mode, two-mode, and mixed-mode behaviour [2]. In one-mode behaviour, both the transversal optical (TO) mode frequency and the longitudinal optical (LO) mode frequency evolve continuously from one binary material to the other. The composition dependence of phonon frequencies is shown schematically in Fig. 3.3a. An example alloy exhibiting this mode type is Zn(Se,Te) [93]. In two-mode behaviour TO and LO mode frequencies of the binary parent material AC shift to one common impurity mode frequency of A-C bonds in a BC crystal, and vice versa, as depicted in Fig. 3.3b. An example is the phonon mode behaviour of (In,Ga)As [93]. If for parts of the compositional range two-mode behaviour is visible while in other parts only a single mode is exhibited, the vibrational behaviour is classified as mixed-mode [2]. This case, which is illustrated in Fig. 3.3c, was reported for (In,Ga)Sb [2].

To predict the phonon mode behaviour of a given ternary alloy, the modified random element isodisplacement (MREI) model can be used [2, 95]. It uses the masses of the constituting atoms to classify the material as exhibiting either one-mode or two-mode behaviour, The classification is based on whether their exists one substituting atom with a mass smaller than the reduced mass of the bond between the remaining elements. If this is the case, the optical phonon frequencies of the two parent compounds are well separated from each other and the alloy shows two-mode behaviour [94]. The MREI model correctly describes the basic properties of many III-V and II-VI semiconductor alloys, but fails to account for some additional features and anomalous intensity evolutions in several materials, like (In,Ga)As and (In,Ga)P [93].

An alternative description is offered by the percolation model, where the (A,B)C crystal is assumed to consist of A-like and B-like regions. These regions exhibit slightly different

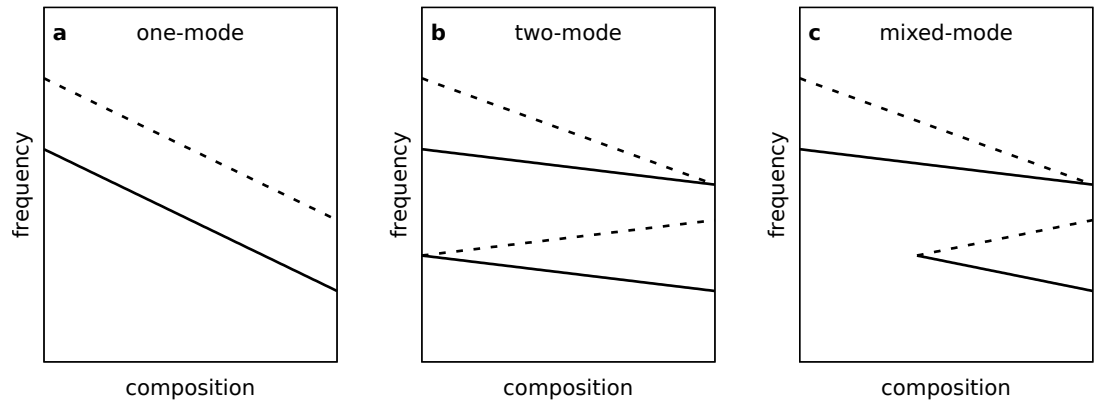

Figure 3.3: Schematic of the different types of phonon mode behaviour in mixed alloys. TO and LO phonon modes are depicted as solid and dashed lines, respectively.

vibrational frequencies due to the influence of differing bond lengths via the Grüneisen relation [93, 94, 96]. Qualitatively, there exist two different regimes concerning the collective vibrations of atoms. Below a critical concentration of the minority bond species, which is called the percolation threshold, these bonds are connected only within finite clusters. Above the percolation threshold, the bonds of the minority bond species are connected throughout the material. This argumentation is valid for both bond species of a ternary alloy. Therefore, as a function of composition, the *normal regime*, where both bond species percolate the material, is surrounded by two *fractal-like regimes*, where one bond-species is confined to finite clusters [93]. At which composition the percolation threshold occurs depends on the crystal structure of the material. For the zinc-blende structure, the critical concentration of minority bonds is 19 % [93].

To describe the TO phonon mode behaviour as a function of composition using the percolation model only few parameters are necessary. These are the bulk and impurity mode frequencies and the parameter Δ, which describes the frequency splitting for one bond species in the A-like and B-like regions. With this, one can reproduce more details of the composition dependence of the TO phonon modes known from experiment than using the MREI model [93].

Both the MREI and the basic percolation model require the knowledge of the impurity mode frequencies as input parameters [93]. However, it is possible to describe the composition dependence of the major Raman mode frequencies with good acurracy using only fundamental properties like bond-length changes and binary bulk phonon dispersion relations, as was shown for (In,Ga)As [92]. The influence of bond-length changes can be calculated using the Grüneisen relation (eq. 3.2.2) [92, 97] with the respective Grüneisen

parameters found in the literature [1]. Additionally, localisation effects play an important role if the collective vibration is confined to one bond species. The change in composition means a reduction of the number of bonds of this given bond species, leading to a spatial confinement of the phonon mode [92]. This spatial localisation is accompanied by a broadening of the mode in reciprocal space, weakening the rule of vanishing phonon momentum normally valid for Raman spectroscopy. The measured frequency is therefore averaged over increasing parts of the Brillouin zone and the description of the composition dependence requires knowledge of the phonon dispersion relation [92, 97]. If the confinement to one bond species is not perfect, coupling effects may influence the frequency further [92].

Since the phonon frequencies are related to bond stretching and bond bending force constants, theoretical calculations of phonon spectra of random alloys may be accelerated when detailed information about the interatomic force constants is available. Force constants calculated *ab initio* for a number of configurations in (Zn,Be)Se and (In,Ga)As show a linear variation with changing bond lengths [98]. Assuming this linear relationship in subsequent calculations of the phonon density of states yields reasonable agreement of this *linearised-force-constants* approach with full *ab initio* calculations [98].

3.2.3 Force constants from temperature-dependent EXAFS studies

Temperature-dependent EXAFS studies, where bond force constants were determined using the correlated Einstein model, can be found in the literature for a range of binary zinc-blende semiconductors [4, 24, 31, 33, 34, 50, 99]. Both the bond stretching and bond bending force constants decrease with increasing ionicity of the bond, while the anisotropy parameter $\xi^{1/2}$ as defined in section 2.3.3 increases with increasing mass ratio of the constituting atoms [44] (see Fig. 3.4). Small differences are found for CdTe, depending on whether the harmonic or anharmonic Einstein model is used [34]. A third possibility is the use of the quasiharmonic analysis, where a harmonic Einstein model is fitted to the thermal contribution to the variance of the distance distribution separately for each temperature, yielding a temperature-dependent quasiharmonic Einstein frequency. However, this approach requires reliable knowledge of the static contribution to the variance. Using the temperature dependence of bond lengths, the change of the quasiharmonic Einstein frequency can be related to the bond length change, defining a bond Grüneisen parameter [34] in analogy to the mode Grüneisen parameter used in Raman spectroscopy (see eq. 3.2.2). The bond Grüneisen parameter determined is constant with increasing temperature and increasing bond length [34].

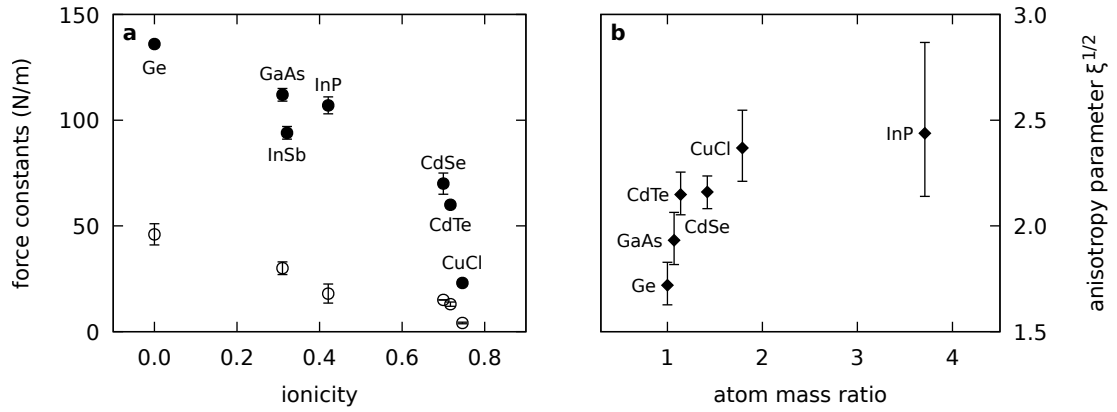

Figure 3.4: Bond force constants of tetrahedrally coordinated materials determined in temperature-dependent EXAFS studies [24, 31–33, 100–103]. **a,** Bond-stretching (full symbols) and bond-bending (open symbols) force constants decrease with increasing ionicity [34, 50]. **b,** The anisotropy parameter increases with increasing mass ratio of the constituting atoms [44, pp. 135–137].

Pressure-dependent EXAFS measurements of CdTe evaluated using the quasiharmonic analysis show an increasing Einstein frequency with increasing hydrostatic pressure [8]. The bond Grüneisen parameter extracted from the relation between Einstein-frequency change and bond-length change, decreases approximately linearly with decreasing bond length [8]. It is interesting to note that the constant-temperature bond Grüneisen parameter and the constant-pressure bond Grüneisen parameter differ substantially in their dependence on the bond length [8]. This can probably be explained through the difference between a bond-length change driven by external stress and a bond-length change resulting from vibrations in the given anharmonic interatomic potential.

In a temperature-dependent EXAFS study of Zn(Se,Te) it is reported, that the Einstein frequencies of both bond species change almost linearly between the binary parent compounds [7], meaning that the frequencies for the Zn-Se and Zn-Te bond are equal for a given composition.

4 Experimental procedure

This chapter describes the experimental methods used, from sample preparation and characterisation, over EXAFS measurements, to the standard data analysis. The customised analysis details are given at the beginning of the subsequent material specific chapters.

4.1 Thin film growth and EXAFS sample preparation

The III-V semiconductors studied in this work comprise the binary materials XY (X = Ga, In; Y = P, As, Sb) and the pseudo-binary alloys (In,Ga)P and (In,Ga)As. All crystallise in the zinc-blende structure with lattice constants ranging from 5.451 Å for GaP to 6.479 Å for InSb [4]. Samples from the binary materials were prepared using commercially available bulk wafers. (In,Ga)P and (In,Ga)As thin films were grown at the Department of Electronic Materials Engineering of The Australian National University Canberra, Australia. Three compositions of (In,Ga)P were grown by metal organic chemical vapour deposition (MOCVD) on GaAs with an intermediate layer of AlAs 50 nm thick. The GaAs substrate showed a miscut of 10 % relative to the (100) direction to avoid ordering of the mixed Ga/In sub-lattice of (In,Ga)P [29]. (In,Ga)As thin films with three different compositions were grown by MOCVD on InP.

The thin films were covered with Apiezon black wax and the AlAs interlayer or the InP substrate was selectively etched using HF(10%) or HCl(32%):H_2O, respectively [29, 104, 105]. The black wax was subsequently rinsed off with trichloroethene. The etching process is depicted schematically in Fig. 4.1. The (In,Ga)P thin film material was diluted with BN and finely ground. The material was then pressed into sample holders and sealed with Kapton tape, yielding samples suitable for EXAFS measurements in transmission mode. Similar BN diluted powder samples were prepared from GaP and InP bulk wafers. The effective thickness amounted to approximately 1.5 absorption lengths 50 eV above the Ga-K edge and approximately 0.5 absorption lengths 50 eV above the In-K edge. The (In,Ga)As material was mixed with graphite and milled in a ball mill for 30 min. The powder was then pressed to pellets with a diameter of 5 mm and a thickness of approximately 1 mm. The effective thickness amounted to approximately 0.1 absorp-

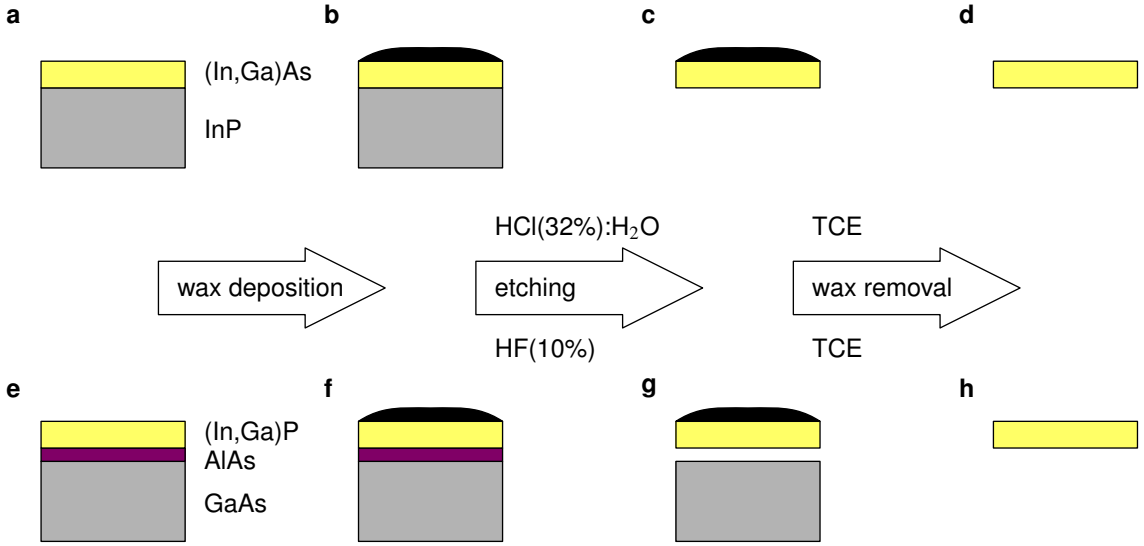

Figure 4.1: Selective etching of substrate or intermediate layer. The (In,Ga)As and (In,Ga)P thin films (a and e) grown by MOCVD were covered with a wax layer for mechanical support (b and f). The InP substrate or the AlAs intermediate layer was removed through selective etching (c and g) using HF(10%) or HCl(32%):H_2O, respectively. After removal of the wax layer (d and h) the resulting thin film material was ground and processed to powder samples suitable for EXAFS measurements.

tion lengths 50 eV above either the Ga- or the In-K edge, i.e. two pellets were prepared for each ternary sample, to facilitate EXAFS measurements in fluorescence mode as required by the beamline setup (see section 4.4). Corresponding graphite diluted powder samples were also prepared from GaAs, InAs, GaSb and InSb bulk wafers.

4.2 Sample characterisation

Prior to the EXAFS sample preparation, the thin films were characterised using Rutherford backscattering spectroscopy (RBS), scanning electron microscopy (SEM) and energy-dispersive x-ray analysis (EDX).

In RBS, light ions are accelerated onto the sample, where they interact with the atoms constituting the material. Resulting backscattered ions are detected as a function of remaining kinetic energy, yielding information about the depth distribution of the different atom species [106]. The backscattering yield may be significantly reduced, when the incoming ions are channelled along a crystallographic axis of the material. Since this channelling is hindered by defects in the material, the comparison of RBS measurements in random and channelling configuration gives information about the crystal quality of the

sample [106]. RBS measurements of (In,Ga)P were carried out at the 1.7 MV tandem accelerator at the Department of Electronic Materials Engineering in Canberra using 2 MeV He^+ ions. The measurements of (In,Ga)As took place at the accelerator JULIA at the Institute of Solid State Physics in Jena using 4 MeV He^{++} ions. Both measurements used a backscattering angle of approximately 170°.

In SEM, a focused electron beam is scanned over the sample and resulting backscattered and secondary electrons are detected. The contrast in backscattered electrons is caused mainly by topography, while the contrast in secondary electrons is mostly due to the sample composition [107]. The accelerated electrons used in SEM imaging can also create a core hole in the electron shell when they impact the atoms of the sample. The characteristic x-radiation emitted when this core hole is refilled can be used with EDX to study the composition of the material [107]. SEM and EDX measurements were performed using a JEOL JSM-6490 and a FEI Helios NanoLab 600i scanning electron microscope at the Institute of Solid State Physics in Jena.

4.2.1 Crystal quality

The crystal quality of the ternary thin films was checked with RBS comparing the spectra recorded in random and channelling configuration. For (In,Ga)As the findings were confirmed by SEM. As an example, the comparison of RBS spectra and SEM images for the samples with nominal In content of 25 % and 50 % is shown in Fig. 4.2. The complete set of RBS spectra and SEM images can be found in appendix B. The (In,Ga)As thin films with nominal In content of 50 % and 75 % show good crystal quality, while the film with 25 % In exhibits significantly poorer crystallinity, as can be seen from both the relatively high backscattering yield in channelling RBS and the extended defects visible in SEM. For (In,Ga)P, the differences between the samples are less pronounced. The films with nominal In content of 50 % and 75 % show somewhat higher crystallinity compared to the film with 25 % In. Since EXAFS measurements probe only the local structure, defects impacting the long-range structure do not impede the EXAFS analysis in this work.

4.2.2 Film thickness and composition

Thickness and composition of the thin films were determined by fitting the random RBS spectra (see appendix B.2 Fig. B.3). An example is given in Fig. 4.3. The composition was also measured by EDX. The resulting values are summarised in Tabs. 4.1 and 4.2. The ratio of group III to group V atoms is equal to one within the measurement uncertainty for

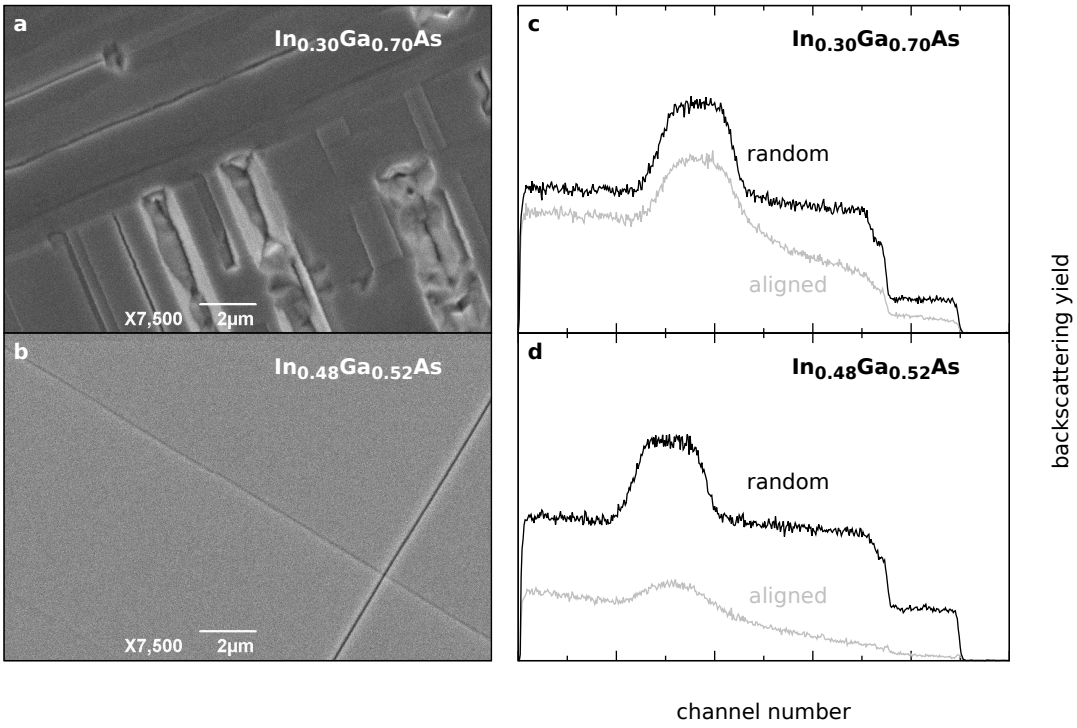

Figure 4.2: SEM and RBS spectra of (In,Ga)As thin films. a-b, In the SEM backscattering electron images significantly more severe defects can be seen for the $In_{0.30}Ga_{0.70}As$ thin film compared to the $In_{0.48}Ga_{0.52}As$ thin film. **c-d,** The lower crystallinity of the $In_{0.30}Ga_{0.70}As$ sample is also visible in the smaller difference between the random and aligned RBS spectra compared to $In_{0.48}Ga_{0.52}As$.

almost all alloys. This would be expected for these materials. The In contents determined with both measurement techniques agree well. The aimed for In content of 50 % was nearly reached for both (In,Ga)P and (In,Ga)As, while the measured compositions for samples of nominally 25 % and 75 % In deviate by up to 11 percentage points consistently for RBS and EDX measurements.

4.2.3 Particle size in the EXAFS samples

The size of the (In,Ga)As particles in the pellets prepared for EXAFS measurements were checked at different spots of the $In_{0.48}Ga_{0.52}As$ pellet using SEM and EDX. An example is shown in appendix B.3 Fig. B.4. The particles with sizes up to 5 µm are distributed homogeneously throughout the pellet. The knowledge of the maximum particle size enables the substantiated estimate of uncertainties arising due to over-absorption in fluorescence mode as detailed in appendix C.6.

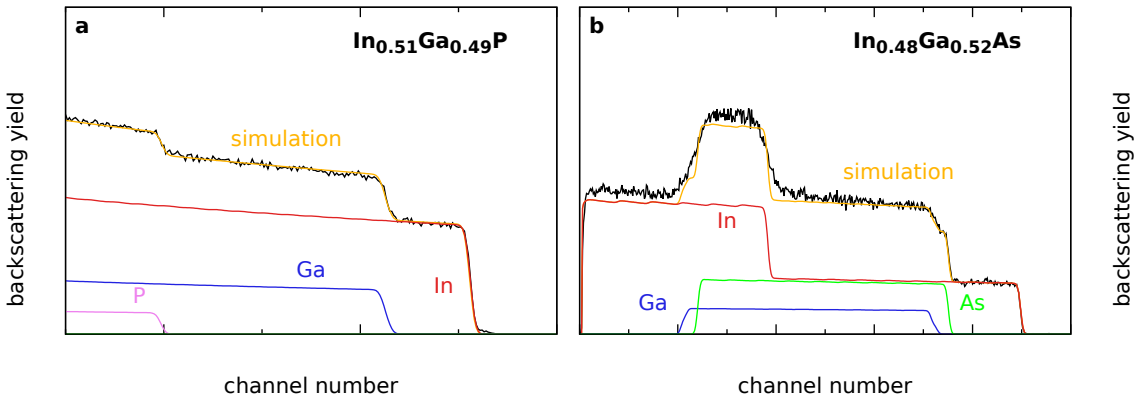

Figure 4.3: Fits to RBS spectra. The random RBS spectra were fitted using the Rump code [39, 108] (panel a) and the *Spektrenverwaltungsprogramm*, written by Ulrich Barth from the Institute of Solid State Physics in Jena, (panel b) to determine the composition and thickness of the thin films. More details are given in appendix B.2.

Table 4.1: Composition of (In,Ga)P thin films determined from RBS and EDX. The layer thickness was determined by RBS. For the second composition the nominal thickness is given, since no thickness could be determined in the fitting procedure of the RBS spectrum [39]. The III to P ratio could not be determined by RBS with a reasonable uncertainty since the mass of the phosphorus atom is small compared to Ga and In leading to a small contribution of P to the backscattering yield.

In/III (nominal)	In/III (RBS)	In/III (EDX)	In/III (combined)	III/P (EDX)	thickness (µm)
0.25	0.34 ± 0.02	0.38 ± 0.03	0.36 ± 0.03	1.00 ± 0.04	0.83 ± 0.01
0.50	0.50 ± 0.02	0.52 ± 0.02	0.51 ± 0.02	1.04 ± 0.04	2.5
0.75	0.70 ± 0.03	0.71 ± 0.02	0.71 ± 0.02	1.06 ± 0.04	0.59 ± 0.01

Table 4.2: Composition of (In,Ga)As thin films determined from RBS and EDX. The layer thickness was determined by RBS.

In/III (nominal)	In/III (RBS)	In/III (EDX)	In/III (combined)	III/As (combined)	thickness (µm)
0.25	0.29 ± 0.01	0.31 ± 0.02	0.30 ± 0.02	1.00 ± 0.04	1.58 ± 0.02
0.50	0.47 ± 0.01	0.48 ± 0.01	0.48 ± 0.02	1.00 ± 0.04	1.82 ± 0.02
0.75	0.64 ± 0.02	0.69 ± 0.01	0.66 ± 0.03	1.03 ± 0.04	1.70 ± 0.02

4.3 EXAFS measurements at HASYLAB

EXAFS measurements of the three (In,Ga)P samples and the binary parent materials GaP and InP were carried out at beamline C of the Hamburger Synchrotronstrahlungslabor (HASYLAB) at DESY in Hamburg, Germany. The absorption spectrum at the Ga-K and In-K edge at 10 367 eV and 27 940 eV [109], respectively, was measured in transmission mode. A Si-111 monochromator and a Si-311 monochromator were used for the Ga-K and In-K edge, respectively. A reference GaAs powder sample or In foil was measured simultaneously with the samples to enable the precise alignment of the edge energy.

The use of a flow-through liquid helium cryostat ensured the stability of the ten temperatures applied in the range between 18 K and 295 K to better than 1 K. The sample temperature was measured with a diode fixed near the sample holder, while the temperature was regulated using a diode near the He entrance. For the samples with low concentration of the absorbing element, several spectra were recorded for selected temperatures to confirm the reproducibility and to enhance the reliability of the results. The Ga edge spectra show edge steps between 0.2 and 0.7, while the In edge spectra yield values just below 0.2 and 0.7 for the ternary alloys and InP, respectively.

4.4 EXAFS measurements at SLS

The three (In,Ga)As samples and the binary materials GaAs, InAs, GaSb and InSb were measured at the SuperXAS beamline of the Swiss Light Source (SLS), Villigen, Switzerland at nine or ten different temperatures between 35 K and 298 K. Additionally, measurements of GaP and InP were carried out at three different temperatures to ensure the reproducibility of the results compared to the measurements at HASYLAB. A Si-111 channel-cut monochromator and a Si-311 channel-cut monochromator were used for the Ga-K and In-K edge, respectively.

Due to the cryostat setup, low temperature measurements at SuperXAS are only possible in fluorescence mode and without recording a reference spectrum. The sample holder is cooled via a cold finger which consists of a massive copper block. The temperature of the sample was measured using a diode mounted on the sample holder. The reproducibility of the measurements was confirmed by recording several spectra for selected temperatures, especially for samples with low concentration of the absorbing element.

4.5 Additional data of binary materials

Additional data series of GaP, GaAs and GaSb measured at the Australian Synchrotron (AS) in Melbourne were provided by Prof. Mark C. Ridgway from the Australian National University in Canberra, Australia. The datasets comprise eight to ten temperatures between 20 K and 295 K, and were measured in transmission mode.

Data of InP measured in transmission mode at the Photon Factory (PF), Japan, [39] was reevaluated to attain maximum comparability between the different materials and slightly differing analysis settings and to critically evaluate the capabilities and limitations of temperature-dependent EXAFS measurements.

4.6 EXAFS data analysis

The data was analysed using the program Larch [110] and self-written plugins for energy calibration and to efficiently deal with temperature-dependent data series. The edge energies of the measured spectra were aligned via the calibration plugin. It uses the Bragg equation to add a small offset to the monochromator angle in order to minimise the differences near the edge for the reference spectra or the sample spectra for transmission or fluorescence measurements, respectively. For each sample, one low-temperature spectrum was calibrated to the tabulated edge energy of 10 367 eV or 27 940 eV for the Ga-K edge or the In-K edge, respectively. To determine the edge position in the spectra, the Larch function *find_e0*, which searches for the maximum derivative, was used. All other spectra of this sample and edge were then aligned to the calibrated low-temperature spectrum.

Normalisation and background subtraction of the aligned spectra were done using the standard functions provided by Larch. The influence of the relevant parameters (edge energy e0, cut-off distance rbkg and spline clamp parameters nclamp, clamp_lo, clamp_hi) was tested by varying these parameters and evaluating the resulting change in the path fitting results.

For Fourier transformation a hanning window with tapering parameter dk=2 was used as the standard case. For fitting, the multiple kweight feature of Larch with values 2, 3, and 4 was used. The start of the window kmin was usually set at 3 Å^{-1} with the end kmax selected according to the visible data quality. All window parameters were varied to test the reliability of the results. Special care was given to the upper bound kmax which is known to have significant effect if leaking of higher shell contributions occurs [111].

Fitting was done in non-phase-corrected radial distance space. The hanning window function with a standard tapering parameter of dr=0.5 was positioned according to the position of the relevant peaks.

The model of the scattering paths was based on the zinc-blende structure with lattice constants known from the literature [1]. Up to the first twelve scattering paths as calculated by FEFF9 [45] without amplitude restrictions (cw=0) were used. For the ternary alloys, the lattice constant corresponding to the binary parent material was used, since the bond lengths are known to change only slightly over the whole compositional range [4, 25, 29]. Therefore, the model employed for the analysis of the Ga edge spectra used the lattice constants of the respective Ga compound, while for the In edge spectra the value of the respective In compound was used. In the FEFF input file some cations were substituted in order to calculate the parameters for equivalent Ga- and In-containing scattering paths. These paths were than weighted according to the composition of the ternary sample. Up to the first three scattering paths were parameterised with one set of free parameters each (bond length, variance, asymmetry parameter and kurtosis cumulant). All remaining paths were parameterised by one common set of free parameters using geometric considerations.

First, the data was fitted with free structural parameters for each measured temperature to check that the variance shows a temperature dependence describable by the Einstein model. Later on, variance, asymmetry parameter and kurtosis cumulant were restricted to the anharmonic correlated Einstein model [47] to reduce the number of free parameters and include the occurring correlations in the final result. The reduced mass of the bond used in the model calculations was assumed to equal the value of an isolated bond although the bond studied is embedded in the crystal. The validity of this assumption was confirmed for (In,Ga)As and is discussed in appendix C.7. The path model was varied through different restrictions of parameters, different numbers of included paths and different numbers of terms for the Einstein model formulas (see appendix C.1) to estimate the influence of the assumptions made. Analysis of the first scattering path using the ratio method was done for comparison. The uncertainties of the final values were estimated considering all varied settings and parameters which amounted to 150 to 5000 tests per sample.

To give an overview over the whole set of fits, the fit results are presented as a function of the *R*-factor, which is defined as [36]

$$R = \frac{\sum_{i=1}^{N} (data_i - fit_i)^2}{\sum_{i=1}^{N} (data_i)^2}. \tag{4.1}$$

Smaller R-factors indicate better fits, but strictly speaking, the R-factors of fits with differing Fourier transformation ranges, differing fitting ranges, or differing numbers of free parameters are not comparable. However, the R-factor is used in the figures only as parameter to spread out the results, with the additional advantage of rejecting fits with unreasonable fit quality parameters.

5 Investigation of ternary alloy systems

In this chapter, the procedure to obtain element-specific effective bond-stretching force constants from the (In,Ga)P data measured at HASYLAB and the (In,Ga)As data measured at SLS is detailed. The composition dependence of the force constants in (In,Ga)P and (In,Ga)As is then discussed taking into account literature data of Zn(Se,Te) [7], so that a comprehensive picture of the vibrational properties of ternary zinc-blende alloys can be formed.

5.1 Analysis of (In,Ga)P data

The spectra were aligned using the simultaneously measured reference spectra with the approach detailed in section 4.6. As an example, the fine structure measured at the Ga-edge for $In_{0.51}Ga_{0.49}P$ and the corresponding Fourier transforms are shown in Fig. 5.1 together with the window functions used in the analysis. An example for the In-edge spectra can be found in appendix C.3.

5.1.1 Parametrisation of the scattering paths

Due to the small mass of the phosphorus atom in comparison to Ga and In, EXAFS spectra of (In,Ga)P feature large second shell contributions. This necessitates the inclusion of higher shell scattering paths in the path fitting model to avoid the corruption of the first shell results through leaking of higher shell contributions [111]. The first twelve scattering paths were used as detailed in section 4.6.

In the restriction of the second and third cumulants using the correlated Einstein model only the terms up to first order were used, since the fit including higher order contributions did not converge reliably for the ternary alloys. The fourth cumulant was set to zero in the standard fit, but the influence of different values of a quartic force constant, defining the fourth cumulant using the first order terms of the correlated Einstein model, was tested. For the binary parent materials a comparison between models including different numbers of terms for the second, third, and fourth cumulant was done.

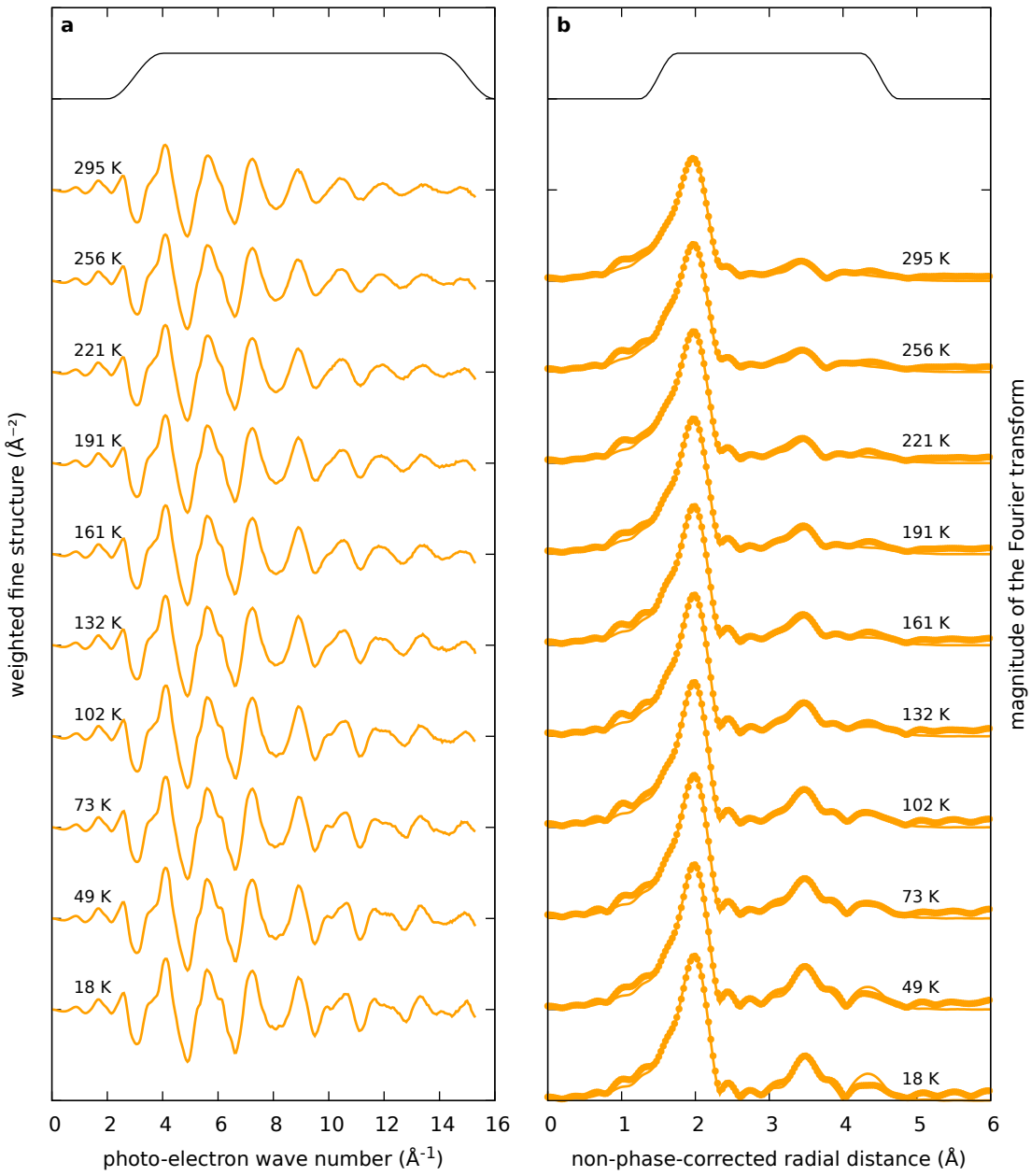

Figure 5.1: Ga-edge spectra of $In_{0.51}Ga_{0.49}P$. Multiple spectra were recorded at selected temperatures. **a,** The fine-structure was weighted with the squared photo-electron wave number to enhance the visibility of the features. The window function used for the subsequent Fourier transformation is shown at the top of the panel. **b,** The magnitude of the Fourier transform resulting from the spectra in panel a (symbols) are compared to the fit of the temperature series using the correlated Einstein model (lines). The fitting range is indicated at the top of the panel.

To account for the uncertainties of the measurement temperature, the temperature used in the Einstein model calculations was varied. In a first test case the assumed sample temperature was increased by the difference between the two temperature sensors which have different distances to the sample, i.e. low temperatures experience a larger shift than high temperatures. In this case the bond-stretching force constants did not change compared to the use of the directly measured temperature values. In a second test, all temperatures were increased by 5 K. This led to an increase in bond-stretching force constants by between $2\,\mathrm{N\,m^{-1}}$ and $3\,\mathrm{N\,m^{-1}}$. The compositional trends under study are therefore unaffected by small uncertainties regarding the measurement temperature.

The amplitude reduction factor S_0^2 and the energy offset E_0 were varied freely per sample, since the differences between some samples were larger than the individual fit uncertainties reported by Larch, which amounted to approximately 0.03 and 0.2 eV, respectively.

5.1.2 Effect of different parameter settings

During the variation of analysis settings and model parameters the values obtained for the bond stretching force constants stayed within the range given by Larch as the fitting uncertainty of an individual fit in almost all cases. This is visible in Fig. 5.2 where the bond stretching force constant obtained for each fit is depicted as a function of the fit quality parameter (R-factor resulting from the Larch fitting routine). The error bars plotted are the individual fit uncertainties from Larch.

When using higher order terms of the anharmonic correlated Einstein model to fit the binary materials data the bond stretching force constants increase. However, the error bars estimated by Larch triple. This can be seen in panels d and e of Fig. 5.2 as several data points at approximately $115\,\mathrm{N\,m^{-1}}$ to $120\,\mathrm{N\,m^{-1}}$ and $135\,\mathrm{N\,m^{-1}}$, respectively. Single high-lying points resulting from successful anharmonic fits of the ternary alloys are also visible in panels c and f. Such an increase by 5 to 10 % when including anharmonic contributions is in agreement with the effect of anharmonicity reported in an EXAFS study of CdTe [34]. There, an increase of the Einstein vibrational frequency by approximately 5 %, corresponding to an increase of the force constant by approximately 10 %, was observed.

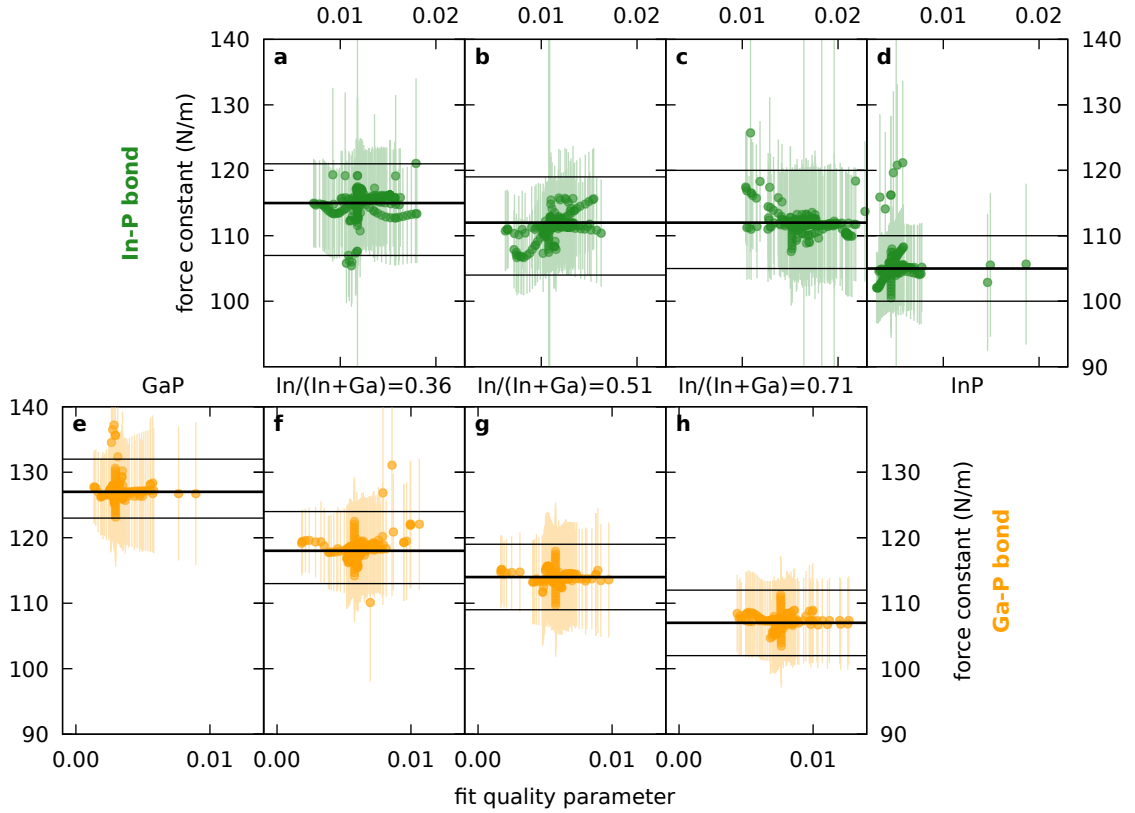

Figure 5.2: Uncertainties of force constants in (In,Ga)P. The In–P and Ga–P effective bond stretching force constants obtained from more than 300 fits per sample and absorption edge, testing different analysis settings and parameters, are plotted as a function of the fit quality parameter R. Smaller R-factors identify better fits. The thick line shows the force constant obtained from one particular setting which gave good fit results for all samples at one absorption edge. The thin lines indicate the minimum and maximum values as estimated from the whole set of tests.

5.2 Analysis of (In,Ga)As data

Since no reference spectra could be recorded simultaneously with the measured samples due to the measurement setup at SLS, the sample spectra were aligned directly with the approach detailed in section 4.6. As detailed below, a Hf decontamination of the Ga-edge spectra was necessary before normalisation and background subtraction. An example for In-edge and decontaminated Ga-edge spectra can be found in appendix C.3.

5.2.1 Correction of Hf contamination

In the preparation of the (In,Ga)As pellet samples an unexpected high abrasion of the zirconium dioxide balls occurred during the milling process. Since neither zirconium nor oxygen interfere with a measurement of the Ga-K or In-K edge this was deemed to not pose a problem for the experiments. However, a common contaminant in zirconium minerals is hafnium [112] and the zirconium dioxide balls used in the milling did contain a non-negligible amount of hafnium that had not been specified by the manufacturer. Therefore, the pellets were contaminated with small amounts of hafnium. This was noticed only during the EXAFS measurements at the SLS where the contamination could neither be removed from the pellets nor avoided by preparing a new set of pellets. Consequently, the samples had to be measured as prepared although the Hf leads to a visible absorption edge (Hf-L_2 edge, 10 739 eV [109]) in the EXAFS region of the Ga-K edge (10 367 eV [109]) as shown in Fig. 5.3.

To eliminate the influence of the Hf edge on the analysis, the data points forming the white-line of the edge were removed. The remaining small step was subtracted from the raw spectrum as a fraction of the Ga edge step. Since the ratio of Hf to Ga content is constant for a given sample, all spectra of one sample were processed using the same edge step ratio with the Ga-K edge step obtained from the LARCH *pre_edge* function. The ratio was determined by minimising the structure below 2 $\mathrm{\AA}^{-1}$ in the Fourier-transformed fine structure spectra χ(R) and confirmed by the comparison of Hf white-line heights of different samples. While the white-line of the Hf-L_2 edge is prominent in the $In_{0.66}Ga_{0.34}As$ spectra, it is significantly smaller for $In_{0.30}Ga_{0.70}As$ and $In_{0.48}Ga_{0.52}As$. For GaAs it is barely visible. This trend is well reproduced in the edge step ratios summarised in Tab. 5.1. The general trend with composition is consistent since a decreasing Ga content does increase the Hf to Ga concentration ratio leading to a higher Hf to Ga edge step ratio. The increase is not linear, because the abrasion significantly increased during the sequence of sample preparation. In succession were prepared: (GaP,) GaAs, (GaSb,),

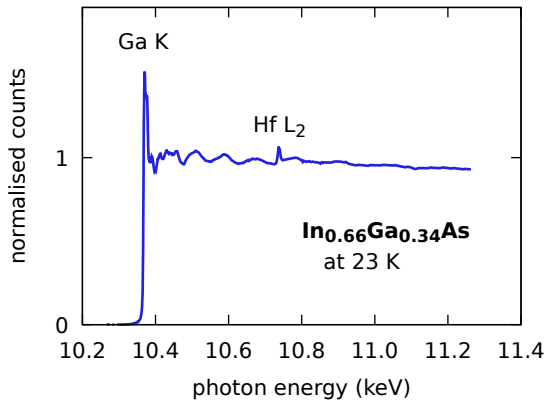

Figure 5.3: Hf-L_2 absorption edge. The white-line of the Hf-L_2 edge is clearly visible in the Ga-K edge spectra of $In_{0.66}Ga_{0.34}As$.

Table 5.1: Hf edge step ratio. The edge step ratio (Hf L_2 to Ga K) was determined from all spectra of a given sample. The uncertainties were estimated from visual inspection of the χ(R) spectra.

Sample	edge step ratio
GaAs	0.000 ± 0.002
$In_{0.30}Ga_{0.70}As$	0.006 ± 0.003
$In_{0.48}Ga_{0.52}As$	0.003 ± 0.002
$In_{0.66}Ga_{0.34}As$	0.026 ± 0.005

$In_{0.48}Ga_{0.52}As$, $In_{0.30}Ga_{0.70}As$, and $In_{0.66}Ga_{0.34}As$; which excellently explains the sequence of the edge step ratios. The influence of the edge step ratio on the analysis was checked by varying the value within double the uncertainties given in Tab. 5.1.

5.2.2 Parametrisation of the scattering paths

Only the first scattering path was used for the analysis of the (In,Ga)As data, since the contributions from the second and higher shells are smaller than for (In,Ga)P. The validity of the single path model was checked by a small step variation of the upper bound of the Fourier transformation window (kmax) described in section 5.2.3. First, the variance of the distance distribution was left free per temperature, to confirm the applicability of the correlated Einstein model for all samples and both absorption edges. Subsequently, the variance was restricted to the Einstein model using the Larch function *sigma2_eins*. The results were confirmed by tests using the cumulant functions detailed in appendix C.1. Fits using anharmonic contributions of order two and higher did not converge reliably for the ternary alloys. In contrast to the results for (In,Ga)P, the use of anharmonic contributions in the analysis of GaAs and InAs does not increase the bond stretching force constants significantly. As for (In,Ga)P, the amplitude reduction factor S_0^2 was varied freely per sample. An overview of the values for S_0^2 for the complete set of tests can be found in appendix C.4. The E_0 differences between the (In,Ga)As samples are just within the individual fit uncertainties. Therefore, E_0 was fixed at the average value of all spectra for a given absorption edge. The influence of this fixed value was studied in subsequent tests.

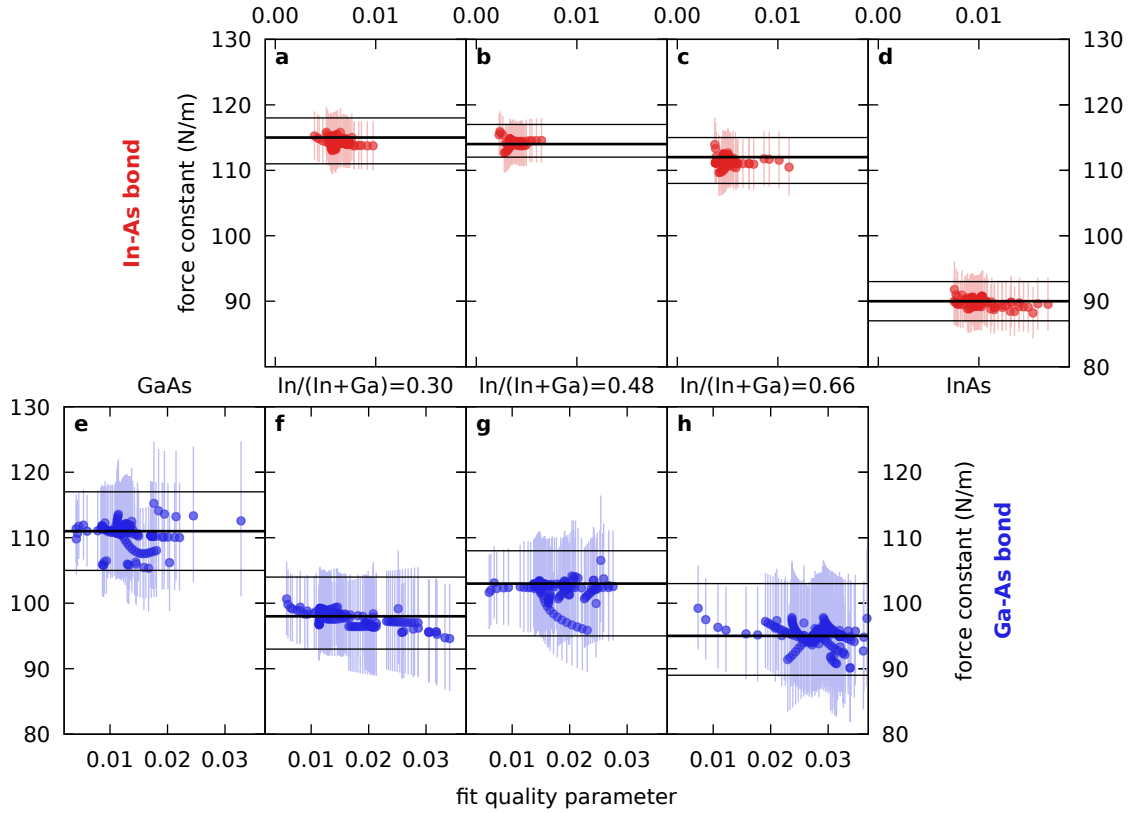

Figure 5.4: Uncertainties of force constants in (In,Ga)As. The In–As and Ga–As effective bond stretching force constants obtained from more than 150 fits per sample and absorption edge, testing different analysis settings and parameters, are plotted as a function of the fit quality parameter R. The thick line shows the force constant obtained from one particular setting which gave good fit results for all samples at one absorption edge. The lines indicate the minimum and maximum values as estimated from the whole set of tests.

5.2.3 Effect of different parameter settings

As is visible in Fig. 5.4, nearly all variations of the bond-stretching force constants determined by different fits of one sample stayed within the individual fit error bars. An undulation when varying the upper bound of the Fourier transformation window (kmax), potentially stemming from the leaking of higher shell contributions [111], was visible only for InAs. However, the amplitude is much smaller than the individual fit uncertainties. The edge step ratio used for correction of the distortion caused by the Hf L_2 edge has significant influence on the force constants determined. Restriction of the edge step ratio values to within double the uncertainties given in Tab. 5.1 confines the variations to the size of the individual fit uncertainties. In Fig. 5.4 fits from analysis settings using edge step ratios farther away are not shown.

5.3 Element-specific effective bond-stretching force constants

For both alloy systems the element-specific bond lengths, as depicted in Fig. 5.5, show good agreement with the values found in the literature [25, 29, 39]. The uncertainties were determined as described above for the bond stretching force constants and are mostly smaller than or similar to the size of the symbols. The figures C.6 and C.7 showing the summary of all test results for the bond lengths can be found in appendix C.4. While the determination of the alloy bond lengths was not the focus of this work, reasonable bond length values are demanded to prove the reliability of the path fitting model. This is confirmed in Fig. 5.5 where especially the change of the bond lengths with alloy composition reported in the literature is well reproduced by the present study while small differences in the absolute values may easily stem from different choices of the analysis settings and path parametrisation.

The element-specific effective bond-stretching force constants determined for (In,Ga)P and (In,Ga)As are summarised in Tabs. 5.2 and 5.3 and plotted in Fig. 5.6. For GaAs and InP, the values of 111 $\mathrm{N\,m^{-1}}$ and 105 $\mathrm{N\,m^{-1}}$, respectively, are in excellent agreement with previous EXAFS studies reporting 112 $\mathrm{N\,m^{-1}}$ [33] and 107 $\mathrm{N\,m^{-1}}$ [31]. The force constants determined from elastic constants [5] (open symbols in Fig. 5.6) are 10 to 20 % larger than the EXAFS force constants. This behaviour is known from the literature [4, 31, 33] and might result from the fact that elastic constants characterise the static response to stress and strain while temperature-dependent EXAFS measures dynamic properties.

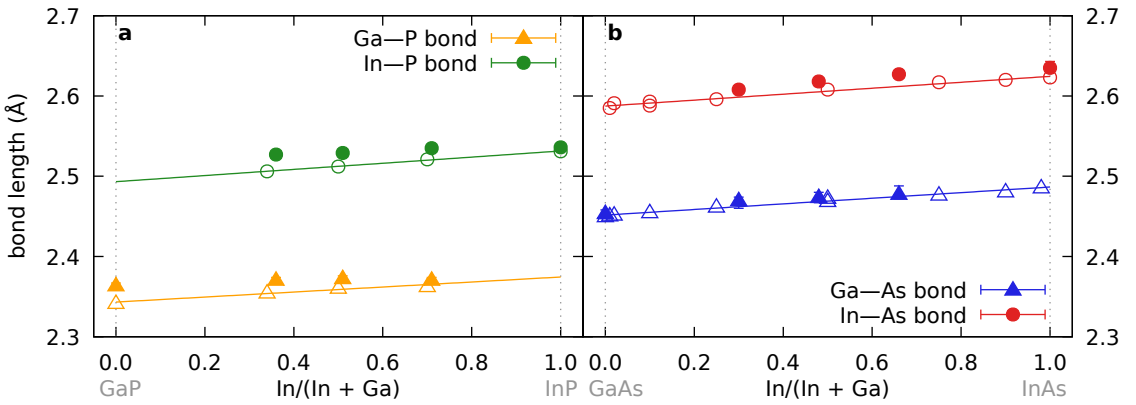

Figure 5.5: Composition dependence of bond lengths. a, The bond lengths determined for (In,Ga)P at 18 K (full symbols) are slightly larger than the literature values at 20 K [29, 39] (open symbols). **b,** The bond lengths of (In,Ga)As at 62 K (full symbols) agree well with the literature values at 77 K [25] (open symbols). The solid lines are the linear curves best fitting the literature data.

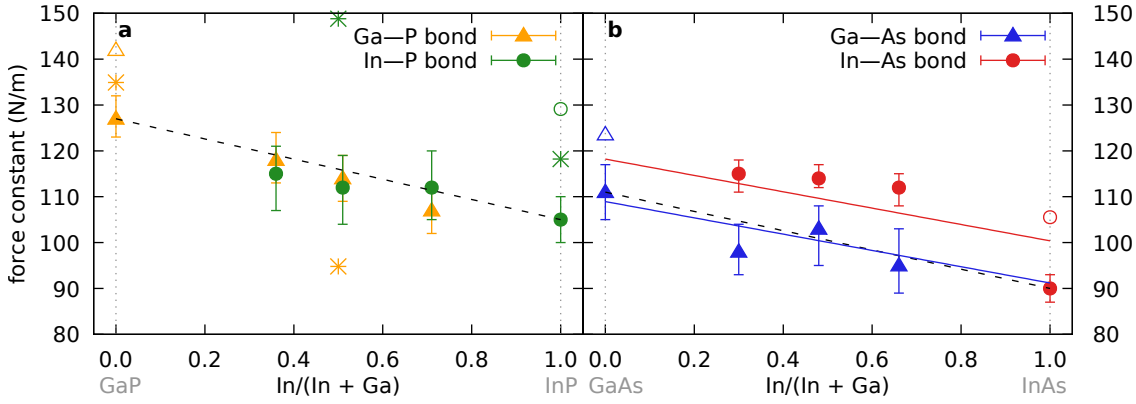

Figure 5.6: Composition dependence of bond stretching force constants. The element-specific bond stretching force constants (solid symbols) are shown as a function of composition for **a,** (In,Ga)P, and **b,** (In,Ga)As. The force constants 3α calculated from elastic constants [5] (open symbols) are shown for comparison. Theoretical predictions for the force constants in (In,Ga)P [78] are added as stars in panel a. Theoretical predictions for ternary (In,Ga)As [98] are plotted as solid lines in panel b.

Table 5.2: Element-specific effective bond stretching force constants in (In,Ga)P. All values are given in $\mathrm{N\,m^{-1}}$. Best, minimum and maximum values refer to the thick and thin lines in Fig. 5.2, respectively.

	k_{Ga-P}			k_{In-P}		
	best	min	max	best	min	max
GaP	127	123	132	-	-	-
$In_{0.36}Ga_{0.64}P$	118	113	124	115	107	121
$In_{0.51}Ga_{0.49}P$	114	109	119	112	104	119
$In_{0.71}Ga_{0.29}P$	107	102	112	112	105	120
InP	-	-	-	105	100	110

Table 5.3: Element-specific effective bond stretching force constants in (In,Ga)As. All values are given in $\mathrm{N\,m^{-1}}$. Best, minimum and maximum values refer to the thick and thin lines in Fig. 5.4, respectively.

	k_{Ga-As}			k_{In-As}		
	best	min	max	best	min	max
GaAs	111	105	117	-	-	-
$In_{0.30}Ga_{0.70}As$	98	93	104	115	111	118
$In_{0.48}Ga_{0.52}As$	103	95	108	114	112	117
$In_{0.66}Ga_{0.34}As$	95	89	103	112	108	115
InAs	-	-	-	90	87	93

5.4 Composition dependence of bond-stretching force constants

It is important to note, that all bond stretching force constants experimentally accessible are *effective* bond stretching force constants describing the bond embedded in the crystal. Therefore, a change of the effective force constant can be caused by a variation of the intrinsic properties of the bond or by a differing embedding. Additionally, while the intrinsic force constants of an isolated bond are identical whether describing a static or a dynamic response, the interaction of a matrix with an embedded bond may differ substantially for the two cases. Temperature-dependent EXAFS measurements therefore yield effective force constants describing the dynamic (vibrational) properties of the material.

In this section, the composition dependence of EXAFS bond-stretching force constants and possible explanations for the trends observed are discussed. The most obvious reference points for the bond-stretching force constants in ternary alloys are the force constants

of their binary parent materials. Therefore, the behaviour of the force constants in ternary alloys with respect to the binary values and their difference is detailed in subsection 5.4.1. Subsequently, the relationship between bond strength and bond length is studied in section 5.4.2 by comparing the composition dependence of EXAFS bond-stretching force constants to the bond-length dependence of elastic force constants determined in binary compounds. However, elastic force constants describe a static property of the material. Therefore, some effects which might influence the composition dependence of EXAFS force constants (for example stemming from the mass disorder) can not occur for elastic constants.

To gain insight into these dynamic effects, the behaviour of the EXAFS bond-stretching force constants is compared to trends observed for TO phonon mode frequencies in section 5.4.3. Facilitating this comparison, the force constants are converted to Einstein vibrational frequencies. A direct analogy between these Einstein vibrational frequencies and the TO phonon mode frequencies determined with Raman spectroscopy is the use of a Grüneisen parameter to describe their bond-length dependence. The idea of a bond Grüneisen parameter characterising the bond-length dependence of Einstein vibrational frequencies is used in section 5.4.4 to compare the composition dependence observed for ternary alloys to the effect of hydrostatic pressure reported in the literature. In the course of the discussion, coupling between the vibrations of the different bond species emerges to influence some bond species. The effect is difficult to quantise, but some qualitative explanatory approaches are studied in section 5.4.5. A short summary of the discussion is given in section 5.4.6.

5.4.1 Bond-strength inversion

The bond stretching force constants of all four bond species show a marked dependence on composition. For Ga–P, In–P, and Ga–As, they show reasonable agreement with the linear interpolation of the binary values (black dashed lines in Fig. 5.6). In contrast, the In–As force constants exhibit a drastic and clearly non-linear composition dependence. Consequently, the effective element-specific bond-stretching force constants of ternary (In,Ga)As in Fig. 5.6b show a remarkable bond strength inversion, where the originally stiffer bond in the binary material becomes the softer bond in the alloy, and vice versa. Such an inversion was predicted for (In,Ga)P by a generalised VFF model fitted to *ab initio* calculated formation energies [78] and is plotted in Fig. 5.6a as stars. However, the EXAFS data of (In,Ga)P exhibits a less pronounced composition dependence, compared to the theoretical prediction, so that no bond strength inversion is observed. Since the

focus of that theoretical work was on the formation energies of the alloys rather than their force constants [78], no explanation is given for this drastic composition dependence. The difference to the EXAFS data might also be due to the VFF model describing static behaviour.

A simple condition for the inversion to occur is that the composition dependence of the force constants is large, while the difference for the binary parent materials remains relatively small. This is, of course, just a generic description with little predictive power, since the composition dependence of force constants needs to be known and might be directly related to the bond strength difference of the binary materials.

5.4.2 Comparison between bond-stretching force constants, elastic force constants, and *ab initio* calculations

Since the elastic force constants of binary zinc-blende compounds show a clear dependence on the bond length [60] (see section 3.2.1 and Fig. 3.2) it stands to reason to depict the element-specific bond-stretching force constants as a function of bond length r. This is done in Fig. 5.7a. The binary values (full symbols) are well described by a r^{-3} dependence (solid black line) similar to the empirical law for elastic force constants. In contrast, the ternary force constants show a much stronger bond length dependence.

The bond strengths of both bond species in turn determine the bond lengths which are exhibited in the alloy system [4, 113]. This can lead to small deviations of the lattice constant from the linear interpolation between the binary values (Vegard's law), if the bond-stretching force constants of the two bond species present in the material are considerably different [51]. Hence, one would expect a small upward bowing of the lattice constant as a function of composition for (In,Ga)As, while no bowing is expected for (In,Ga)P. Such a bowing for (In,Ga)As was reported from molecular dynamics calculations [51] and density functional theory (DFT) calculations [114]. However, other calculations report downward bowing [52] or no bowing [115]. Experimental studies detected no bowing within measurement uncertainty [116, 117]. Consequently, the composition dependence of lattice constants can not be used to confirm the relation of the element-specific effective bond-stretching force constants determined in this work. Nevertheless, an overview of existing theoretical and experimental studies covering the deviation of lattice constants from Vegard's law in III-V and II-VI semiconductor alloys can be found in appendix A.

For ternary (In,Ga)As exists an *ab initio* finite-displacements calculation [98], where a linear relationship between the bond stretching force constant of an individual bond with

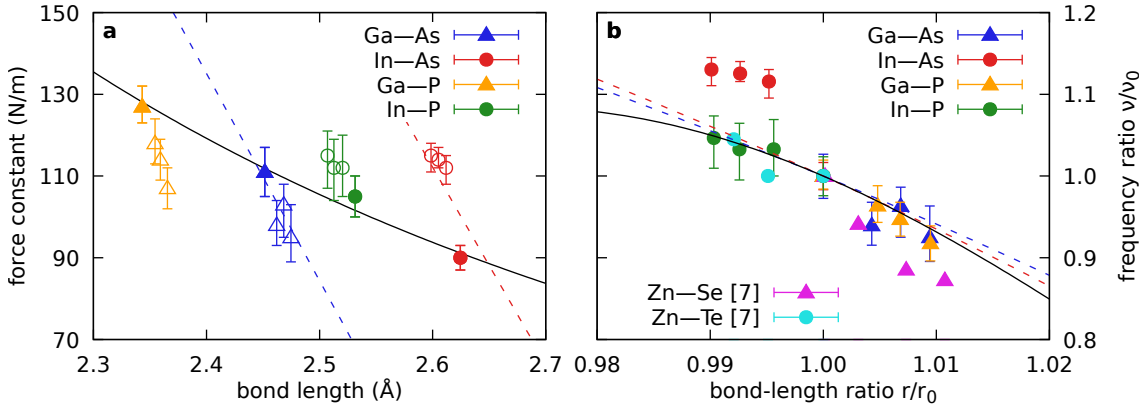

Figure 5.7: Bond length dependence of force constants and vibrational frequencies. **a,** The bond stretching force constants of the binary materials (solid symbols) decrease with increasing bond length. The data is well described by a r^{-3}-dependence (black line). The ternary materials (open symbols) show a clear deviation from this best fitting line. Theoretical predictions for bond stretching force constants in (In,Ga)As [98] are added as blue and red dashed lines. **b,** The change of the Einstein frequency as a function of the change in bond lengths is depicted using the respective ratios to the binary values r_0 and ν_0. From pressure-dependent EXAFS measurements of CdTe a linear dependence of the bond Grüneisen parameter from the bond length was reported [8]. The solid black line then results from the assumption, that this linear relationship is valid for both elongation and compression of the bond. The dashed lines indicate the slope of the dashed lines in a.

its individual bond length is found. The relationship is identical for $In_{0.19}Ga_{0.81}As$ and $In_{0.81}Ga_{0.19}As$ [98]. Using the linear interpolated average element-specific bond lengths given in Fig. 5.5, the resulting composition dependence is plotted in Fig. 5.6b as solid lines. The agreement is good for the Ga–As bond and reasonable for the In–As bond in the ternary alloy. The value for InAs does not fit on this line, which is also visible in Fig. 5.7a where the proposed bond-length dependence is added as coloured dashed lines. The strong difference between InAs and the ternary materials is not easily explainable. The calculation was only done for ternary alloys [98] but the average In–As bond length in InAs is within the range of individual bond lengths in the alloys studied there. This indicates that the vibrational behaviour can differ substantially between binary and ternary materials.

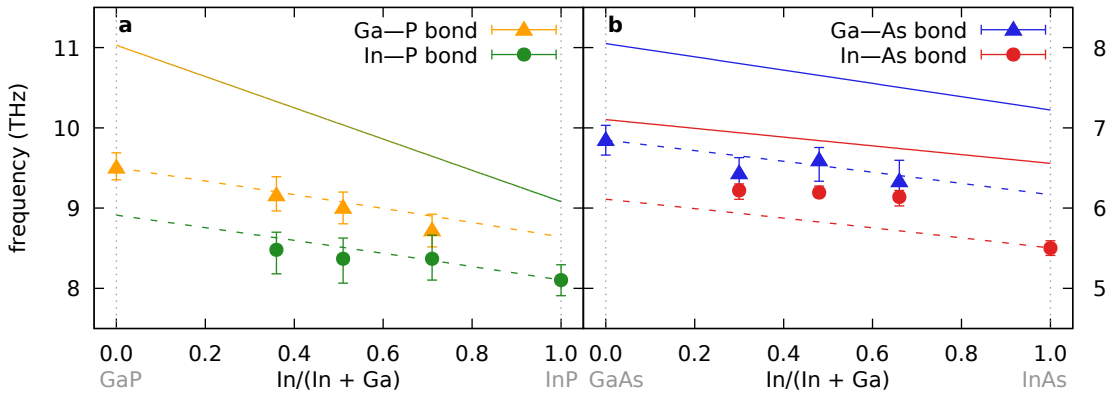

Figure 5.8: Composition dependence of vibrational frequencies. The element-specific Einstein vibrational frequencies (solid symbols) are shown as a function of composition for **a,** (In,Ga)P, and **b,** (In,Ga)As. The coloured dashed lines show the assumption of linearly changing force constants (black dashed lines in Fig. 5.6). The Raman TO frequencies as generated from the MREI scheme [92, 93, 118] are added for comparison as solid lines.

5.4.3 Comparison between Einstein vibrational frequencies and TO phonon mode frequencies

The discussion up to now focused on the change of the intrinsic properties of the bond itself. It is, however, possible that part of the change in effective force constants is caused by the alteration of the bonds surroundings leading to a change of the collective vibrational behaviour. To compare the EXAFS results to other measures of such collective vibrations like Raman and IR spectroscopy, it is useful to calculate the Einstein vibrational frequencies from the bond stretching force constants as detailed in section 2.3.3. The resulting vibrational frequencies in (In,Ga)P and (In,Ga)As are plotted in Fig. 5.8. Since the conversion depends on the reduced mass of the bond, different bonds with the same bond stretching force constants may exhibit different vibrational frequencies. This is visible for (In,Ga)P, where the force constants of Ga–P and In–P bonds in Fig. 5.6a are very similar for a given composition, while the Einstein frequencies in Fig. 5.8a differ considerably. Similarly, the black dashed lines describing linearly changing force constants in Fig. 5.6 transform to the element-specific colored dashed lines in Fig. 5.8.

For comparison the dominant Raman TO mode frequency of (In,Ga)P [93, 118], showing one-mode behaviour, and both bond-specific Raman TO mode frequencies of (In,Ga)As [92, 93], showing two-mode behaviour, are shown as solid lines. The comparison of this single mode phonon frequencies with the Einstein vibrational frequencies requires great care, since the Einstein frequency is a weighted average over the whole phonon spectrum,

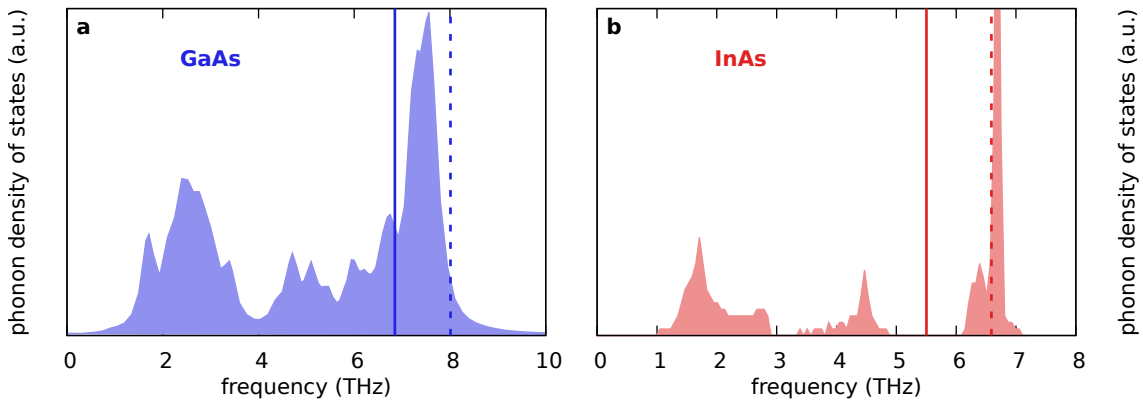

Figure 5.9: Calculated phonon density of states in GaAs [119] and InAs [87]. As common for III-V semiconductors, the phonon densities for GaAs and InAs show pronounced contributions from optical modes. The Brillouin zone center TO phonon mode frequency indicated by the dashed line roughly matches the maximum in phonon density of states for both compounds. The Einstein vibrational frequencies determined with EXAFS are marked by the solid lines.

therefore including optical as well as acoustic phonon modes over the complete Brillouin zone. Consequently, the Raman TO mode frequencies in Fig. 5.8 are larger than the Einstein vibrational frequencies. As an example, the phonon densities of states for GaAs and InAs, together with the Einstein vibrational frequencies and the TO phonon mode frequencies, are depicted in Fig. 5.9.

Additionally, the element-specific Einstein vibrational frequencies of (In,Ga)P differ from each other, while the TO phonon modes show one-mode behaviour, and the element-specific Einstein vibrational frequencies of (In,Ga)As are nearly equal despite the two-mode behaviour visible for the TO phonon modes. Concerning the composition dependence, the fact, that all frequencies decrease with increasing In content, is almost the only agreement between Einstein vibrational frequencies and TO phonon mode frequencies.

Due to their fundamentally different nature, only some of the effects observable in the composition dependence of Raman mode frequencies described in section 3.2.2 apply to Einstein vibrational frequencies. For the description of the Raman mode behaviour, the bond-length dependence according to the Grüneisen relation and the phonon localisation when approaching the dilute limit of one bond species [92, 93, 97] are important. Additionally, mode coupling might occur [92].

Phonon localisation effects in Raman measurements of semiconductor alloys arise due to the broadening of the phonon mode in reciprocal space in response to its spatial confinement in real space [97]. This mechanism does not apply to Einstein vibrational frequen-

cies which always contain contributions from the whole reciprocal space, but other mechanisms may change the relative vibration of neighbouring atoms detected by temperature-dependent EXAFS. For instance, the movement of one bonding partner could get restricted if other neighbours of this atom can not oscillate with the frequency of the bond under consideration due to a large difference in the reduced mass or bond-stretching force constant of the different bond species [120]. However, whether localisation effects are decisive for the composition dependence of Einstein vibrational frequencies can not be established at this point.

5.4.4 Application of the Grüneisen relation to Einstein vibrational frequencies

The bond-length dependence of Raman mode frequencies is described by the Grüneisen relation, where a mode specific, bond-length independent Grüneisen parameter is the proportionality factor between bond-length change and frequency change [92, 93]. Therefore, single mode frequencies show a linear dependence on the bond length of the material. The Grüneisen relation can also be applied to Einstein vibrational frequencies with the difference, that the bond Grüneisen parameter is bond-length dependent, as was reported in a pressure-dependent EXAFS study of CdTe [8]. There, the bond Grüneisen parameter increases linearly with increasing bond length ratio. To study the relationship between frequency changes and bond length changes, the frequency ratio and bond-length ratio related to the respective binary values are plotted in Fig. 5.7b.

For Zn(Se,Te), there exists a temperature-dependent EXAFS study [7], where the alloys were investigated over the whole compositional range. The measurements were carried out in transmission mode in the temperature range from 10 K to 300 K using powder samples diluted with cellulose and BN [7]. The temperature dependence of the variance of the distance distribution was fitted using a harmonic correlated Einstein model and the Einstein vibrational frequencies for the Zn–Se and Zn–Te bonds are reported to vary almost linearly between the binary values [7]. However, no numerical values are given. Therefore, the element-specific effective bond-stretching force constants of Zn(Se,Te) were extracted from Fig. 4 in [7], which shows the fitted temperature-dependence of the variance. The values plotted for the Zn–Se and Zn–Te bond in Fig. 5.7b thus miss the errorbars. No other temperature-dependent EXAFS studies of ternary zinc-blende alloys could be found in the literature.

It is conspicuous, that most data points in Fig. 5.7b form one common curve, excep-

tions being the In–As and the Zn–Se bond. Strikingly, pressure-dependent EXAFS measurements of CdTe [8] (solid black line) yield the exact same relationship between the two ratios. The similarity between the effect of alloying and application of hydrostatic pressure indicates, that the response of the bond to a bond length change forced by its surrounding does not depend on the cause of this external stress. A large part of the composition dependence of bond-stretching force constants is therefore caused by this forced change of the bond length.

The deviations visible for In–As and Zn–Se stem mostly from the difference between the binary material and the ternary alloy nearest to it in composition. In contrast, the differences between the ternary alloys are in agreement with the slope of the CdTe curve. This behaviour is similar to the one discussed previously concerning the comparison with *ab initio* finite displacement calculations [98] and could hint at an effect of the percolation threshold at 19 % minority bonds described in section 3.2.2. While the percolation threshold known from Raman measurements [93] is visible in the properties of the minority bond species, the interconnected nature of vibrational properties could make it possible that the properties of the majority bond species are affected, too. This is especially true, since the most probable cause of the deviation from the common curve in the case of In–As and Zn–Se are coupling effects between both bond species as discussed in the following section.

5.4.5 Influence of coupling effects

Hints for the importance of coupling effects can be seen in the overview of bond-stretching force constants and Einstein vibrational frequencies presented in Fig. 5.10. For (In,Ga)P the force constants vary continuously between the binary values and the Einstein vibrational frequencies differ between the two bond species. In contrast, for (In,Ga)As and Zn(Se,Te), the force constants lie apart from each other, while the vibrational frequencies change smoothly. Possibly, the vibrations of both constituting bond species are coupled for (In,Ga)As and Zn(Se,Te) aligning the respective frequencies whereas the vibrational frequencies in (In,Ga)P are not significantly affected by coupling effects. Since the difference in the Einstein frequencies of the binary compounds is larger for (In,Ga)As than for Zn(Se,Te) (approximately 1.5 THz compared to approximately 1.0 THz), the frequency shift caused by coupling is expected to be more pronounced in (In,Ga)As compared to Zn(Se,Te). This is indeed seen comparing the deviations visible in Fig. 5.7b.

To explain the differing behaviour the phonon dispersion curves of the binary materials can be used. If there exists a frequency gap between the optical and acoustic phonon

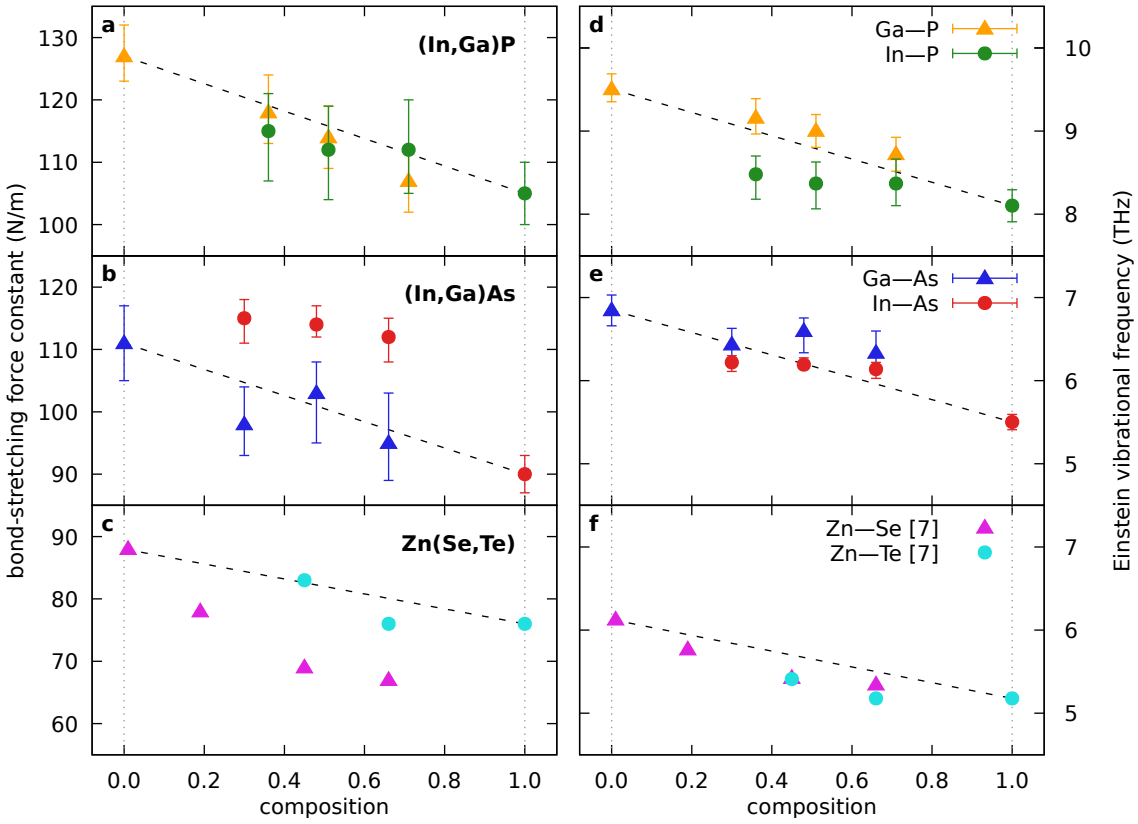

Figure 5.10: Element-specific effective bond-stretching force constants and deduced Einstein vibrational frequencies in semiconductor alloys. a-c, The bond-stretching force constants of (In,Ga)P, (In,Ga)As, and Zn(Se,Te) [7] are depicted as a function of the In or Te content, respectively. **d-f,** The Einstein vibrational frequencies were calculated from the force constants using the reduced mass of the bond. The black dashed lines depict the linear interpolations between the binary values.

Table 5.4: Properties of bonds. The bond length given is the natural bond length [4] exhibited in the binary material. The reduced mass and atom mass ratio of the bond was calculated from the atomic weights [1]. The EXAFS bond-stretching force constants for Zn–Se and Zn–Te are taken from the literature [7].

bond species	bond length [4] (Å)	reduced mass [1] (amu)	atom mass ratio [1]	force constant ($N\,m^{-1}$)	TO mode frequency [1] (THz)	Phillips ionicity [1]
Ga–P	2.360	21.45	2.25	127	10.95	0.327
In–P	2.541	24.39	3.71	105	9.13	0.421
Ga–As	2.448	36.11	1.07	111	8.00	0.310
In–As	2.623	45.34	1.53	90	6.58	0.357
Zn–Se	2.455	35.77	1.21	88	6.15	0.630
Zn–Te	2.643	43.23	1.95	76	5.43	0.609

modes of the stiffer bond species, the optical modes of the softer bond may lie within this gap and no coupling can occur between the optical modes. This is the case for (In,Ga)P, because GaP exhibits a frequency gap of more than 2 THz [85]. If the frequency gap is small or non-existent, as for GaAs [86, 88] and ZnSe [88], the phonon dispersions of the binary materials overlap, leading to the coupling of the vibrations of different bond species in (In,Ga)As and Zn(Se,Te). Since the development of a frequency gap in the binary material is related to the difference in atomic mass of its constituents, the mass ratio of the atoms forming the stiffer bond in the alloy may serve as a rough estimate whether coupling effects need to be considered. An overview of some properties of the bond species studied here, including the mass ratio, is given in Tab. 5.4.

In Fig. 5.10 it seems that in (In,Ga)As the frequency of the In–As bond is shifted up to the Ga–As frequency, while in Zn(Se,Te) the frequency of the Zn–Se bond is shifted down to match the Zn–Te frequency. The common Einstein vibrational frequency in (In,Ga)As is by trend higher than the linear interpolation of the binary values (black dashed line in Fig. 5.10), whereas it is smaller than the interpolated value in Zn(Se,Te). This impression is confirmed by the fact, that the In–As bond lies above the common curve in Fig. 5.7b, while the Zn–Se bond lies below.

At first sight, the finding that the frequency shift is visible for the longer In–As bond in (In,Ga)As and for the shorter Zn–Se bond in Zn(Se,Te) is startling. In Tab. 5.4 some properties possibly related to the vibrational properties are listed. The natural bond length, the bond strength, and the reduced mass of a bond in the binary material are directly related [1] as is shown in Fig. 3.2. The mass ratio of the atoms sharing a bond may

be important in the decision whether coupling occurs in an alloy as discussed above. However, comparing the two bond species in either Zn(Se,Te) or (In,Ga)As, the Zn–Se bond has a ratio nearer to one, while the In–As bond possesses a mass ratio farther from one. Therefore, the mass ratio does not seem to decide which bond species experiences a frequency shift.

From the properties in Tab. 5.4, only the Phillips ionicity remains as a candidate for a prediction which Einstein vibrational frequency is shifted if coupling occurs. In–As and Zn–Se are both the more ionic bond species in their respective alloy. This means, that the bond is less directional and less localised [112]. This may also lead to a less defined value of the force constant, which would explain, why the frequency of the more ionic bond shifts, while the frequency of the less ionic bond is unaffected.

5.4.6 Composition dependence of bond-stretching force constants in ternary alloys

In conclusion, the ternary zinc-blende semiconductors studied in this work show a pronounced composition dependence of the element-specific effective bond-stretching force constants and Einstein vibrational frequencies. In the case of (In,Ga)As there even is a bond-strength inversion with respect to the binary parent materials visible, i.e. the softer bond comparing the binary compounds is the stronger bond in the alloy and vice versa. Major parts of this composition dependence can be attributed to the bond length change experienced by the bonds in the ternary alloy, in direct analogy to the effects in CdTe under hydrostatic pressure. This indicates, that localisation effects and charge redistributions due to the replacement of atoms are negligible in the explanation of the basic composition dependence of bond-stretching force constants in ternary zinc-blende alloys. The most probable cause of remaining discrepancies are coupling effects between the vibrational frequencies of both bond species constituting the alloy.

6 Investigation of binary compound materials

Beside the vibrations parallel to the bond discussed in the previous chapter, the comparison of bond lengths determined by EXAFS with the mean distance between lattice sites known from XRD or optical interferometry measurements, enables the investigation of vibrations perpendicular to the bond direction in binary compound semiconductors as described in section 2.3.3. A comprehensive set of temperature-dependent EXAFS data from III-V compound semiconductors can therefore provide insight into the connection between fundamental material properties, like the mass ratio and the ionicity of the bond, and the vibrational anisotropy thought to be related to the NTE observed for many materials with zinc-blende structure [24]. Such a systematic comparison is not possible using only literature data, since the analysis procedure, for example whether the harmonic or the anharmonic correlated Einstein model is used (see sections 5.1.2 and 6.2.2), has a significant impact on the results. The consistent analysis of the current dataset is therefore the foundation of a substantiated discussion of the uncertainties and limitations in the determination of force constants from temperature-dependent EXAFS measurements.

6.1 Analysis of binary compound data

6.1.1 Sample overview

Samples were measured at the Hamburger Synchrotronstrahlungslabor (HASYLAB), at the Swiss Light Source (SLS), at the Photon Factory (PF), and at the Australian Synchrotron (AS) as described in sections 4.3 to 4.5. An overview is given in Tab. 6.1. The datasets measured at PF and AS were already aligned, but were subjected to the normal calibration and alignment procedure as detailed in section 4.6, to rule out differences between the datasets arising due to different alignment routines. Where reference data was available, this was used for alignment, otherwise the sample spectra were used.

Table 6.1: Sample overview. The measurement mode was either transmission (T) or fluorescence (F) mode.

sample name	facility	measurement year	measurement mode	comments
$InP_{HASYLAB}$	HASYLAB	2012	T	
InP_{PF}	PF	2007	T	same data as in [31]
$InAs_{SLS}$	SLS	2015	F	
$InSb_{SLS}$	SLS	2015	F	
$GaP_{HASYLAB}$	HASYLAB	2012	T	
GaP_{AS1}	AS	2010	T	
GaP_{AS2}	AS	2011	T	
$GaAs_{SLS}$	SLS	2014	F	
$GaAs_{AS1}$	AS	2009	T	
$GaAs_{AS2}$	AS	2011	T	
$GaSb_{SLS}$	SLS	2014	F	
$GaSb_{AS1}$	AS	2010	T	
$GaSb_{AS2}$	AS	2011	T	

6.1.2 Parametrisation of the scattering paths

For the model based on the zinc-blende structure, either the first twelve or only the first scattering path(s) were/was used. The lattice constants were taken from the literature [4]. The amplitude reduction factor S_0^2 and the energy offset E_0 were varied freely per sample. The Einstein model for the variance, the asymmetry parameter and kurtosis parameter contained all anharmonic terms given in the literature [47] as implemented in the analysis scripts (see appendix C.1). They are determined by the parameters of the effective pair potential, namely the bond-stretching force constant $k_{\parallel}=k_0$, the cubic force constant k_3, and the quartic force constant k_4 (see section 2.3.3). All cumulant formulas used neglect cross-correlation between parallel and perpendicular vibrations [47].

When using only the first scattering path, the analysis of the In-edge measurements showed a clear oscillatory dependence on the higher end of the Fourier-transform window (kmax), indicating significant leaking of higher shell contributions into the first shell signal [111]. Therefore, all subsequent analysis of the In-edge spectra used the twelve-path model (see sec. 4.6). The higher-shell leakage effect was less pronounced for the Ga-edge data. Because of this, Ga-edge data analysis was done using both the single-path and the twelve-path model.

From the temperature-dependent bond lengths R_{EXAFS} determined in the fits, the variance of the distribution of displacements perpendicular to the bond direction $\langle \Delta u_{\perp}^2 \rangle$ can

be extracted using eq. 2.14. The necessary mean distances between lattice sites R_C are known from XRD measurements (GaP, InP, GaAs, and InAs) [121] or linear thermal expansion measurements of single crystals by optical interferometry (GaSb and InSb) [122, 123]. The temperature dependence of $\langle \Delta u_\perp^2 \rangle$ was fitted by a harmonic correlated Einstein model [4, 34] via a bond-bending force constant and a static contribution to the variance using the *curve_fit* function of `python.numpy`. In this approach, neither the uncertainties of the bond lengths R_{EXAFS} nor their correlations with each other and with additional parameters are propagated to the bond-bending force constants determined. However, the alternative of restricting the bond lengths in the first fit (LARCH fit of the spectrum) to the harmonic correlated Einstein model needs an unpractical amount of computation time.

An additional possibility not reliant on literature thermal expansion data is the use of the anharmonic correlated Einstein model to calculate the temperature dependence of the mean distance of lattice sites from the effective pair potential [47]. The EXAFS first cumulant (bond length) can then be parameterised using the thermal expansion described by the potential parameters of the parallel vibrations (k_0,k_3, and k_4) and the additional contributions by perpendicular vibrations. Unfortunately, fits realising this approach are computationally expensive and partially unstable thus severely limiting the applicability of this approach. A limited number of tests was performed for both of these *all-in-one fit* approaches. The effective bond-bending force constant could be expected to depend on the parametrisation of the bond length change. The values obtained from the *all-in-one fits* show reasonable agreement with the effective bond-bending force constants of the *two-subsequent fits* approach, for the samples where the fit results are within the range physically possible. While the LARCH fitting routine reports significant correlations between the bond-bending force constant and the bond-stretching force constant, the *all-in-one fits* yield effective bond-stretching force constants in good agreement with the *two-fits* approach for almost all samples. The results for the effective bond-stretching force constants are therefore independent of the parametrisation of the bond lengths.

6.1.3 Challenges during data analysis

In contrast to the ternary (In,Ga)As data (see sec. 5.2.1), the Hf L_2 edge and its whiteline where barely visible for the binary Ga-containing compounds measured at SLS. Therefore, a correction of the distortion caused by the Hf L_2 edge was not necessary.

Some samples yield unreasonable amplitude reduction factors. This applies to GaP_{AS2}, $GaAs_{AS2}$, and $GaSb_{SLS}$, with amplitude reduction factors of 2.15 ± 0.05, 1.50 ± 0.03, and 0.43 ± 0.03, respectively. Both fits of individual spectra and fits of the temperature series

yield these values. They are further confirmed by individual fits using the *quick first shell fit* tool of ARTEMIS [124]. Amplitude reduction factors can also be determined by setting fixed values in a wide range and performing fits with different kweight parameters [125]. Since parts of the fit results are physically meaningful parameters and should not depend on the kweight used, the fit results for these parameters should not differ comparing different kweight values for the true value of the amplitude reduction factor [125]. Using the first-nearest neighbour (1NN) bond-stretching force constant and the static contribution to the variance of the 1NN distance distribution as decisive result values, the amplitude reduction factors previously determined were affirmed. For $GaSb_{SLS}$ the Booth algorithm implemented in ATHENA [124] was used to rule out the distortion of the spectra by over-absorption effects (see also appendix C.6).

It is well known, that the amplitude reduction factor depends on the absorbing atom as well as the crystal structure of the material [126]. Since many experimental effects, like higher harmonics of the monochromator (see section 2.2.1) or detector nonlinearities, also influence the amplitude reduction factor, it may also differ for different beamlines [36]. For the current dataset it can be seen, that measurements at the In-K edge yield higher amplitude reduction factors than measurements at the Ga-K edge. This is consistent with reports of the amplitude reduction factor as a function of the atomic number of the absorbing atom [126], where the values for atomic numbers around 49 (In) are approximately 20 % higher than the values for atomic numbers around 31 (Ga). Comparing the different beamlines, measurements at the AS from 2011 yield the highest values followed by measurements at the AS before 2011, measurements at HASYLAB and the PF. Measurements at the SLS yield the lowest amplitude reduction factors. Despite the fact, that all materials studied here exhibit the same crystal structure, the phosphides are characterised by higher amplitude reduction factors than the arsenides, which in turn yield higher values than the antimonides. Given this systematic, the problematic samples are those combining materials that give high amplitude reduction factors with a beamline yielding high values (GaP and GaAs at AS in 2011), or a material giving a low amplitude reduction factor with a beamline yielding low values (GaSb at SLS). However, the reason for the stark differences is unclear.

Additionally to the problematic amplitude reduction factors, for all three of the problematic samples, the parameter values determined in the fits of the temperature series are marked by large individual-fit uncertainties, large deviations between individual fits, and partially unreasonable values. The data of GaP_{AS2},$GaAs_{AS2}$, and $GaSb_{SLS}$ was therefore discarded.

6.2 Bond-stretching force constants and pair potential parameters

The accumulated individual fit results for the effective bond-stretching force constants in all remaining samples are shown in Figs. 6.1 and 6.2, for the Ga-containing and In-containing samples, respectively. Compared to the study of the composition dependence (see Fig. 5.2 and Fig. 5.4), the variations are larger. This can be attributed to the more complex model, including higher anharmonic contributions and, compared to the (In,Ga)As analysis, more scattering paths.

6.2.1 Correlations between potential parameters

The analysis of the fit results of the complete set of tests reveal a significant mathematical correlation between the parameters of the effective pair potential for a given material. Since the physical property is the effective pair potential, this could mean either that the same form of the potential can be reached through different parameter combinations, or that the data quality is not sufficient to distinguish between the different potential forms. An example of the correlation between k_0 and k_3, and k_0 and k_4 can be seen for one GaP and one InP sample in Figs. 6.3 and 6.4, respectively. Analog diagrams for the other materials can be found in appendix C.5.

Most samples show an increase of the bond-stretching force constant with increasing cubic force constant. The exceptions are both samples of GaSb, which exhibit very different patterns with large variations in the bond-stretching force constant. Together with the chaotic behaviour of the bond-stretching force constant as a function of the fit quality parameter visible for $GaSb_{AS1}$ in Fig. 6.1, this may indicate that the results for GaSb are rather unreliable. For the samples $GaP_{HASYLAB}$, $GaSb_{AS1}$, and $InAs_{SLS}$ a cluster of values appears with negative k_3 and large k_4 (see Fig. 6.3). A negative cubic force constant k_3 would lead to a negative thermal expansion coefficient in the high temperature limit [47]. While NTE is known to occur for zinc-blende materials, it is restricted to a temperature range usually below 100 K [1]. Therefore, negative k_3 are not physically reasonable. This assessment is supported by the fact, that significantly negative k_3 appear only sporadically in the tests for either very low or very high values of kmax ($13\,\text{Å}^{-1}$ and $16\,\text{Å}^{-1}$, respectively). This implicates, that for $GaP_{HASYLAB}$ bond-stretching force constants below $120\,\text{N}\,\text{m}^{-1}$, and for $GaSb_{AS1}$ most values below $110\,\text{N}\,\text{m}^{-1}$, should be ignored. The correlation between the quartic force constant and the bond-stretching force constant is marked

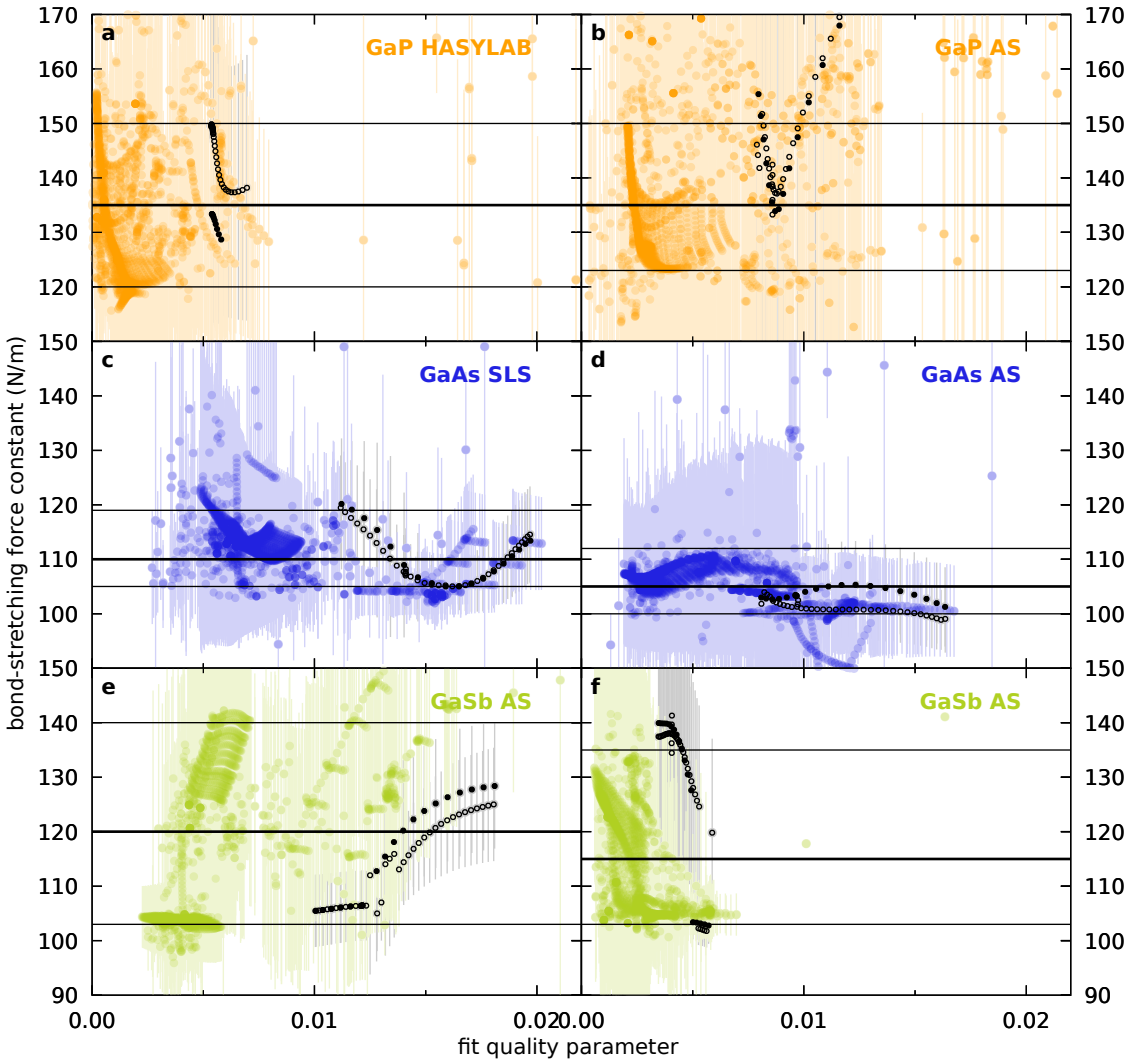

Figure 6.1: Uncertainties of the bond-stretching force constants in GaP, GaAs and GaSb. The effective bond-stretching force constants resulting from more than 1500 fits per sample are shown as a function of the fit quality parameter R. Smaller R factors mean better fits. The error bars plotted are the uncertainties given for an individual fit by the LARCH fitting routine. Coloured symbols depict results from the *two-fits* approach, employed for most of the analysis. The results from *all-in-one* fits using literature thermal expansion data (open black symbols) or calculated temperature-dependent bond lengths (solid black symbols) are shown for comparison. Thick and thin black lines refer to the best, minimum and maximum force constant values given in Tab. 6.2.

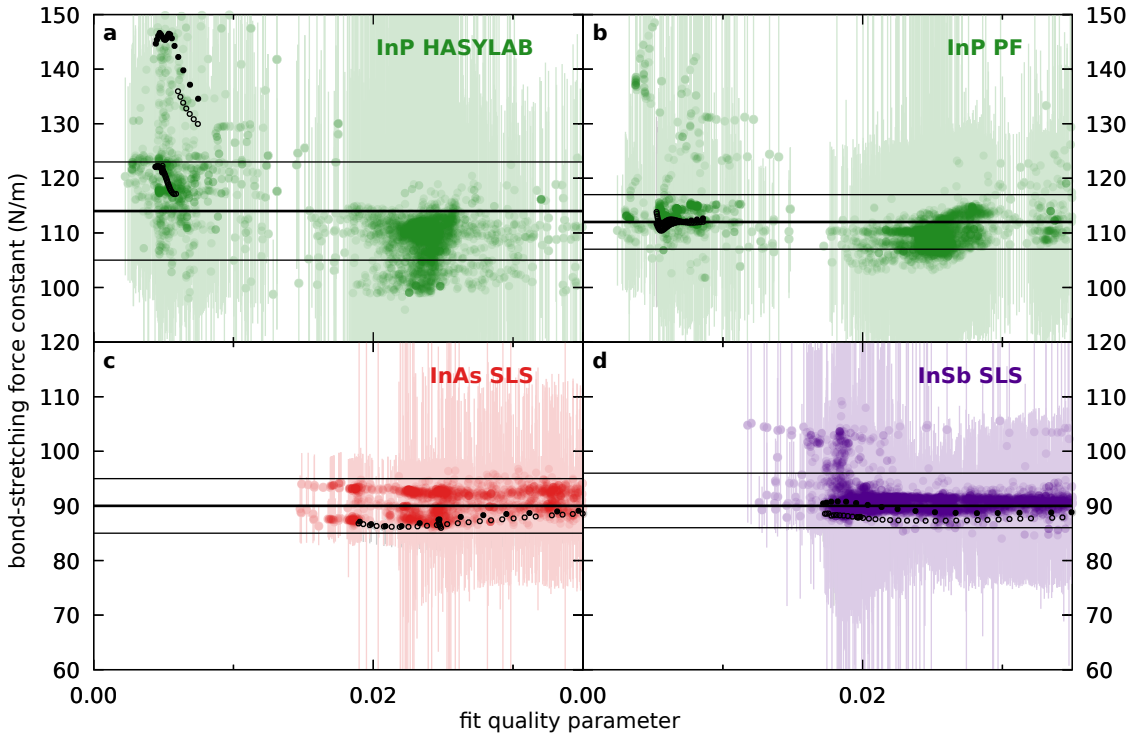

Figure 6.2: Uncertainties of the bond-stretching force constants in InP, InAs and InSb. The effective bond-stretching force constants resulting from more than 2500 fits per sample are shown as a function of the fit quality parameter R. The description is the same as in Fig. 6.1.

by the existence of two or three branches where most of the fit results aggregate. This characteristic is visible for most samples. The results for the effective bond-stretching force constants considering both the trends with fit quality and the correlations with the other potential parameters are summarised in Tab. 6.2. For their better evaluation, the values are also added to Fig. 6.1 and Fig. 6.2 as black lines.

6.2.2 Comparison to elastic constants and Raman frequencies

The samples $GaP_{HASYLAB}$, $InP_{HASYLAB}$, $GaAs_{SLS}$, and $InAs_{SLS}$ were already analysed as parent materials of the ternary alloys (In,Ga)P and (In,Ga)As in chapter 5. However, the analysis there included less terms of anharmonic contributions and for (In,Ga)As less scattering paths due to the restrictions imposed by the analysis of the ternary alloys. The bond-stretching force constants determined with higher anharmonic contributions are very similar to the previous analysis for GaAs and InAs, but increase for GaP and InP, probably due to the anharmonic contributions as discussed in section 5.1.2. The difference

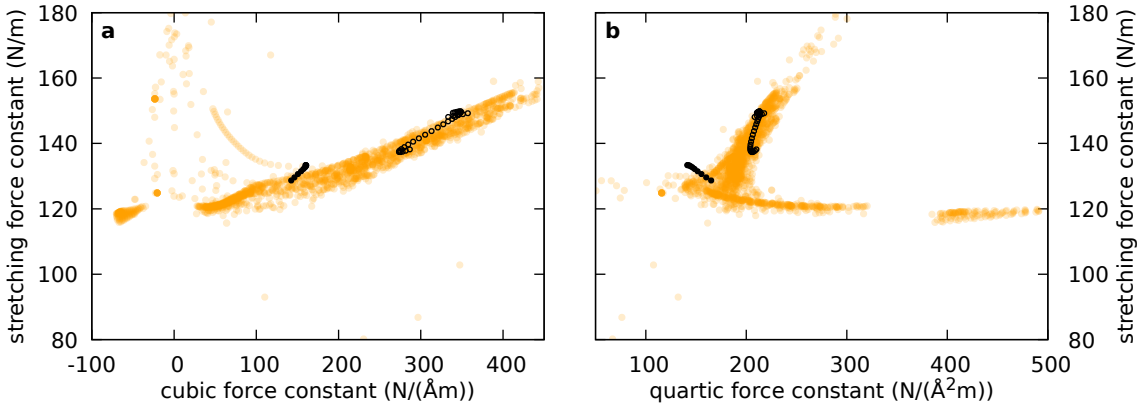

Figure 6.3: Correlations between parameters of the 1NN interatomic potential for GaP measured at HASYLAB. The bond-stretching force constant is shown as a function of the cubic force constant (panel a) and as a function of the quartic force constant (panel b). Coloured symbols depict results from the *two-fits* approach, employed for most of the analysis. The results from *all-in-one* fits using literature thermal expansion data (open black symbols) or calculated temperature-dependent bond lengths (solid black symbols) are shown for comparison. The uncertainties of the parameter values were omitted for the sake of clarity.

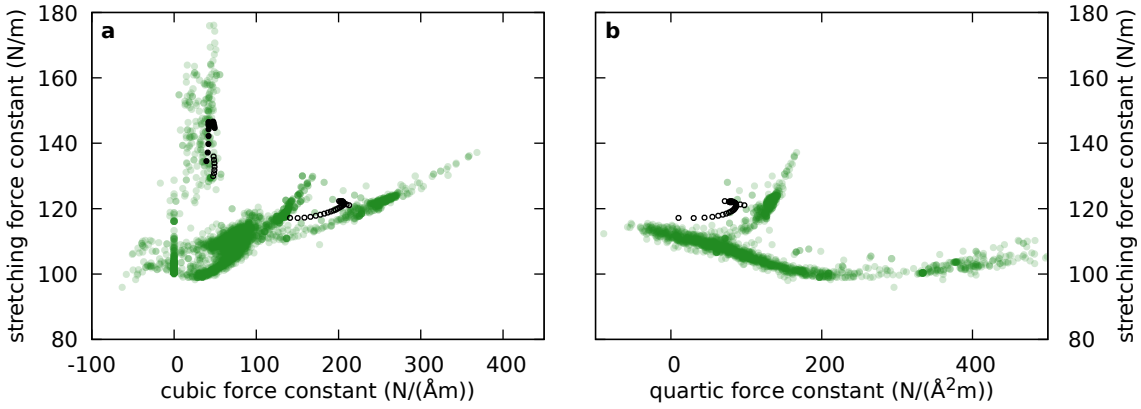

Figure 6.4: Correlations between parameters of the 1NN interatomic potential for InP measured at HASYLAB. The bond-stretching force constant is shown as a function of the cubic force constant (panel a) and as a function of the quartic force constant (panel b). Coloured symbols depict results from the *two-fits* approach, employed for most of the analysis. The results from *all-in-one* fits using literature thermal expansion data (open black symbols) or calculated temperature-dependent bond lengths (solid black symbols) are shown for comparison. The uncertainties of the parameter values were omitted for the sake of clarity.

Table 6.2: Force constants in binary III-V materials. The final values determined for the bond-stretching force constant, the bond-bending force constant, and the 2NN stretching force constant are shown together with their minimum and maximum reasonable values.

	1NN $k_{\parallel}$ ($N\,m^{-1}$)			1NN $k_{\perp}$ ($N\,m^{-1}$)			2NN $k_{\parallel}$ ($N\,m^{-1}$)		
	best	min	max	best	min	max	best	min	max
$InP_{HASYLAB}$	114	105	123	13	10	21	31	28	34
InP_{PF}	112	107	117	22	18	30	31	28	34
$InAs_{SLS}$	90	85	95	30	20	45	25	23	30
$InSb_{SLS}$	90	86	96	14	7	22	25	21	32
$GaP_{HASYLAB}$	135	120	150	30	20	40	42	40	44
GaP_{AS1}	135	123	150	30	20	40	44	41	47
$GaAs_{SLS}$	110	105	119	20	15	30	33	30	36
$GaAs_{AS1}$	105	100	112	22	17	32	31	28	34
$GaSb_{AS1}$	120	103	140	20	12	30	25	22	28
$GaSb_{AS2}$	115	103	135	25	15	40	27	24	30

can be seen in Fig. 6.5a, where anharmonic and harmonic effective bond-stretching force constants are depicted as solid and open symbols, respectively. That anharmonic contributions are important to a varying degree for different materials, could be related to different cubic and quartic force constants. However, the cubic and quartic force constants of the phosphides show no significant difference compared to the arsenides as is shown later in section 6.2.3. Also, the same cubic force constant can have different effect depending on the value of the bond-stretching force constant. The cause is, that a larger bond stretching force constant (i.e. a larger Einstein vibrational frequency) shifts the onset of the rise in variance to larger temperatures (see Fig. 2.6a). Since effects of anharmonicity can mostly be seen above this critical temperature (see Fig. 2.6b), materials featuring smaller bond-stretching force constants should, assuming the same range of measurement temperatures, show larger differences between the harmonic and anharmonic correlated Einstein model. This is, however, not the case for the comparison between phosphides and arsenides, where the phosphides show the larger influence of anharmonic contributions despite their larger bond-stretching force constants. Therefore, the reason for the different influence of anharmonic contributions remains unclear.

Due to the shift in values of the bond-stretching force constants of GaP and InP when using more anharmonic contributions, the bond-length dependence, which was well described by a r^{-3} trend in Fig. 5.7a is now less defined, as can be seen in Fig. 6.5a. This

effect is intensified by the values of GaSb and InSb. Thus, the bond-stretching force constants show a bond-length dependence different from the trend observed for the force parameters determined from elastic constants. In Fig. 6.5b the relation between the EXAFS bond-stretching force constants and the elastic force constants 3α [6] is illustrated. While the values of GaP, InP, GaAs, and InAs show a nearly linear relationship, the values of GaSb and InSb deviate significantly from this trend, demonstrating the profound difference of the two measures of bond strength.

To explore the similarities to Raman TO mode frequencies, the Einstein vibrational frequencies calculated from the bond-stretching force constants via the reduced mass of the bond are plotted as a function of the inverse reduced mass in Fig. 6.5c. As discussed in section 5.4.3, Einstein vibrational frequencies and TO phonon mode frequencies are not directly comparable. Nevertheless, it is informative to compare the dependencies on other material parameters. In agreement with the behaviour of TO phonon modes (see Fig. 3.2b), the Einstein frequencies increase linearly with the inverse of the reduced mass of the bond. Yet the values of the In-containing compounds all lie slightly below the best fitting linear dependence, while the values of the Ga-containing compounds lie slightly above it. Similarly, one could draw parallel lines through the P-containing, As-containing, and Sb-containing compounds. Both effects could be explained by a dependence on the ionicity of the bond (see Tab. 6.3). To confirm this, the difference between the Einstein vibrational frequencies of the samples and the linear function assumed for the dependence on the reduced mass were plotted as a function of ionicity. Only a slight adjustment of the linear dependence in Fig. 6.5c from the solid black line to the dashed black line is needed to gain the linear dependence on ionicity depicted in Fig. 6.5d. Therefore, the Einstein vibrational frequencies in III-V compounds can be calculated to good accuracy by a bilinear function of the inverse reduced mass μ (in amu^{-1}) and the Phillips ionicity f_i of the bond as

$$\nu_{\parallel}(\mu, f_i) = 4.1 + 170\mu^{-1} - 6.6 f_i. \tag{6.1}$$

Such a relation including the ionicity of the bond is not visible for the TO phonon frequencies, which are reasonably well described using the dependence on the reduced mass of the bond [1]. The remaining discrepancies show no dependence on the ionicity. However, the relationship between bond-stretching and bond-bending parameters determined from elastic constants, α and β, respectively, is reported to involve the factor $(1 - \mathrm{f_i})$ [5, 60]. It is therefore not surprising, that the Einstein vibrational frequency is related to the ionicity of the bond.

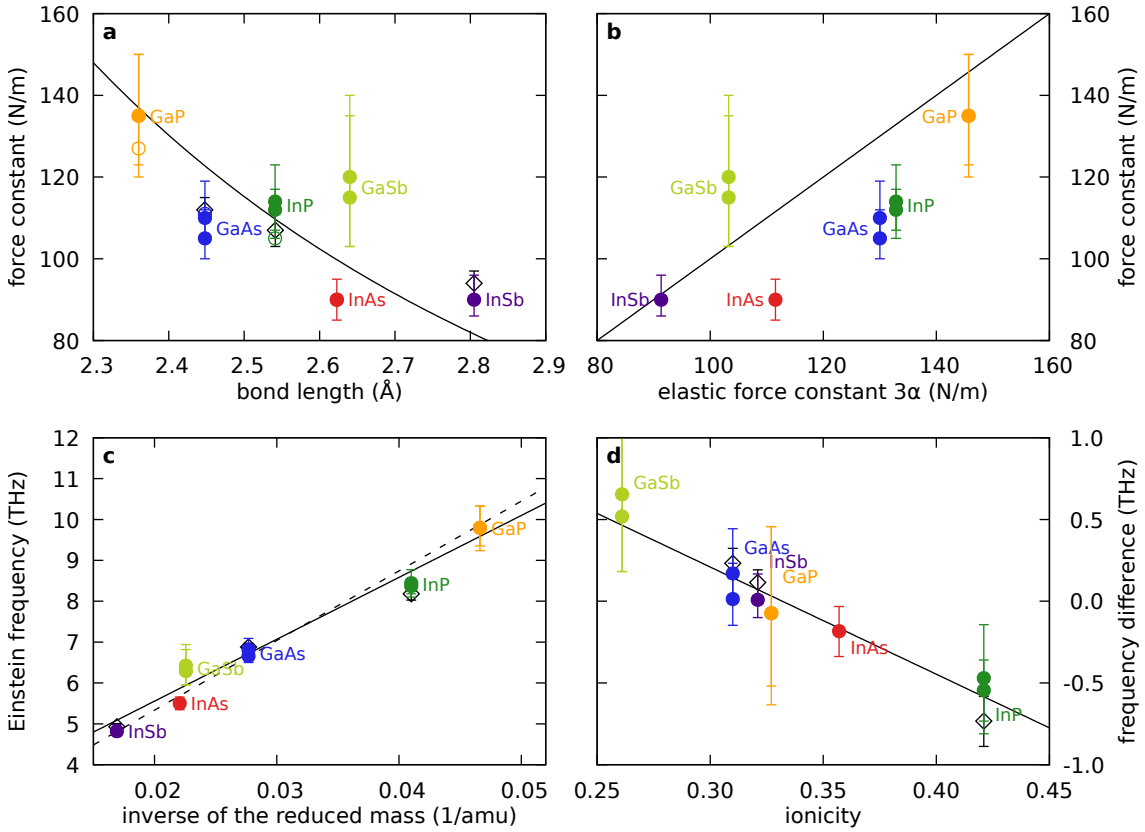

Figure 6.5: Bond-stretching force constants as a function of bond length and Einstein vibrational frequencies as a function of the inverse reduced mass and the ionicity of the bond. Coloured symbols depict the values obtained in this work, while black symbols show the literature data [31–33]. **a,** The EXAFS bond-stretching force constants roughly decrease with increasing bond length. The r^{-3} dependence best fitting the coloured symbols is shown as solid black line. The harmonic force constants of GaP, InP, GaAs, and InAs stemming from the analysis of the ternary alloys in chapter 5 are added as open symbols without error bars. **b,** The EXAFS bond-stretching force constants are depicted as a function of the elastic force constants 3α [6]. The solid black line indicates the line of equality between both parameters. **c,** The Einstein vibrational frequencies calculated from the bond-stretching force constants rise linearly with the inverse of the reduced mass of the bond. The best fitting linear dependence is added as solid black line. The dashed black line depicts the linear function optimised to yield a linear dependence on ionicity in panel c. **d,** The difference of the Einstein frequencies to the dashed line in panel c is plotted as a function of ionicity of the bond.

Table 6.3: Properties of binary III-V materials. The reduced mass and atom mass ratio of the bond was calculated from the atomic weights [1].

material	lattice constant [4] (Å)	bond length [4] (Å)	Phillips ionicity [1]	reduced mass [1] (amu)	atom mass ratio [1]
GaP	5.451	2.360	0.327	21.45	2.25
GaAs	5.653	2.448	0.310	36.11	1.07
GaSb	6.096	2.640	0.261	44.34	1.75
InP	5.869	2.541	0.421	24.39	3.71
InAs	6.058	2.623	0.357	45.34	1.53
InSb	6.479	2.805	0.321	59.09	1.06

6.2.3 Cubic and quartic force constants

To study the cubic force constant k_3 and the quartic force constant k_4 independent of the trends observed for the bond-stretching force constant $k_{\|}$, their values were plotted with respect to $k_{\|}$ in Fig. 6.6. The values were determined from plots of the whole set of fits as a function of the fit quality parameter.

Focusing on the values obtained in this work (coloured symbols), the only significant trend visible is the decrease of $k_3/k_{\|}$ with increasing bond length shown in panel a. In particular, there is no clear trend with ionicity for both $k_3/k_{\|}$ and $k_4/k_{\|}$. This may indicate, that the decrease of the cubic force constant with increasing ionicity reported before [33, 50] can be explained by an overall scaling factor to the potential equation 2.18 equally effecting $k_{\|}$=k_0, k_3, and k_4. However, taking into account the literature value for $k_3/k_{\|}$ in GaAs a slight increase with increasing Phillips ionicity could be seen, if the current values of both GaP and GaAs are faulty. Hence, in the current state it is not possible to decide, whether the bond length or the ionicity is the main parameter influencing the anisotropy parameter $k_3/k_{\|}$. Another option to study the anharmonicity of the effective pair potential poses the skewness parameter $k_3/k_{\|}^{3/2}$ [50] . When plotting $k_3/k_{\|}^{3/2}$ instead of $k_3/k_{\|}$ the trends from Fig. 6.6 remain nearly unaltered.

6.2.4 Effective pair potential

While the bond-stretching force constant is the most intuitively comprehensible of the potential parameters, the cubic and quartic force constants have significant impact on the shape of the potential. The effective pair potential calculated from eq. 2.18 is plotted in Fig. 6.7.

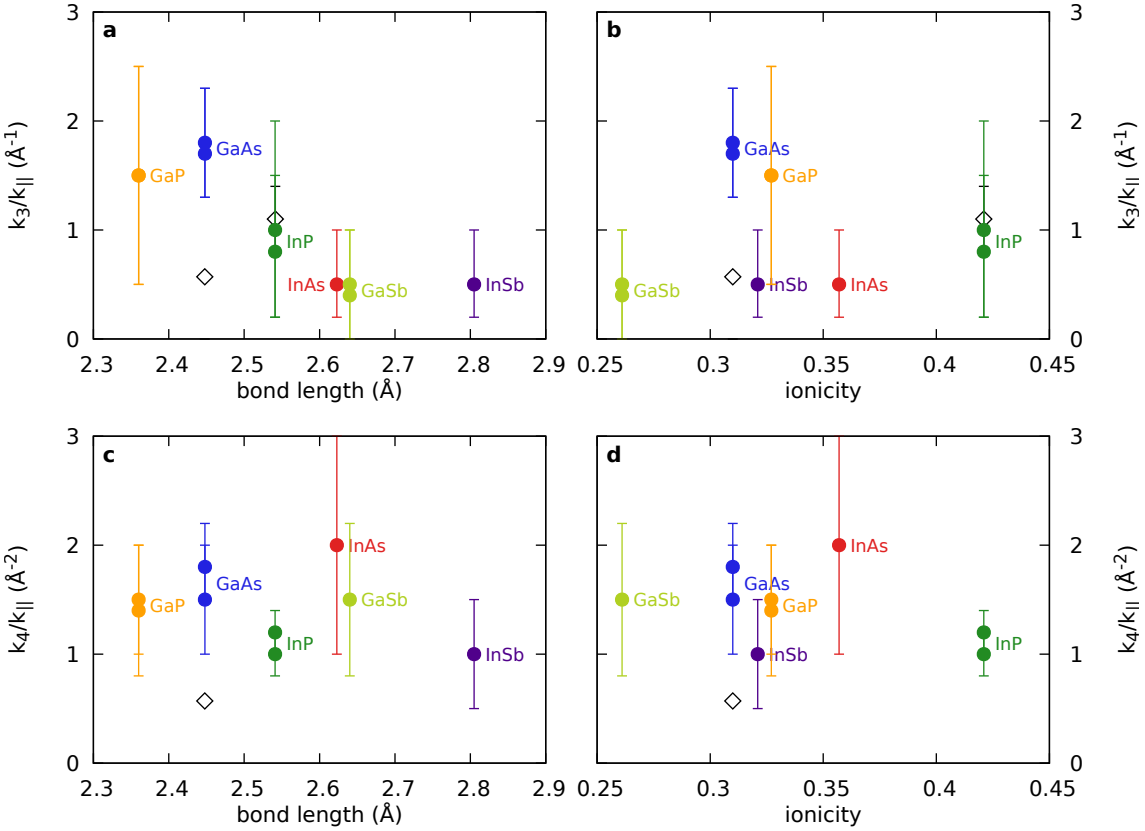

Figure 6.6: Anharmonicity parameters. Coloured symbols depict the values obtained in this work, while black symbols show the literature data for InP [31] and GaAs [33]. **a-b,** The ratio between cubic and bond-stretching force constant is plotted as a function of bond length and Phillips ionicity of the bond. **c-d,** The ratio between quartic and bond-stretching force constant is plotted as a function of bond length and Phillips ionicity of the bond.

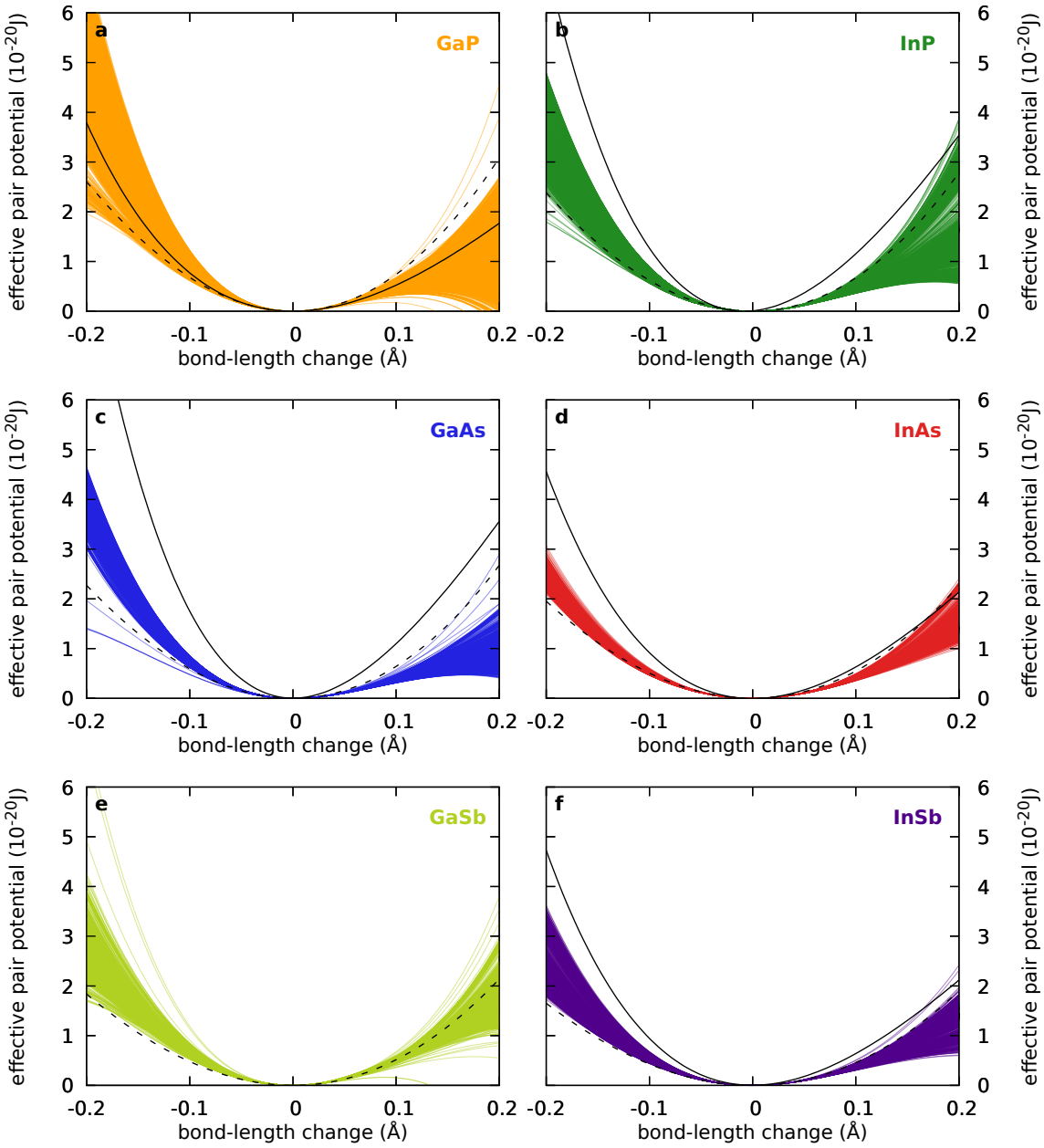

Figure 6.7: Effective pair potential. For each fit a potential curve according to eq. 2.18 was drawn. The complete set of tests was restricted to the fits that yield a bond-stretching force constant within the uncertainty interval given in Tab. 6.2 for the respective sample and a non-negative cubic force constant. If more than one sample was measured for a given material, the results of all samples were plotted together in one panel. For comparison, the bond-stretching part of the Keating potential using the force parameters determined from elastic constants [5] and the 1NN bond-stretching contribution to the Vashishta potential [127] used in molecular dynamics calculations [51, 65, 128, 129] are plotted as dashed black lines and solid black lines, respectively.

For all six materials studied, the potential is clearly asymmetric with higher values at smaller bond lengths. This characteristic is not reproduced by the bond-stretching part of the Keating potential calculated using the force parameters determined from elastic constants [5] which is plotted as dashed black lines in Fig. 6.7. In contrast, the bond-stretching part of the Vashishta potential [127] frequently used in molecular dynamics calculations [51, 65, 128, 129] does show the correct asymmetry. The potential minimum does not match the bond length expected from the lattice constant exactly, probably, because the potential was restricted to the interaction of one single bond. Therefore, only differences with respect to the minimum are plotted in Fig. 6.7 as solid black line.

For GaP the agreement between the effective pair potential determined with EXAFS and the Vashishta potential is very good. For GaAs, InP, InAs, and InSb, the Vashishta potential yields values approximately two times larger than the EXAFS potential, while the overall shape is very similar.

6.3 Bond-bending force constants and anisotropy parameters

The bond-bending force constants determined from the set of fits shown in Fig. 6.1 and Fig. 6.2 are summarised in Tab. 6.2. The overview of the individual results of the fits is shown in appendix C.5. The bond-bending force constants were plotted as a function of the fit quality parameter from the first (LARCH spectrum) fit, while the fit quality of the second (bond-length) fit was not considered. To test the influence of the literature data of R_C, fits were also carried out under the assumption of half or double the thermal expansion compared to the literature [121–123]. In both cases, the overall distribution of bond-bending force constants as a function of fit quality parameter stays the same, with the force constant values shifted down by up to 10 % assuming half the thermal expansion and shifted up by up to 25 % assuming double the thermal expansion. The samples which show larger variations for a given thermal expansion, also show larger variations when changing the assumption.

6.3.1 Trends in bond-bending force constants

In Fig. 6.8a the bond-bending force constants are plotted as a function of the bond length. The values tend to decrease with increasing bond length and show reasonable agreement with EXAFS bond-bending force constants found in the literature for GaAs [33] and InP

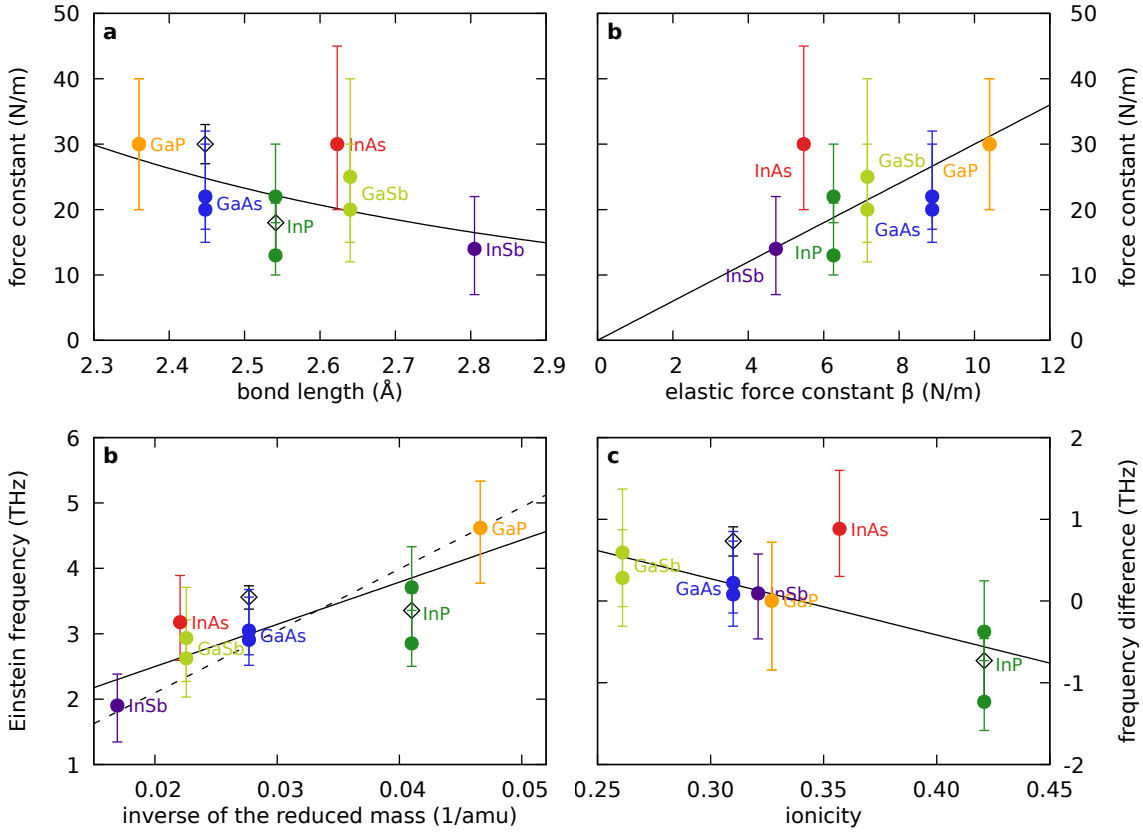

Figure 6.8: Bond-bending force constants as a function of bond length and Einstein vibrational frequencies as a function of the inverse reduced mass and the ionicity of the bond. Coloured symbols depict the values obtained in this work, while black symbols show the literature data [31, 33]. **a,** The EXAFS bond-bending force constants show no clear bond-length dependence. The r^{-3} dependence best fitting the coloured symbols is shown as solid black line. **b,** The EXAFS bond-bending force constants are compared to the elastic force constant β. The solid black line indicates the linear function 3β. **c,** The Einstein frequencies of vibrations perpendicular to the bond roughly increase with increasing inverse of the reduced mass of the bond. The best fitting linear dependence is added as solid black line. The dashed black line depicts the linear function optimised to yield a linear dependence on ionicity in panel c. **d,** The difference of the Einstein frequencies to the dashed line in panel c is plotted as a function of ionicity of the bond.

[31]. For comparison the best fitting r^{-3} dependence is added as solid line, since such a dependence was observed for the bond-bending force parameters stemming from measurements of the elastic constants [60]. The EXAFS bond-bending force constants are in rough agreement with such a trend, but, due to the large uncertainties, many functions could be fitted to these values. The EXAFS bond-bending force constants are compared to the elastic bond-bending parameters β determined from elastic constants [6] in Fig. 6.8b. While the force constant k_θ is defined by $2/3\,\beta$ (see section 3.2.1), the EXAFS bond bending force constants $k_\perp$ follow astonishingly well the relation 3β indicated by the black solid line. The only exception is the value of InAs which is larger than expected from the overall trend.

By analogy to the Einstein vibrational frequency of the parallel vibrations, the perpendicular Einstein vibrational frequencies are plotted as a function of the inverse reduced mass of the bond in Fig. 6.8c. As before, the frequencies increase roughly linear with increasing inverse reduced mass. Similar to the parallel Einstein vibrational frequency, one can alter the best fitting linear function (solid line) to explain the deviations by a linear dependence on ionicity. The result is shown in Fig. 6.8d. Thus, the Einstein vibrational frequency of vibrations perpendicular to the bond can be described by a bilinear function of inverse reduced mass μ^{-1} (in amu^{-1}) and Phillips ionicity f_i as

$$\nu_\perp(\mu, f_i) = 2.5 + 95\mu^{-1} - 6.9 f_i. \tag{6.2}$$

Again, the visible exception not fitting on this line is the value of InAs. Since the individual fit values obtained for InAs show large variations as visible in appendix Fig. C.17c, this deviation could be attributed to the fits being rather unstable with respect to the bond-bending force constant.

6.3.2 Trends in anisotropy parameters

The anisotropy parameter is defined as the ratio between the bond-stretching and the bond-bending force constant, $\xi = k_\parallel/k_\perp$ [50]. Alternatively, one can study the parameter $\xi^{1/2}$, which describes the anisotropy with respect to the Einstein vibrational frequencies. The results for both parameters are plotted in Fig. 6.9 as a function of different bond properties. The values were calculated from the force constants given in Tab. 6.2, while the uncertainties were estimated from plots of the single fit results against the fit quality parameter, which can be found in appendix C.5 as Fig. C.18 and Fig. C.19. Keeping in mind, that the value for InAs might be distorted by a false bond-bending force constant,

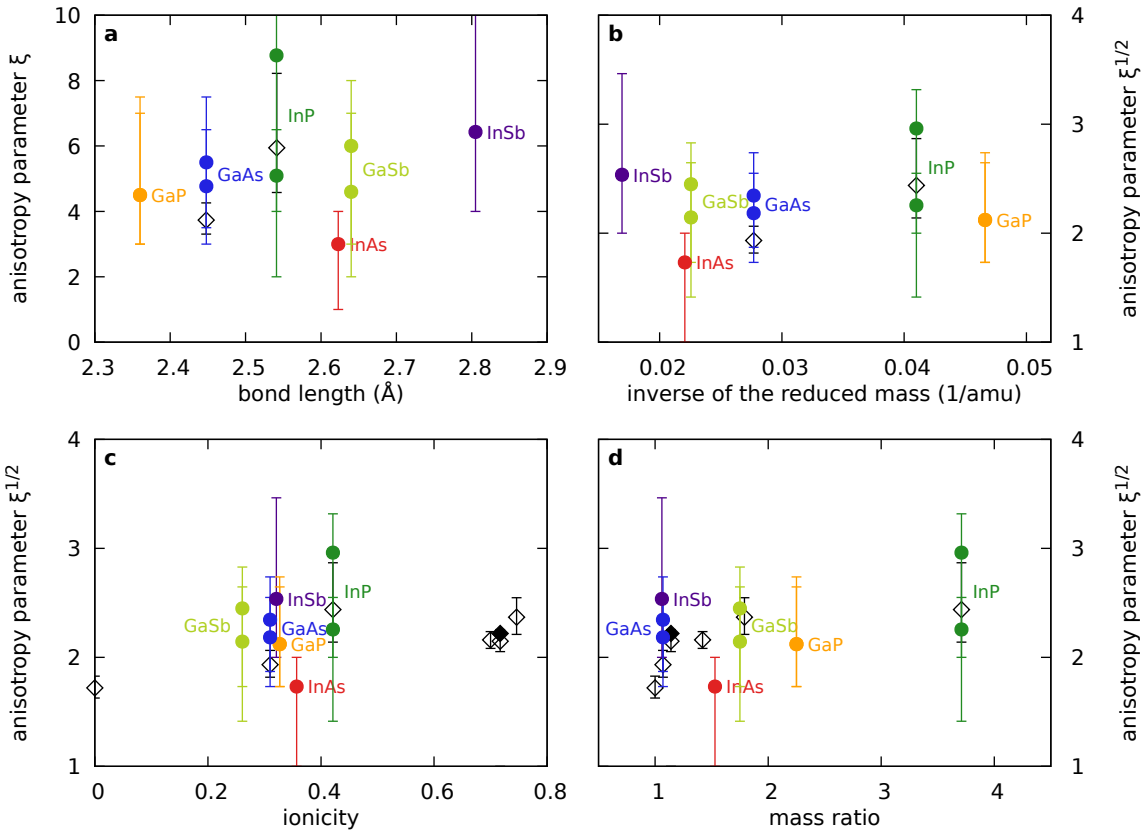

Figure 6.9: Anisotropy parameters with respect to the force constants (ξ) and with respect to the Einstein vibrational frequencies ($\xi^{1/2}$). a, The anisotropy parameter ξ is plotted as a function of bond length and compared to literature values of GaAs [33] and InP [31]. **b-d,** The anisotropy parameter $\xi^{1/2}$ is plotted against the inverse of the reduced mass, ionicity, and mass ratio of the bond. Open black symbols depict the literature values for GaAs [33], InP [31], Ge [101, 103], CdTe [24], CdSe [50, 100], and CuCl [102] using the harmonic correlated Einstein model. The anisotropy parameter of CdTe stemming from an analysis using anharmonic contributions [34] is given as solid black symbol.

the anisotropy slightly increases with increasing bond length and is constant as a function of the reduced mass. To compare the anisotropy between IV, III-V, II-VI, and I-VII materials plotting against the ionicity or the mass ratio of the bond can be used [50]. The literature values show an increase with ionicity and an increase with increasing mass ratio. While the values determined here are consistent with such a trend, the uncertainties are too large to reach a definite conclusion. In particular, this also precludes a meaningful correlation of the anisotropy parameter with the strength of the NTE as originally intended.

The large uncertainties compared to the literature data are caused by several factors. First, the inclusion of anharmonic contributions in the correlated Einstein model of the vibrations parallel to the bond enhances the mathematical correlation between the parameters of the effective pair potential and decreases the stability of the fit as can be seen from the analysis of the ternary alloys, where the higher anharmonic contributions even preclude the fit from converging (see sections 5.1.2 and 5.2.2). Since in most of the EXAFS studies found in the literature the harmonic correlated Einstein model is used to describe the temperature dependence of the variance of the distance distribution, the force constants and anisotropy parameters determined there are expected to exhibit somewhat smaller uncertainties. The only exception is the literature value of CdTe [34], which stems from an analysis including anharmonic contributions. However, no uncertainty for the bond-stretching force constant is given there. While the harmonic approximation significantly reduces the uncertainties, it also decreases the bond-stretching force constants in some materials (CdTe [34], GaP, and InP), while other materials are unaffected (GaAs and InAs). Therefore, a trend visible in the harmonic effective bond-stretching force constants or derived properties like the anisotropy parameter, could stem either from a trend in the force constants or from a trend in the shift caused by the harmonic approximation. Hence, one should avoid the harmonic approximation when comparing materials for which different shifts might occur. This posed no problem for the analysis of the ternary materials (see sections 5.1.2 and 5.2.2), since for a given dataset the shift induced by the harmonic approximation is very similar (i.e. none for GaAs, (In,Ga)As, and InAs; and approximately $10\,\mathrm{N\,m^{-1}}$ for GaP, (In,Ga)P, and InP). For the bond-bending force constants, such effects should be negligible, since the potential describing perpendicular vibrations is symmetric (see Fig. 2.5) and the major part of the anharmonic contributions to the variance is caused by k_3.

A second issue is the limited comparability of measurements performed at different facilities. In a homogeneous dataset stemming from one beamline and ideally from the same beamtime, trends between the samples can be detected, even if the uncertainty of

the absolute values is large. In contrast, measurements performed at different beamlines may be subjected to very different experimental conditions, restricting comparisons to the absolute values without the possibility of evaluating more precise relative trends. The measurement of the current dataset was optimised for maximum comparability in the analysis of the ternary alloys and in fact precise trends could be detected in the element-specific effective bond-stretching force constants of (In,Ga)P and (In,Ga)As (see chapter 5). As a result the measurements of the different binary materials are less homogeneous, since they were measured in the beamtimes of the corresponding ternary alloys. Additionally, some data from previous measurements was provided by Mark Ridgway, Australian National University. To account for the resulting experimental differences, a very high number of tests was performed to reliably specify the force constants and to guarantee that differences between the materials show true physical properties.

While it is desirable, to measure all samples of interest in one beamtime (e.g. all (In,Ga)P alloys plus InP and GaP), this approach poses the problem, that the time available for the measurement of each sample decreases compared to the thorough investigation of only one or very few samples per beamtime as performed in studies found in the literature [24, 33]. As a consequence, the data quality of spectra will decrease, when many samples are studied at once, especially in the case of time-consuming temperature-dependent EXAFS measurements. The systematic comparison of temperature-dependent EXAFS results therefore requires a trade-off between measurement homogeneity (i.e. all samples measured in one beamtime) and measurement time per sample (i.e. only one sample per beamtime). Hence, the larger uncertainties of the anisotropy parameters in this work compared to the literature are caused by the use of higher anharmonic contributions in the cumulant formulas, the probably lower data quality originating from the attempt to measure many samples in one beamtime, and the extensive testing procedure trying to eliminate the influence of any experimental differences on the trends under study.

6.3.3 Relationship between bond-stretching force constants, bond-bending force constants and Raman TO frequencies

In diamond, the Raman TO frequencies can be related to the potential parameters describing vibrations parallel and perpendicular to the bond [130]. The relationship can be easily modified to describe binary zinc-blende semiconductors and in harmonic approximation yields

$$\nu_{\mathrm{TO}} = \left(\frac{4(k_{\parallel} + 4k_{\perp})}{3\mu} \right)^{\frac{1}{2}}, \tag{6.3}$$

Table 6.4: Calculated TO frequencies of binary III-V materials. The values were calculated using eq. 6.3.

	TO frequency (THz)	
sample	calc.	exp. [1]
$InP_{HASYLAB}$	11.78	9.14
InP_{PF}	12.93	9.14
$InAs_{SLS}$	9.72	6.59
$InSb_{SLS}$	7.10	5.39
$GaP_{HASYLAB}$	15.57	10.96
GaP_{AS1}	15.57	10.96
$GaAs_{SLS}$	10.36	8.01
$GaAs_{AS1}$	10.44	8.01
$GaSb_{AS1}$	9.59	6.72
$GaSb_{AS2}$	9.94	6.72

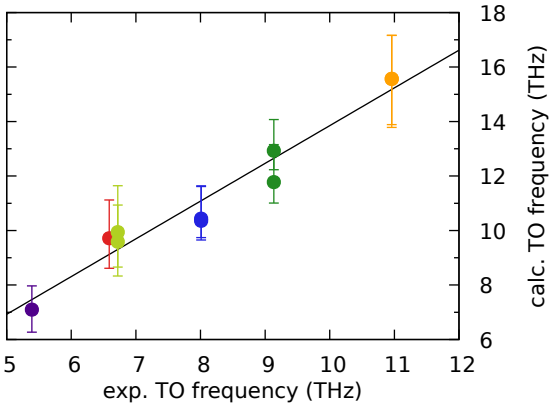

Figure 6.10: Calculated TO frequencies. The values are plotted from Tab. 6.4. The uncertainties are propagated from the minimum and maximum values given in Tab. 6.2. The solid line depicts the best fitting proportionality between experimental and calculated TO frequencies.

where μ is the reduced mass of the bond. The calculated TO frequencies using the bond-stretching force constant $k_{\parallel}$ and bond-bending force constant $k_{\perp}$ given in Tab. 6.2 are presented in Tab. 6.4 together with experimental Raman TO frequencies from the literature [1]. The calculated values are approximately 1.4 times larger than the experimental values for all samples. This relation is depicted in Fig. 6.10.

It is worth noting, that the derivation of the formula assumes intrinsic force constants, while temperature-dependent EXAFS measurements yield effective force constants describing the dynamic behaviour of an embedded bond. To obtain the experimental TO frequencies from the calculation, the intrinsic force constants inserted need to be smaller than the EXAFS force constants. That the EXAFS force constants are larger than the intrinsic force constants implies that the free vibration of an isolated bond is hindered by neighbouring atoms when this bond is embedded in the material. The impairment of the vibration for a material consisting only of one bond species should mainly depend on the crystal structure. This assumption is validated by the fact, that all materials studied in this work share a constant factor between calculated and experimental TO frequencies.

It is noticeable, that the value of InAs does fit well in the curve, despite the peculiar bond-bending force constant discussed earlier. This suggests the possibility that this bond-bending force constant is indeed a real feature of the In–As bond and not an artefact of insufficient data quality.

6.4 Second-nearest neighbour vibrations

Since the variance of the second-nearest neighbour (2NN) distance distribution was modelled by an anharmonic correlated Einstein model, too, effective stretching force constants ($k_{\parallel}=k_0$) for the 2NN pairs Ga–Ga or In–In could be obtained. Values and uncertainties were determined from plots of the whole set of fits, which can be found in appendix C.5. The results are printed in Tab. 6.2 and plotted in Fig. 6.11. For GaAs and InP the values determined are slightly smaller than the literature values [31, 33] shown as black symbols.

6.4.1 Trends with bond length and reduced masses

As a function of bond length depicted in Fig. 6.11a the values roughly follow an r^{-3} trend. Furthermore, it can be seen in Fig. 6.11b, that the relative vibrational frequency of the 2NN pair depends significantly on the intermediate atom species. Understandably, stiffer bonds connecting the atoms increase the 2NN vibrational frequency. Since the 1NN bond-stretching force constant is correlated with the reduced mass of the bond, the 2NN vibrational frequency is plotted as a function of the inverse reduced mass of the 1NN bond in panel c. A clear increase of the 2NN vibrational frequency is visible, where the Ga-containing and In-containing samples lie on different straight lines. The slope for the Ga-containing and the In-containing samples differs by the ratio of their square atomic masses.

As a result, the values of all samples lie on one common line when plotted as a function of the mass parameter $1/(\mu_{1NN}\mu_{2NN}^2)$ as was done in panel d. While it seems reasonable, that the 2NN vibrational frequency depends on both μ_{1NN} and μ_{2NN}, the explanation for the specific dependence observed empirically is unclear yet.

6.4.2 Relation between 1NN and 2NN force constants

The effective force constant determined for the 2NN pair is not the property of a direct bond, but originates from the stretching and bending properties of the connecting 1NN pairs. It is therefore possible to relate the 2NN stretching force constant to the 1NN bond-stretching and bond-bending constants using geometric considerations and the harmonic approximation. The relation describes only static properties since it calculates the forces arising from infinitesimal displacements. Under these assumptions, one obtains

$$k_{2NN} = \frac{k_{\parallel}\, k_{\perp}}{2(k_{\parallel} \sin^2\theta + k_{\perp} \cos^2\theta)}, \tag{6.4}$$

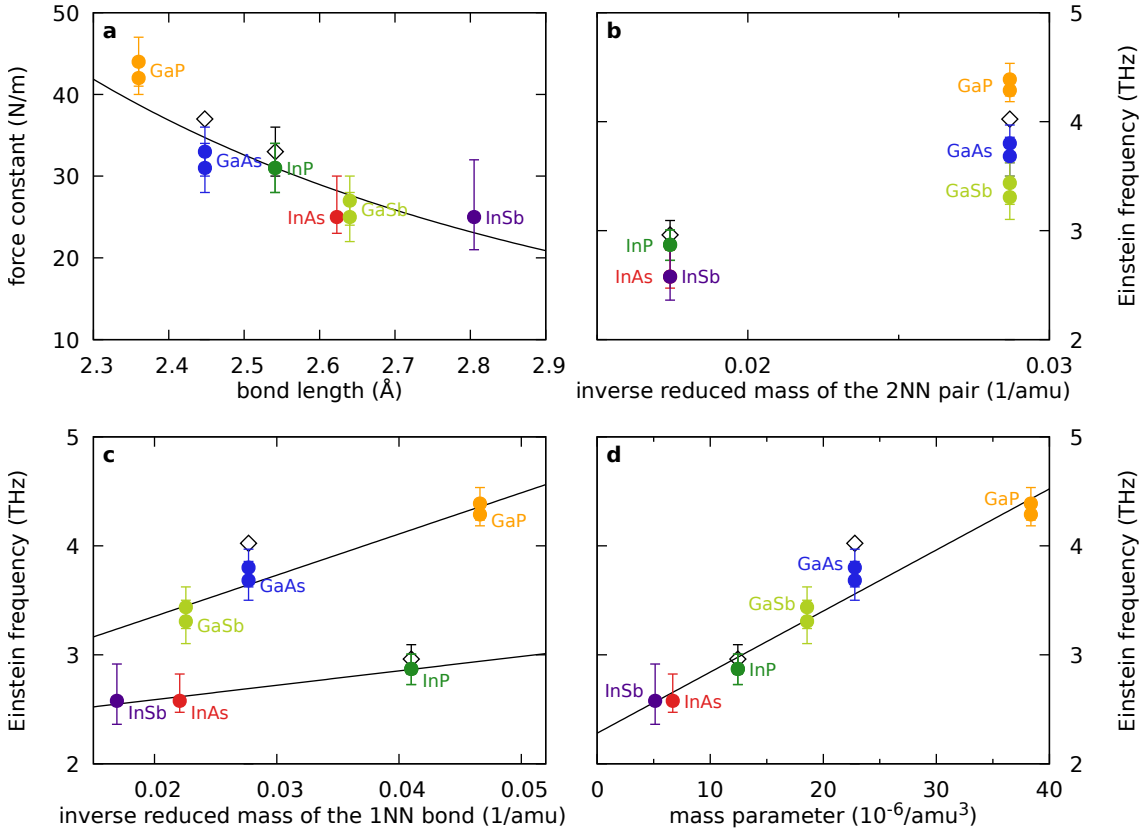

Figure 6.11: 2NN stretching force constants as a function of 1NN bond length and 2NN Einstein vibrational frequencies as a function of mass parameters. Coloured symbols depict the values obtained in this work, while black symbols show the literature data [31, 33]. **a,** The second neighbour stretching force constants decrease with increasing 1NN bond length. The solid black line depicts the best fitting r^{-3} dependence. **b-d,** The force constants from panel a were converted in Einstein vibrational frequencies using the reduced mass of the second-neighbour pair μ_{2NN}. This frequency is plotted as a function of the inverse reduced mass of the second neighbour pair $1/(\mu_{2NN})$ in panel b, the inverse reduced mass of the nearest neighbour bond $1/(\mu_{1NN})$ in panel c, and the mass parameter $1/(\mu_{1NN}\mu_{2NN}^2)$ in panel d. The solid lines depict the linear functions best fitting to the Ga-containing or In-containing samples in panel c and to all samples in panel d.

Table 6.5: Calculated 2NN stretching force constants in binary III-V materials. The values were calculated using eq. 6.4 with $\theta = 35°$.

	2NN force constant ($N\,m^{-1}$)	
sample	calculated	fitted
$InP_{HASYLAB}$	16	31
InP_{PF}	24	31
$InAs_{SLS}$	27	25
$InSb_{SLS}$	16	25
$GaP_{HASYLAB}$	31	42
GaP_{AS1}	31	44
$GaAs_{SLS}$	22	33
$GaAs_{AS1}$	23	31
$GaSb_{AS1}$	23	25
$GaSb_{AS2}$	26	27

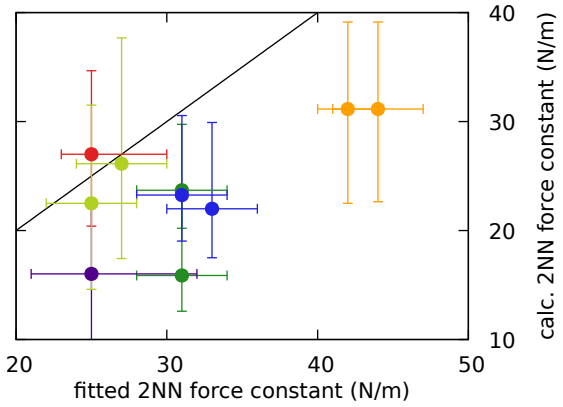

Figure 6.12: Calculated 2NN force constants. The values are plotted from Tab. 6.5. The uncertainties are propagated from the minimum and maximum values given in Tab. 6.2. The solid line depicts the equality between fitted and calculated 2NN stretching force constants.

where θ identifies the angle between the 1NN bond and the line connecting the 2NN pair. For the ideal zinc-blende structure $\theta = \arccos\sqrt{2/3} \approx 35°$. The resulting 2NN stretching force constants are given in Tab. 6.5. While the calculated values are in the right order of magnitude, a direct relationship to the experimental values is not visible in Fig. 6.12.

7 Summary and conclusion

In this work, the vibrational properties of binary III-V zinc-blende semiconductor compounds and their ternary alloys were studied using temperature-dependent extended x-ray absorption fine structure spectroscopy. The set of samples comprised GaP, GaAs, GaSb, InP, InAs, InSb, and the random alloys (In,Ga)P and (In,Ga)As. The measurements were performed on powder samples at the Ga-K and In-K x-ray absorption edge (10 367 eV and 27 940 eV, respectively). Part of the materials were measured in transmission and part in fluorescence mode, depending on the experimental conditions provided by the beamline. The measurement temperatures ranged from 20 K to 300 K.

The EXAFS data was analysed using the path fitting approach with theoretical phase shifts and scattering amplitudes calculated using FEFF9 [45]. To deal efficiently with the temperature-dependent data series, a plugin for the analysis software LARCH [110] was developed, which enabled extensive tests of the analysis parameters and settings. The distance distribution of the neighbouring atoms which underlies the fine structure visible in EXAFS spectra, is usually described using the mean, the variance, the asymmetry parameter, and the kurtosis cumulant of the distribution. Here, the temperature-dependence of the variance, the asymmetry parameter, and the kurtosis cumulant of the distance distribution was parameterised using the anharmonic correlated Einstein model, to obtain the element-specific effective bond-stretching force constants. For the binary compounds, additionally, the temperature-dependence of the difference between bond length and mean lattice site distance was fitted by a harmonic correlated Einstein model to extract effective bond-bending force constants.

For the ternary alloys (In,Ga)P and (In,Ga)As, the element-specific effective bond-stretching force constants were determined as a function of composition. For all four bond species (Ga–P, In–P, Ga–As, and In–As), the values decrease with increasing In content of the sample. In the case of (In,Ga)P, the effective bond-stretching force constants of the Ga–P and In–P bonds, vary almost linearly between the values of the binary parent compounds GaP and InP. In contrast, a pronounced bond-strength inversion is visible in (In,Ga)As. There, the Ga–As bond, which is stiffer than the In–As bond when comparing the binary compounds GaAs and InAs, turns out to be the softer bond in the

ternary alloy. This inversion is caused by a strong composition dependence of the strength of the In–As bond, where the In–As effective bond-stretching force constant in the ternary alloy is larger than the Ga–As effective bond-stretching force constant in GaAs.

The change of the element-specific effective bond-stretching force constants with composition, could be caused either by the change of the intrinsic force constant of the bond or by the change of the vibrational properties through the substitution of neighbouring atoms. To enlarge the basis on which the effects governing the composition dependence of force constants are examined, literature data of Zn(Se,Te) [7] was included in the discussion. It emerges, that the relative change in the bond-stretching force constant induced by alloying shows the same trend as the change induced by hydrostatic pressure (reported for CdTe [8]) when related to the relative change in bond lengths. Therefore, the composition dependence of element-specific effective bond stretching force constants is caused mainly by the intrinsic change of the force constant correlated with the forced change in bond length. Deviations from this common behaviour are visible for the In–As bond in (In,Ga)As and the Zn–Se bond in Zn(Se,Te). These can probably be attributed to coupling effects between the vibrations of the different bond species present in the ternary alloy.

For the binary compounds GaP, GaAs, GaSb, InP, InAs, and InSb, effective bond-stretching and bond-bending force constants were determined. Both effective force constants roughly decrease with increasing bond length. From the force constants the Einstein vibrational frequencies for vibrations parallel and perpendicular to the bond direction can be calculated. For the six materials studied, both Einstein vibrational frequencies show a bilinear dependence on the inverse reduced mass and the Phillips ionicity of the bond. In contrast, the anisotropy parameter quantifying the vibrational anisotropy by the ratio between parallel and perpendicular Einstein vibrational frequency are afflicted with large uncertainties. Therefore, no clear trends are visible when plotting the anisotropy parameter as a function of different material parameters, like reduced mass, atom mass ratio, or Phillips ionicity. The vibrational anisotropy is thought to be linked to the negative thermal expansion observed for many zinc-blende semiconductor compounds at low temperatures [22–24]. However, the large uncertainties of the values determined in this work preclude a correlation of the strength of the negative thermal expansion with the anisotropy parameter.

The large uncertainties of the anisotropy parameter in this work compared to literature values originate from the inclusion of anharmonic contributions in the correlated Einstein model, the somewhat lesser data quality, and the differing experimental conditions. The use of the anharmonic correlated Einstein model is necessary, since the impact of

the harmonic approximation on the force constants varied significantly for the different materials. Since the cause of this effect is unclear, comparisons between the harmonic effective bond-stretching force constants can not reveal, whether the change observed for the harmonic force constants stems from a change of the force constant or from a difference of the force constant shift caused by the harmonic approximation.

To significantly improve the precision of the results, it is necessary to enhance the data quality and to increase the homogeneity of the dataset with respect to the experimental conditions. However, it is difficult to obtain both improvements simultaneously, since a systematic temperature-dependent EXAFS study requires a trade-off between the measurement time devoted to each sample (high data quality) and the number of samples which can be measured in one beamtime (high data homogeneity). A large number of fits using different analysis settings were performed in this work to exclude the possibility that trends seen for the fit results might stem from differing experimental conditions. It would be highly desirable to better understand the influence of the experimental conditions on the EXAFS results in order to improve the comparability between measurements of different beamlines and beamtimes, and to avoid problems with the amplitude reduction factor of the spectra which led to the refusal of several datasets in this work. Higher quality data could in principle enable the precise determination of the anisotropy parameter in order to study correlations with the strength of the negative thermal expansion. Additionally, an open question is, whether the Einstein frequencies of the II-VI semiconductors follow a bilinear dependence on inverse reduced mass and ionicity of the bond similar to the relations found for parallel and perpendicular vibrations in III-V semiconductor compounds in this work. The strong mathematical correlation between the parameters of the effective pair potential limiting the accuracy of the bond-stretching force constants, might be overcome by expanding the measurement range to higher temperature. The anharmonic contributions to the cumulants already used in the analysis should probably enable the description of the temperature dependence to at least a few hundred °C. Such an EXAFS study at elevated temperature may also shed some light on the effects governing the shift in force constants when using the harmonic approximation to parameterise the variance of the distance distribution.

Regarding the bond-stretching force constants and Einstein vibrational frequencies in alloys, the general relationship between the change of the Einstein vibrational frequency and the forced change of the bond length, either by alloying or by hydrostatic pressure, found in this work significantly improves the fundamental understanding of the vibrational behaviour in random semiconductor alloys. Based on this finding, the equivalence

between alloying and hydrostatic pressure with respect to the Einstein frequency change could be tested further by a temperature-dependent EXAFS study under hydrostatic pressure investigating the shorter bond species in a ternary semiconductor alloy. In this case, the alloying leads to an increase of the length of this bond species, while the hydrostatic pressure decreases the bond length. The most interesting state is when the bond length of the bond species under study equals the natural length known from the respective binary compound. If the bond length dependence is the only cause of the frequency change, the Einstein vibrational frequency determined at this point should then equal the value of the binary compound. A promising candidate for this test is the Ga–P bond in (In,Ga)P.

In conclusion, the element-specific effective force constants determined in this work contribute to the basic understanding of atomic vibrations in semiconductor compounds and alloys. Additionally, the extensive set of fits testing different analysis settings provide a substantiated estimate of the accuracy achievable for force constants derived from temperature-dependent EXAFS measurements.

References

[1] S. Adachi. *Properties of Group IV, III-V and II-VI Semiconductors*. Chichester: John Wiley & Sons, 2005.

[2] S. Adachi. *Properties of Semiconductor Alloys*. Chichester: John Wiley & Sons, 2012.

[3] J. C. Woicik. "Local structure determination in strained-layer semiconductors". *Surf. Sci. Rep.* **69**, (2014), 38–53.

[4] C. S. Schnohr. "Compound semiconductor alloys: From atomic-scale structure to bandgap bowing". *Appl. Phys. Rev.* **2**, (2015), 031304.

[5] R. M. Martin. "Elastic Properties of ZnS Structure Semiconductors". *Phys. Rev. B* **1**, (1970), 4005–4011.

[6] H. Neumann. "Interatomic Force Constants and Localized Effective Charges in Sphalerite-Structure Compounds". *Cryst. Res. Technol.* **20**, (1985), 773.

[7] J. Pellicer-Porres, A. Polian, A. Segura, V. Muñoz-Sanjosé, A. Di Cicco and A. Traverse. "X-ray-absorption fine-structure study of $ZnSe_xTe_{1-x}$ alloys". *J. Appl. Phys.* **96**, (2004), 1491.

[8] P. Fornasini, R. Grisenti, T. Irifune, T. Shinmei, O. Mathon, S. Pascarelli and A. D. Rosa. "Bond compressibility and bond Grüneisen parameters of CdTe". *J. Phys.: Condens. Mat.* **30**, (2018), 245402.

[9] R. F. Service. "Is silicon's reign nearing its end?" *Science* **323**, (2009), 1000.

[10] J. A. del Alamo. "Nanometre-scale electronics with III–V compound semiconductors". *Nature* **479**, (Nov. 2011), 317–323.

[11] K. Tomioka, M. Yoshimura and T. Fukui. "A III–V nanowire channel on silicon for high-performance vertical transistors". *Nature* **488**, (Aug. 2012), 189–193.

[12] M. G. Lagally and R. H. Blick. "A 'bed of nails' on silicon". *Nature* **432**, (2004), 450.

[13] Z. L. Yuan, B. E. Kardynal, A. W. Sharpe and A. J. Shields. "High speed single photon detection in the near infrared". *Appl. Phys. Lett.* **91**, (2007), 041114.

[14] G. Ariyawansa, C. J. Reyner, J. M. Duran, J. D. Reding, J. E. Scheihing and E. H. Steenbergen. "Unipolar infrared detectors based on InGaAs/InAsSb ternary superlattices". *Appl. Phys. Lett.* **109**, (2016), 021112.

[15] A. Rogalski, P. Martyniuk and M. Kopytko. "InAs/GaSb type-II superlattice infrared detectors: Future prospect". *Appl. Phys. Rev.* **4**, (2017), 031304.

[16] R. Chen, T.-T. D. Tran, K. Wei Ng, W. Son Ko, L. C. Chuang, F. G. Sedgwick and C. Chang-Hasnain. "Nanolasers grown on silicon". *Nat. Photon.* **5**, (2011), 170–175.

[17] J. Yoon, S. Jo, I. S. Chun, I. Jung, H.-S. Kim, M. Meitl, E. Menard, X. Li, J. Coleman, U. Paik and J. A. Rogers. "GaAs photovoltaics and optoelectronics using releasable multilayer epitaxial assemblies". *Nature* **465**, (2010), 329.

[18] F. Dimroth, M. Grave, P. Beutel, U. Fiedeler, C. Karcher, T. N. D. Tibbits, E. Oliva, G. Siefer, M. Schachtner, A. Wekkeli, A. W. Bett, R. Krause, M. Piccin, N. Blanc, C. Drazek, E. Guiot, B. Ghyselen, T. Salvetat, A. Tauzin, T. Signamarcheix, A. Dobrich, T. Hannappel and K. Schwarzburg. "Wafer bonded four-junction GaInP/GaAs//GaInAsP/GaInAs concentrator solar cells with 44.7% efficiency". *Prog. Photovolt: Res. Appl.* **22**, (2014), 277.

[19] M. A. Green and S. P. Bremner. "Energy conversion approaches and materials for high-efficiency photovoltaics". *Nat. Mater.* **16**, (Jan. 2017), 23–34.

[20] M. M. May, H.-J. Lewerenz, D. Lackner, F. Dimroth and T. Hannappel. "Efficient direct solar-to-hydrogen conversion by in situ interface transformation of a tandem structure". *Nat. Commun.* **6**, (2015), 8286.

[21] J. Gu, Y. Yan, J. L. Young, K. Xerxes Steirer, N. R. Neale and J. A. Turner. "Water reduction by a p-$GaInP_2$ photoelectrode stabilized by an amorphous TiO_2 coating and a molecular cobalt catalyst". *Nat. Mater.* **15**, (2016), 456.

[22] T. H. K. Barron, J. G. Collins and G. K. White. "Thermal expansion of solids at low temperatures". *Adv. Phys.* **29**, (1980), 609.

[23] G. D. Barrera, J. A. O. Bruno, T. H. K. Barron and N. L. Allan. "Negative thermal expansion". *J. Phys.: Condens. Mat.* **17**, (2005), R217.

[24] N. Abd el All, G. Dalba, D. Diop, P. Fornasini, R. Grisenti, O. Mathon, F. Rocca, B. Thiodjio Sendja and M. Vaccari. "Negative thermal expansion in crystals with the zincblende structure: an EXAFS study of CdTe". *J. Phys.: Condens. Mat.* **24**, (2012), 115403.

[25] J. C. Mikkelsen Jr. and J. B. Boyce. "Atomic-Scale Structure of Random Solid Solutions: Extended X-Ray-Absorption Fine-Structure Study of $Ga_{1-x}In_xAs$". *Phys. Rev. Lett.* **49**, (1982), 1412–1415.

[26] A. Balzarotti. "Lattice distortions around atomic substitutions in II-VI alloys". *Physica* **146B**, (1987), 150–175.

[27] P. Letardi, N. Motta and A. Balzarotti. "Atomic bonding and thermodynamic properties of pseudo-binary semiconducting alloys". *J. Phys. C: Solid State* **20**, (1987), 2853–2884.

[28] Z. Wu, K. Lu, Y. Wang, J. Dong, H. Li, C. Li and Z. Fang. "Extended x-ray-absorption fine-structure study of $GaAs_xP_{1-x}$ semiconducting random solid solutions". *Phys. Rev. B* **48**, (1993), 8694.

[29] C. S. Schnohr, L. L. Araujo, P. Kluth, D. J. Sprouster, G. J. Foran and M. C. Ridgway. "Atomic-scale structure of $Ga_{1-x}In_xP$ alloys measured with extended x-ray absorption fine structure spectroscopy". *Phys. Rev. B* **78**, (2008), 115201.

[30] D. N. Talwar, Z. C. Feng, J.-F. Lee and P. Becla. "Structural and dynamical properties of Bridgman-grown $CdSe_x$ Te_{1-x} ($0 < x < 0.35$) ternary alloys". *Phys. Rev. B* **87**, (2013), 165208.

[31] C. S. Schnohr, P. Kluth, L. L. Araujo, D. J. Sprouster, A. P. Byrne, G. J. Foran and M. C. Ridgway. "Anisotropic vibrations in crystalline and amorphous InP". *Phys. Rev. B* **79**, (2009), 195203.

[32] M. Krbal, A. V. Kolobov, B. Hyot, B. André, P. Fons, R. E. Simpson, T. Uruga, H. Tanida and J. Tominaga. "Amorphous InSb: Longer bonds yet higher density". *J. Appl. Phys.* **108**, (2010), 023506. DOI: 10.1063/1.3436592.

[33] S. I. Ahmed, G. Aquilanti, N. Novello, L. Olivi, R. Grisenti and P. Fornasini. “Local vibrational properties of GaAs studied by extended X-ray absorption fine structure”. *J. Chem. Phys.* **139**, (2013), 164512.

[34] P. Fornasini and R. Grisenti. “On EXAFS Debye-Waller factor and recent advances”. *J. Synchr. Rad.* **22**, (2015), 1242.

[35] G. Bunker. *Introduction to XAFS*. New York: Cambridge University Press, 2010.

[36] S. Calvin. *XAFS for Everyone*. Boca Raton: CRC Press, 2013.

[37] J. J. Rehr and R. C. Albers. “Theoretical approaches to x-ray absorption fine structure”. *Rev. Mod. Phys.* **72**, (July 2000).

[38] B. Ravel. *ATHENA Manual*. 2016.

[39] C. S. Schnohr. “Atomic-scale structure of crystalline InP, amorphous InP and crystalline $Ga_{1-x}In_xP$ alloys”. PhD thesis. The Australian National University, June 2009.

[40] G. Bunker. “Application of the Ratio Method of EXAFS analysis to disordered systems”. *Nucl. Instrum. Methods* **207**, (1983), 437.

[41] D. E. Sayers, E. A. Stern and F. W. Lytle. “New technique for Investigating Noncrystalline Structures: Fourier Analysis of the Extended X-Ray-Absorption Fine Structure”. *Phys. Rev. Lett.* **27**, (1971), 1204.

[42] G. T. Seidler, D. R. Mortensen, A. J. Remesnik, J. I. Pacold, N. A. Ball, N. Barry, M. Styczinski and O. R. Hoidn. “A laboratory-based hard x-ray monochromator for high-resolution x-ray emission spectroscopy and x-ray absorption near edge structure measurements”. *Rev. Sci. Instrum.* **85**, (2014), 113906.

[43] G. Dalba and P. Fornasini. “EXAFS Debye-Waller Factor and Thermal Vibrations of Crystals”. *J. Synchr. Rad.* **4**, (1997), 243–255.

[44] C. S. Schnohr and M. C. Ridgway, eds. *X-Ray Absorption Spectroscopy of Semiconductors*. Berlin: Springer, 2015. ISBN: 978-3662443613.

[45] J. J. Rehr, J. J. Kas, F. D. Vila, M. P. Prange and K. Jorissen. “Parameter-free calculations of X-ray spectra with FEFF9”. *Phys. Chem. Chem. Phys.* **12**, (2010), 5503–5513.

[46] P. Fornasini. “Study of lattice dynamics via extended x-ray absorption fine structure”. *J. Phys.: Condens. Mat.* **13**, (2001), 7859.

[47] J. Haug, A. Chassé, R. Schneider, H. Kruth and M. Dubiel. “Thermal expansion and interatomic potentials of silver revealed by extended x-ray absorption fine structure spectroscopy using high-order perturbation theory”. *Phys. Rev. B* **77**, (2008), 184115.

[48] P. Fornasini, S. a Beccara, G. Dalba, R. Grisenti, A. Sanson, M. Vaccari and F. Rocca. “Extended x-ray-absorption fine-structure measurements of copper: Local dynamics, anharmonicity, and thermal expansion”. *Phys. Rev. B* **70**, (2004), 174301.

[49] T. Yokoyama. “Path-integral effective-potential theory for EXAFS cumulants compared with the second-order perturbation”. *J. Synchr. Rad.* **6**, (1999), 323–325.

[50] P. Fornasini, R. Grisenti, M. Dapiaggi, G. Agostini and T. Miyanaga. “Nearest-neighbour distribution of distances in crystals from extended X-ray absorption fine structure”. *J. Chem. Phys.* **147**, (2017), 044503.

[51] P. S. Branicio, J. P. Rino, F. Shimojo, R. K. Kalia, A. Nakano and P. Vashishta. "Molecular dynamics study of structural, mechanical, and vibrational properties of crystalline and amourphous $Ga_{1-x}In_xAs$ alloys". *J. Appl. Phys.* **94**, (2003), 3840–3848.

[52] S. T. Murphy, A. Chroneos, C. Jiang, U. Schwingenschlögl and R. W. Grimes. "Deviations from Vegard's law in ternary III-V alloys". *Phys. Rev. B* **82**, (2010), 073201.

[53] F. El Haj Hassan, B. Al Shafaay, H. Meradji, S. Ghemid, H. Belkhir and M. Korek. "Ab initio study of the fundamental properties of HgSe, HgTe and their $HgSe_xTe_{1-x}$ alloys". *Phys. Scr.* **84**, (2011), 065601.

[54] A. Nassour. "First-principles calculations of structural properties and lattice dynamics in $ZnSe_xTe_{1-x}$ alloys". *Comp. Mater. Sc.* **77**, (2013), 403.

[55] M. Schenk, I. Hähnert, L. T. H. Duong and H.-H. Niebsch. "Validity of the Lattice-Parameter Vegard-Rule in $Cd_{1-x}Zn_xTe$ Solid Solutions". *Cryst. Res. Technol.* **31**, (1996), 665.

[56] T. Ganguli, J. Mazher, A. Polian, S. K. Deb, F. Villain, O. Pagès, W. Paszkowicz and F. Firszt. "Lattice relaxation in the highly-contrasted $Zn_{1-x}Be_xSe$ alloy: An extended x-ray absorption fine structure study". *J. Appl. Phys.* **108**, (2010), 083539.

[57] N. W. Ashcroft and N. D. Mermin. *Solid State Physics*. Thomson Learning, 1976.

[58] S. Hunklinger. *Festkörperphysik*. München: Oldenbourg Wissenschaftsverlag, 2007.

[59] P. N. Keating. "Effect of Invariance Requirements on the Elastic Strain Energy of Crystals with Application to the Diamond Structure". *Phys. Rev.* **145**, (1966), 637.

[60] A. S. Verma. "Bond-stretching and bond-bending force constant of binary tetrahedral ($A^{III}B^V$ and $A^{II}B^{VI}$) semiconductors". *Phys. Lett. A* **372**, (2008), 7196–7198.

[61] M. B. Kanoun, S. Goumri-Said, A. E. Merad, G. Merad, J. Cibert and H. Aourag. "Zinc-blende AlN and GaN under pressure: structural, electronic, elastic and piezoelectric properties". *Semicond. Sci. Technol.* **19**, (2004), 1220.

[62] L. Louail, D. Maouche and A. Hachemi. "Elastic properties of InAs under pressure up to 18 GPa". *Mat. Lett.* **60**, (2006), 3269.

[63] S. Aouadi, P. Rodriguez-Hernandez, K. Kassali and A. Muñoz. "Lattice dynamics properties of zinc-blende and Nickel arsenide phases of AlP". *Phys. Lett. A* **372**, (2008), 5340.

[64] A. Bouhemadou, R. Khenata, M. Kharoubi, T. Seddik, A. H. Reshak and Y. Al-Douri. "FP-APW + lo calculations of the elastic properties in zinc-blende III-P compounds under pressure effects". *Comp. Mater. Sc.* **45**, (2009), 474.

[65] C. I. Ribeiro-Silva, J. P. Rino, L. G. V. Gonçalves and A. Picinin. "An effective interaction potential for gallium phosphide". *J. Phys.: Condens. Mat.* **23**, (2011), 055801.

[66] H. Salehi, H. A. Badehian and M. Farbod. "First principle study of the physical properties of semiconducting binary antimonide compounds under hydrostatic pressures". *Mat. Sci. Semicon. Proc.* **26**, (2014), 477.

[67] A. R. Degheidy and E. B. Elkenany. "Electronic, optical, and mechanical properties of BN, AlN, and InN with zinc-blende structure under pressure". *Chin. Phys. B* **26**, (2017), 086103.

[68] F. C. Peiris, U. Bindley, J. K. Furdyna, H. Kim, A. K. Ramdas and M. Grimsditch. "Determination of the dispersion of the index of refraction and the elastic moduli for molecular-beam-epitaxy-grown $Zn_{1-x}Be_xSe$ alloys". *Appl. Phys. Lett.* **79**, (2001), 473.

[69] K. Bouamama, K. Daoud and K. Kassali. "Ab initio calculations in the virtual-crystal approximation of the structural and the elastic properties of BeS_xSe_{1-x} alloys under high pressure". *Modelling Simul. Mater. Sci. Eng.* **13**, (2005), 1153.

[70] S. Mnasri, S. Abdi-Ben Nasrallah, N. Sfina, N. Bouarissa and M. Said. "Electronic, lattice vibration and mechanical properties of CdTe, ZnTe, MnTe, MgTe, HgTe and their ternary alloys". *Semicond. Sci. Technol.* **24**, (2009), 095008.

[71] P. S. Vyas, P. N. Gajjar, B. Y. Thakore and A. R. Jani. "Elastic properties of $Ga_xIn_{1-x}P$ semiconductor". *Physica B* **406**, (2011), 4412.

[72] A. Boumaza, S. Ghemid, Z. Chouahda, H. Meradji and F. El Haj Hassan. "First-principles calculations of the structural, electronic, elastic, phase diagram and thermal properties of $Zn_{1-x}Be_xTe$ ternary alloy". *Phys. Scr.* **86**, (2012), 035703.

[73] M. A. Ghebouli, H. Choutri, N. Bouarissa, B. Ghebouli, M. Fatmi and E. Uçgun. "Ab initio calculation of fundamental properties of $Ca_xMg_{1-x}A$ (A=Se and Te) alloys in the rock-salt structure". *Physica E* **49**, (2013), 83.

[74] S. Saib, N. Bouarissa, P. Rodríguez-Hernández and A. Muñoz. "Composition-dependent elastic modulus, vibration frequency and polaron properties of $ZnSe_xTe_{1-x}$ system". *Opt. Mater.* **35**, (2013), 2303.

[75] J. Berggren, M. Hanke and A. Trampert. "Bowing effect in elastic constants of dilute Ga(As,N) alloys". *Appl. Phys. Lett.* **108**, (2016), 183106.

[76] M. Zafar, M. Shakil, S. Ahmed, M. Raza-ur-rehman Hashmi, M. A. Choudhary and Naeem-ur-Rehman. "Ab initio study of structural, electronic and elastic properties of $CdSe_{1-x}S_x$ semiconductor". *Solar Energy* **158**, (2017), 63.

[77] S. Gehrsitz, H. Sigg, N. Herres, K. Bachem, K. Köhler and F. K. Reinhart. "Compositional dependence of the elastic constants and the lattice parameter of $Al_xGa_{1-x}As$". *Phys. Rev. B* **60**, (Oct. 1999), 11601.

[78] K. Biswas, A. Franceschetti and S. Lany. "Generalized valence-force-field model of (Ga,In)(N,P) ternary alloys". *Phys. Rev. B* **78**, (2008), 085212.

[79] M. T. Dove. *Structure and Dynamics: an atomic view of materials*. Oxford master series in condensed matter physics. New York: Oxford University Press, 2010.

[80] D. L. Price, J. M. Rowe and R. M. Nicklow. "Lattice Dynamics of Grey Tin and Indium Antimonide". *Phys. Rev. B* **3**, (1971), 1268.

[81] B. Hennion, F. Moussa, G. Pepy and K. Kunc. "Normal modes of vibrations in ZnSe". *Phys. Lett. A* **36**, (1971), 376.

[82] J. M. Rowe, R. M. Nicklow, D. L. Price and K. Zanio. "Lattice dynamics of cadmium telluride". *Phys. Rev. B* **10**, (1974), 671.

[83] N. Vagelatos, D. Wehe and J. S. King. "Phonon dispersion and phonon densities of states for ZnS and ZnTe". *J. Chem. Phys.* **60**, (1974), 3613.

[84] P. H. Borcherds, G. F. Alfrey, D. H. Saunderson and A. D. B. Woods. “Phonon dispersion curves in indium phosphide”. *J. Phys. C : Solid State Phys.* **8**, (1975), 2022.

[85] P. H. Borcherds, K. Kunc, G. F. Alfrey and R. L. Hall. “The lattice dynamics of gallium phosphide”. *J. Phys. C : Solid State Phys.* **12**, (1979), 4699.

[86] D. Strauch and B. Dorner. “Phonon dispersion in GaAs”. *J. Phys.: Condens. Mat.* **2**, (1990), 1457–1474.

[87] P. H. Borcherds and K. Kunc. “The lattice dynamics of indium pnictides”. *J. Phys. C : Solid State Phys.* **11**, (1978), 4145–4155.

[88] B. D. Rajput and D. A. Browne. “Lattice dynamics of II-VI materials using the adiabatic bond-charge model”. *Phys. Rev. B* **53**, (1996), 9052.

[89] B. Weinstein, J. B. Renucci and M. Cardona. “Effect of hydrostatic pressure on the second order Raman spectrum of GaP”. *Solid State Commun.* **12**, (1973), 473–479.

[90] E. Jahne, W. Pilz, M. Giehler and L. Hildisch. “Non-Isodisplacement of P Atoms in Long-Wavelength Optical Phonons in $In_{1-x}Ga_xP$”. *Phys. Stat. Sol. B* **91**, (1979), 155.

[91] T. Kato, T. Matsumoto and T. Ishida. “Raman Spectral Behavior of In_1-xGa_xP (0<x<1)”. *Jpn. J. Appl. Phys.* **27**, (1988), 983.

[92] J. Groenen, R. Carles, G. Landa, C. Guerret-Piécourt, C. Fontaine and M. Gendry. “Optical-phonon behavior in $Ga_{1-x}In_xAs$: The role of microscopic strains and ionic plasmon coupling”. *Phys. Rev. B* **58**, (1998), 10452–10462.

[93] O. Pagès, A. V. Postnikov, M. Kassem, A. Chafi, A. Nassour and S. Doyen. “Unification of the phonon mode behavior in semiconductor alloys: Theory and ab initio calculations”. *Phys. Rev. B* **77**, (2008), 125208.

[94] O. Pagès, J. Souhabi, A. V. Postnikov and A. Chafi. “Percolation versus cluster models for multimode vibration spectra of mixed crystals: GaAsP as a case study”. *Phys. Rev. B* **80**, (2009), 035204.

[95] I. F. Chang and S. S. Mitra. “Long wavelength optical phonons in mixed crystals”. *Adv. Phys.* **20**, (1971), 359.

[96] O. Pagès, T. Tite, K. Kim, P. A. Graf, O. Maksimov and M. C. Tamargo. “Percolation picture for long wave phonons in zinc-blende mixed crystals: from (Zn,Be) chalcogenides to (Ga,In)As”. *J. Phys.: Condens. Mat.* **18**, (2006), 577.

[97] R. Hajj Hussein, O. Pagès, S. Doyen-Schuler, H. Dicko, A. V. Postnikov, F. Firszt, A. Marasek, W. Paszkowicz, A. Maillard, L. Broch and O. Gorochov. “Percolation-type multi-phonon pattern of Zn(Se,S): Backward/forward Raman scattering and ab initio calculations”. *J. Alloy. Compd.* **644**, (2015), 704–720.

[98] A. Nassour, J. Hugel and A. V. Postnikov. “Linearized force constants method for lattice dynamics in mixed semiconductors”. *J. Phys.: Conf. Ser.* **92**, (2007), 012139.

[99] N. Abd el All, B. Thiodjio Sendja, R. Grisenti, F. Rocca, D. Diop, O. Mathon, S. Pascarelli and P. Fornasini. “Accuracy evaluation in temperature-dependent EXAFS measurements of CdTe”. *J. Synchr. Rad.* **20**, (2013), 603–613.

[100] G. Dalba, P. Fornasini, R. Grisenti, D. Pasqualini, D. Diop and F. Monti. “Anharmonicity effects on the extended x-ray-absorption fine structure: The case of cadmium selenide”. *Phys. Rev. B* **58**, (1998), 4793.

[101] G. Dalba, P. Fornasini, R. Grisenti and J. Purans. “Sensitivity of Extended X-Ray-Absorption Fine Structure to Thermal Expansion”. *Phys. Rev. Lett.* **82**, (1999), 4240.

[102] M. Vaccari, R. Grisenti, P. Fornasini, F. Rocca and A. Sanson. “Negative thermal expansion in CuCl: An extended x-ray absorption fine structure study”. *Phys. Rev. B* **75**, (2007), 184307.

[103] J. Purans, N. D. Afify, G. Dalba, R. Grisenti, S. De Panfilis, A. Kuzmin, V. I. Ozhogin, F. Rocca, A. Sanson, S. I. Tiutiunnikov and P. Fornasini. “Isotopic Effect In Extended X-Ray-Absorption Fine Structure of Germanium”. *Phys. Rev. Lett.* **100**, (2008), 055901.

[104] Z. S. Hussain, E. Wendler, W. Wesch, G. J. Foran, C. S. Schnohr, D. J. Llewellyn and M. C. Ridgway. “Rapid ion-implantation-induced amorphization of $In_xGa_{1-x}As$ relative to InAs and GaAs”. *Phys. Rev. B* **79**, (2009), 085202.

[105] S. Decoster, C. J. Glover, B. Johannessen, R. Giulian, D. J. Sprouster, P. Kluth, L. L. Araujo, Z. S. Hussain, C. S. Schnohr, H. Salama, F. Kremer, K. Temst, A. Vantomme and M. C. Ridgway. “Lift-off protocols for thin films for use in EXAFS experiments”. *J. Synchr. Rad.* **20**, (2013), 426–432.

[106] G. Götz and K. Gärtner. *High Energy Ion Beam Analysis of Solids*. Berlin: Akademie-Verlag Berlin, 1988.

[107] R. F. Egerton. *Physical Principles of Electron Microscopy. An Introduction to TEM, SEM, and AEM*. Springer Science + Business Media, Inc, 2005.

[108] M. Thompson. *http://www.genplot.com/index.htm*.

[109] A. C. Thompson and D. Vaughan. *X-RAY DATA BOOKLET*. 2nd ed. Berkeley: Lawrence Berkeley National Laboratory, 2001.

[110] M. Newville. “Larch: An Analysis Package for XAFS and Related Spectroscopies”. *J. Phys.: Conf. Ser.* **430**, (2013), 012007.

[111] C. S. Schnohr, L. L. Araujo and M. C. Ridgway. “Temperature-Dependent Second Shell Interference in the First Shell Analysis of Crystalline InP X-ray Absorption Spectroscopy Data”. *J. Phys. Soc. Jpn.* **83**, (2014), 094602.

[112] E. Riedel. *Anorganische Chemie*. 6th ed. Berlin: Walter de Gruyter, 2004.

[113] A. Balzarotti, N. Motta, A. Kisiel, M. Zimnal-Starnawska, M. T. Czyzyk and M. Podgórny. “Model of th local structure of random ternary alloys: Experiment versus theory”. *Phys. Rev. B* **31**, (June 1985), 7526.

[114] M. Hadjab, S. Berrah, H. Abid, M. I. Ziane, H. Bennacer and B. G. Yalcin. “Full-potential calculations of structural and optoelectronic properties of cubic indium gallium arsenide semiconductor alloys”. *Optik* **127**, (2016), 9280.

[115] S. Kumar, T. K. Maurya and S. Auluck. “Structural, Electronic, and Optical Properties of $In_xGa_{1-x}As$ Alloys by Full Potential Linear Augmented Plane Wave Method”. *Jpn. J. Appl. Phys.* **47**, (2008), 5417.

[116] J. C. Woolley and B. A. Smith. "Solid Solution in $A^{III}B^{V}$ Compounds". *Proc. Phys. Soc.* **72**, (1958), 214–223.

[117] I. Katayama, T. Nakai, T. Inomoto and Z. Kozuka. "Activity measurements of Ga in GaAs-InAs solid solutions by the EMF method". *Mater. Trans.* **30**, (1989), 354.

[118] O. Pagès, A. Chafi, D. Fristot and A. V. Postnikov. "(Ga,In)P: A standard alloy in the classification of phonon mode behavior". *Phys. Rev. B* **73**, (2006), 165206.

[119] M. Durandurdu and D. A. Drabold. "Ab initio simulation of high-pressure phases of GaAs". *Phys. Rev. B* **66**, (2002), 045209.

[120] H. Rücker and M. Methfessel. "Anharmonic Keating model for group-IV semiconductors with application to the lattice dynamics in alloys af Si, Ge, and C". *Phys. Rev. B* **52**, (1995), 11059–11072.

[121] N. N. Sirota, A. M. Antiukhov and A. A. Sidorov. "Temperature dependence of the thermal expansion coefficient for gallium and indium phosphide and arsenide in the range of 7-310K according to the x-ray diffraction study". *Dokl. Akad. Nauk SSSR* **277**, (1984), 1379.

[122] S. I. Novikova and N. K. Abrikosov. "Тепловое расширение AlSb, GaSb, ZnTe и HgTe при низких температурах". *Sov. Phys. Solid State* **5**, (1963), 2138.

[123] D. F. Gibbons. "Thermal Expansion of Some Crystals with the Diamond Structure". *Phys. Rev.* **112**, (1958), 136.

[124] B. Ravel and M. Newville. "ATHENA, ARTEMIS, HEPHAESTUS: data analysis for X-ray absorption spectroscopy using IFEFFIT". *J. Synchr. Rad.* **12**, (2005), 537–541.

[125] M. Bauer and H. Bertagnolli. "The Amplitude Reduction Factor and the Cumulant Expansion Method: Crucial Factors in the Structural Analysis of Alkoxide Precursors in Solution". *J. Phys. Chem. B* **111**, (2007).

[126] G. G. Li, F. Bridges and C. H. Booth. "X-ray-absorption fine-structure standards: A comparison of experiment and theory". *Phys. Rev. B* **52**, (1995).

[127] P. Vashishta, R. K. Kalia and J. P. Rino. "Interaction potential for SiO_2: A molecular-dynamics study of structural correlations". *Phys. Rev. B* **41**, (1990), 12197.

[128] P. S. Branicio, J. P. Rino, C. K. Gan and H. Tsuzuki. "Interaction potential for indium phosphide: a molecular dynamics and first-principles study of the elastic constants, generalized stacking fault and surface energies". *J. Phys.: Cond. Matter* **21**, (2009), 095002.

[129] J. P. Rino, G. de Oliveira Cardozo and A. Picinin. "Atomistic Modeling of the Structural and Thermal Conductivity of the InSb". *Comp. Mater. Cont.* **12**, (2009), 145.

[130] R. Vogelgesang, A. K. Ramdas, S. Rodriguez, M. Grimsditch and T. R. Anthony. "Brillouin and Raman scattering in natural and isotopically controlled diamond". *Phys. Rev. B* **54**, (Aug. 1996), 3989.

[131] D. N. Talwar, D. Sofranko, C. Mooney and S. Tallo. "Elastic, structural, bonding, and defect properties of zinc-blende BN, AlN, GaN, InN and their alloys". *Mat. Sci. Eng.* **B90**, (2002), 269.

[132] L. De Caro, C. Giannini, L. Tapfer, H.-P. Schönherr, L. Däweritz and K. H. Ploog. "Validity of Vegard's rule for the lattice parameter and the stiffness elastic constant ratios of the AlGaAs ternary compound". *Solid State Commun.* **108**, (1998), 599.

[133] D. Zhou and B. F. Usher. "Deviation of the AlGaAs lattice constant from Vegard's law". *J. Phys. D: Appl. Phys.* **34**, (2001), 1461.

[134] F. Germini, C. Bocchi, C. Ferrari, S. Franchi, A. Baraldi, R. Magnanini, D. De Salvador, M. Berti and A. V. Drigo. "Assessment of Vegard's law validity in the $Ga_{1-x}Al_xSb$/GaSb epitaxial system". *J. Phys. D: Appl. Phys.* **32**, (1999), A12.

[135] S. Drablia, H. Meradji, S. Ghemid, S. Labidi and B. Bouhafs. "First principles calculations of structural, electronic, thermodynamic and optical properties of $BAs_{1-x}P_x$ alloy". *Phys. Scr.* **79**, (2009), 045002.

[136] H. Baaziz, Z. Charifi, F. El Haj Hassan, S. J. Hashemifar and H. Akbarzadeh. "FP-LAPW investigations of $Zn_{1-x}Be_xS$, $Zn_{1-x}Be_xSe$ and $Zn_{1-x}Be_xTe$ ternary alloys". *Phys. Stat. Sol. B* **243**, (2006), 1296.

[137] M. Ameri, D. Rached, M. Rabah, F. El Haj Hassan, R. Khenata and M. Doui-Aici. "First principles study of structural and electronic properties of $Be_xZn_{1-x}S$ and $Be_xZn_{1-x}Te$ alloys". *Phys. Stat. Sol. B* **245**, (2008), 106.

[138] W. Paszkowicz, K. Godwod, J. Domagała, F. Firszt, J. Szatkowski, H. Męczyńska, S. Łęgowski and M. Marczak. "Lattice parameter, microhardness and energy gap of bulk $Zn_{1-x}Be_xSe$ alloys". *Solid State Commun.* **107**, (1998), 735.

[139] B. Jobst, D. Hommel, U. Lunz, T. Gerhard and G. Landwehr. "E_0 band-gap energy and lattice constant of ternary $Zn_{1-x}Mg_xSe$ as functions of composition". *Appl. Phys. Lett.* **69**, (1996), 97.

[140] A. Haloui, Y. Feutelais and B. Legendre. "Experimental study of the ternary system Cd-Te-Zn". *J. Alloy. Compd.* **260**, (1997), 179.

[141] S. Stolyarova, F. Edelman, A. Chack, A. Berner, P. Werner, N. Zakharov, M. Vytrykhivsky, R. Beserman, R. Weil and Y. Nemirovsky. "Structure of CdZnTe films on glass". *J. Phys. D: Appl. Phys.* **41**, (2008), 065402.

[142] J. C. Woolley and B. Ray. "Solid solution in $A^{II}B^{VI}$ tellurides". *J. Phys. Chem. Solids* **13**, (1960), 151.

[143] F. El Haj Hassan and B. Amrani. "Structural, electronic and thermodynamic properties of magnesium chalcogenide ternary alloys". *J. Phys.: Condens. Mat.* **19**, (2007), 386234.

[144] C. H. Booth and F. Bridges. "Improved Self-Absorption Correction for Fluorescence Measurements of Extended X-Ray Absorption Fine-Structure". *Physica Scripta* **T115**, (2005), 202.

Most figures in this work were created using `gnuplot` (www.gnuplot.info). Schemata were drawn with `metapost` (www.tug.org/metapost.html). Figure 3.1a was created using `XCrySDen` (http://www.xcrysden.org).

A Additional material properties

A.1 Deviations of the lattice constant from Vegard's law

Table A.1: Deviations from Vegard's law for the lattice constant in random ternary III-V alloys. It is indicated whether the lattice parameter of the alloy is larger ('deviation: up') or smaller ('deviation: down') than expected from Vegard's law. If the lattice constant follows Vegard's law, this is specified as 'no deviation'. Some materials show an S-shaped deviation where the lattice constant is smaller than expected in one part of the compositional range and larger in another part.

material	deviation	calculation	experimental data
(Al,B)N	down	[131]	-
(Ga,B)N	down	[131]	-
(Ga,Al)N	down	[131]	-
(In,B)N	down	[131]	-
(In,Al)N	down	[131]	-
(In,Ga)N	down	[131]	-
(Al,B)As	down	[52]	-
(Ga,B)As	down	[52]	-
(Ga,Al)As	no	-	[132]
(Ga,Al)As	up	[52]	[2, 77, 133]
(In,B)As	down	[52]	-
(In,Al)As	down	[52]	-
(In,Ga)As	no	[115]	[116, 117]
(In,Ga)As	up	[51, 114]	-
(In,Ga)As	down	[52]	-
(Ga,Al)Sb	up	-	[2, 134]
(In,Al)Sb	S	-	[116]
(In,Ga)Sb	no	-	[116]
B(P,As)	up	[135]	-
In(As,Sb)	S	-	[116]

Table A.2: Deviations from Vegard's law for the lattice constant in random ternary II-VI alloys. The description of the different deviations is the same as in Tab. A.1

material	deviation	calculation	experimental data
(Zn,Be)S	up	[136, 137]	-
(Zn,Be)Se	no	-	[138]
(Zn,Be)Se	up	[136]	-
(Zn,Mg)Se	up	-	[139]
(Zn,Be)Te	up	[72, 136, 137]	-
(Cd,Zn)Te	no	-	[55, 140, 141]
(Cd,Zn)Te	down	-	[142]
(Hg,Zn)Te	down	-	[142]
(Cd,Hg)Te	down	-	[142]
Be(S,Se)	up	[69]	-
Mg(S,Se)	up	[143]	-
Mg(S,Te)	up	[143]	-
Mg(Se,Te)	up	[143]	-
Zn(Se,Te)	down	[54]	-
Cd(S,Se)	no	[76]	-
Hg(Se,Te)	up	[53]	-

A.2 Elastic force constants in zinc-blende materials

Table A.3: Force constants determined from elastic constants. The values are from the literature [6]. They are also plotted in Fig. 3.2a.

material	lattice constant (Å)	α ($N\,m^{-1}$)	β ($N\,m^{-1}$)
AlSb	6.136	35.74	6.63
GaP	5.451	48.57	10.4
GaAs	5.635	43.34	8.88
GaSb	6.096	34.42	7.16
InP	5.869	44.29	6.26
InAs	6.058	37.18	5.47
InSb	6.479	30.44	4.73

material	lattice constant (Å)	α ($N\,m^{-1}$)	β ($N\,m^{-1}$)
ZnS	5.410	44.73	4.36
ZnSe	5.669	38.61	4.65
ZnTe	6.104	32.04	4.49
CdTe	6.481	29.44	2.48
HgSe	6.084	37.43	2.37
HgTe	6.461	29.32	2.54

A.3 Influence of hydrostatic pressure on elastic force constants

Since the EXAFS results show a material-independent relation between the Einstein vibrational frequency and the bond length, it is interesting to test whether the force constants determined from elastic constants show a similar trend. To do this, theoretical predictions of elastic constants under hydrostatic pressure, which are available for a range of zinc-blende materials, where compiled from the literature. Predictions can be drawn from density functional calculations [61, 62, 64, 66], molecular dynamics calculations [65, 128], and calculations using the empirical pseudo-potential method [67]. Only studies reporting the elastic constants and the bond lengths as a function of pressure were used. From the pressure-dependent elastic constants, the force constant α was calculated using the relations given in the literature [5], but neglecting the terms containing the dynamic effective charge. To increase the comparability with the trend observed for the Einstein vibrational frequencies, the elastic force constant was converted to an elastic frequency by taking the square root. The relative change of this elastic frequency is plotted as a function of the relative change of the bond length in Fig. A.1.

Most values form one common curve, exceptions being the results from the empirical pseudo-potential method. In contrast to the behaviour of the Einstein vibrational frequencies depicted in Fig. 5.7, the trend of the elastic frequencies is roughly linear.

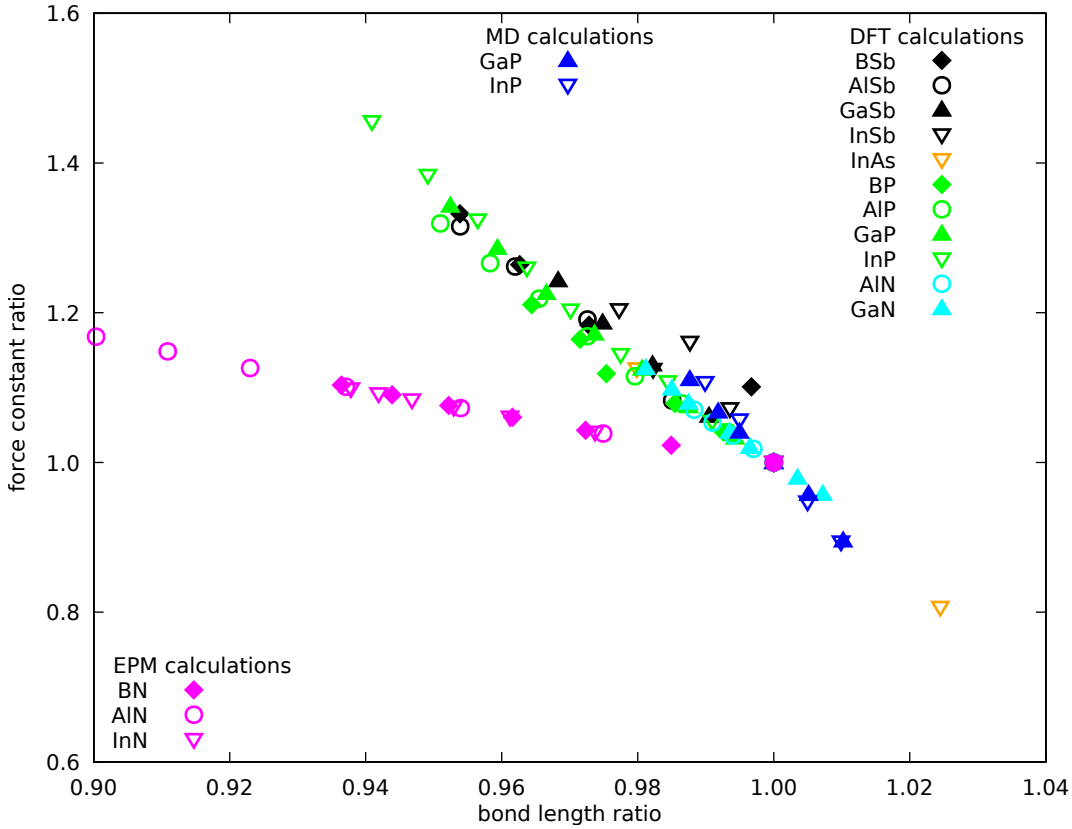

Figure A.1: Ratio of the square root of the elastic force constants as a function of bond-length ratio. The values stemming from density functional theory calculations (Antimonides [66], InAs [62], Phosphides [64], Nitrides [61]) and molecular dynamics calculations (GaP [65], InP [128]) roughly form one common curve for all materials. The values from the empirical pseudo-potential method [67] deviate significantly from this trend.

B Characterisation details

B.1 SEM images of thin films

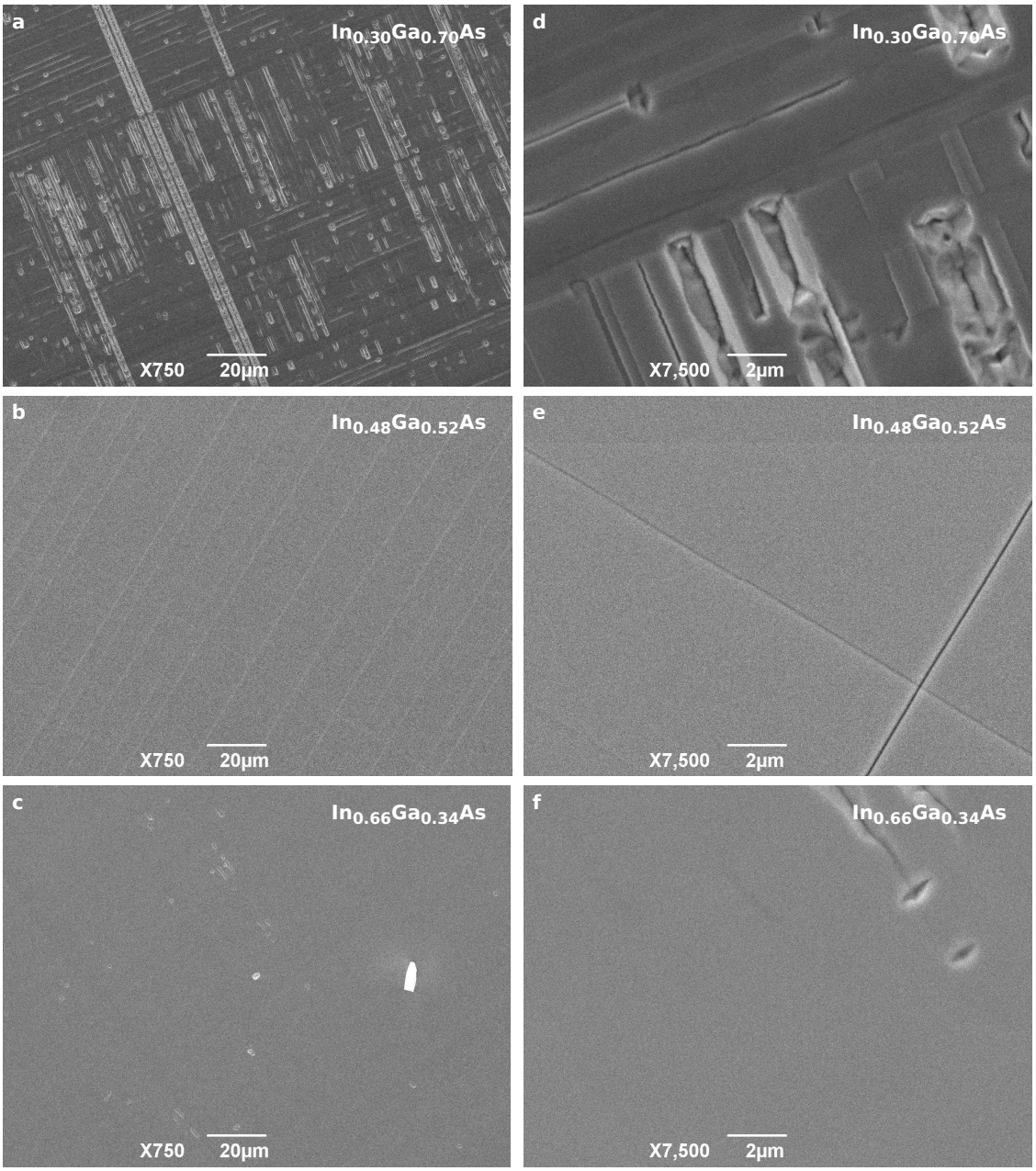

Figure B.1: SEM backscattering electron images of (In,Ga)As thin films. Many defects are visible in the images of $In_{0.30}Ga_{0.70}As$ (panel a and d). In comparison, the images of $In_{0.48}Ga_{0.52}As$ and $In_{0.66}Ga_{0.34}As$ show significantly better crystallinity.

B.2 RBS measurements

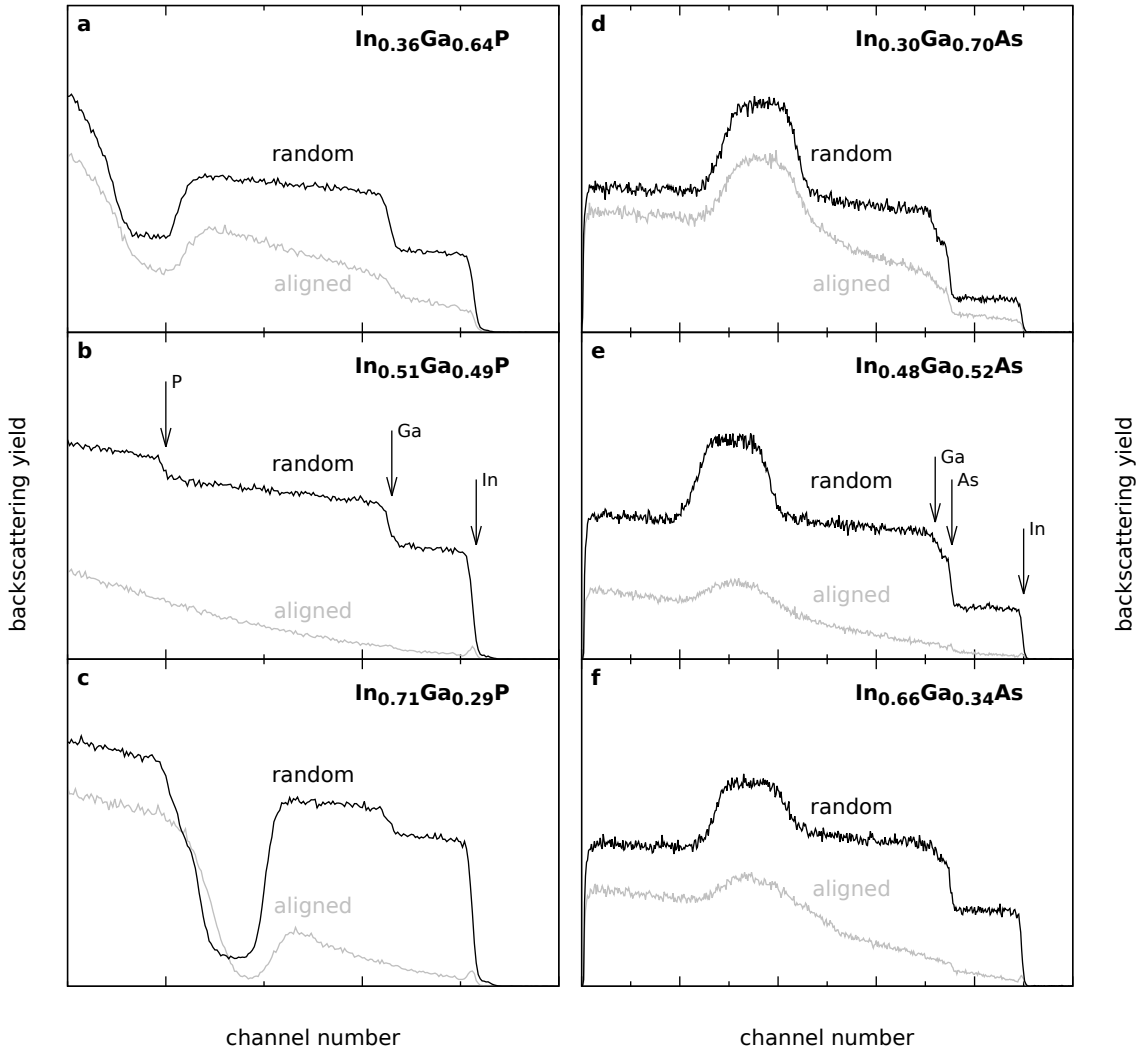

Figure B.2: Comparison between RBS spectra in random and channelling configuration. For a given element of the sample, a smaller channel number (smaller energy of the backscattered ion) correlates with a larger depth, since the backscattered ion loses more energy till it reaches the detector. The reduction of the backscattering yield when orienting a crystallographic axis along the incident beam direction (*aligned*) compared to the yield for an arbitrary direction (*random*) is a measure for the crystalline quality. **a-c,** RBS measurements of the (In,Ga)P thin films confirm the good crystal quality of the samples. The In and Ga surface signals (labelled in panel b) are clearly separable for all three compositions. **d-f,** For (In,Ga)As, all three surface signals are separable. The $In_{0.30}Ga_{0.70}As$ sample shows significantly poorer crystallinity than the other compositions.

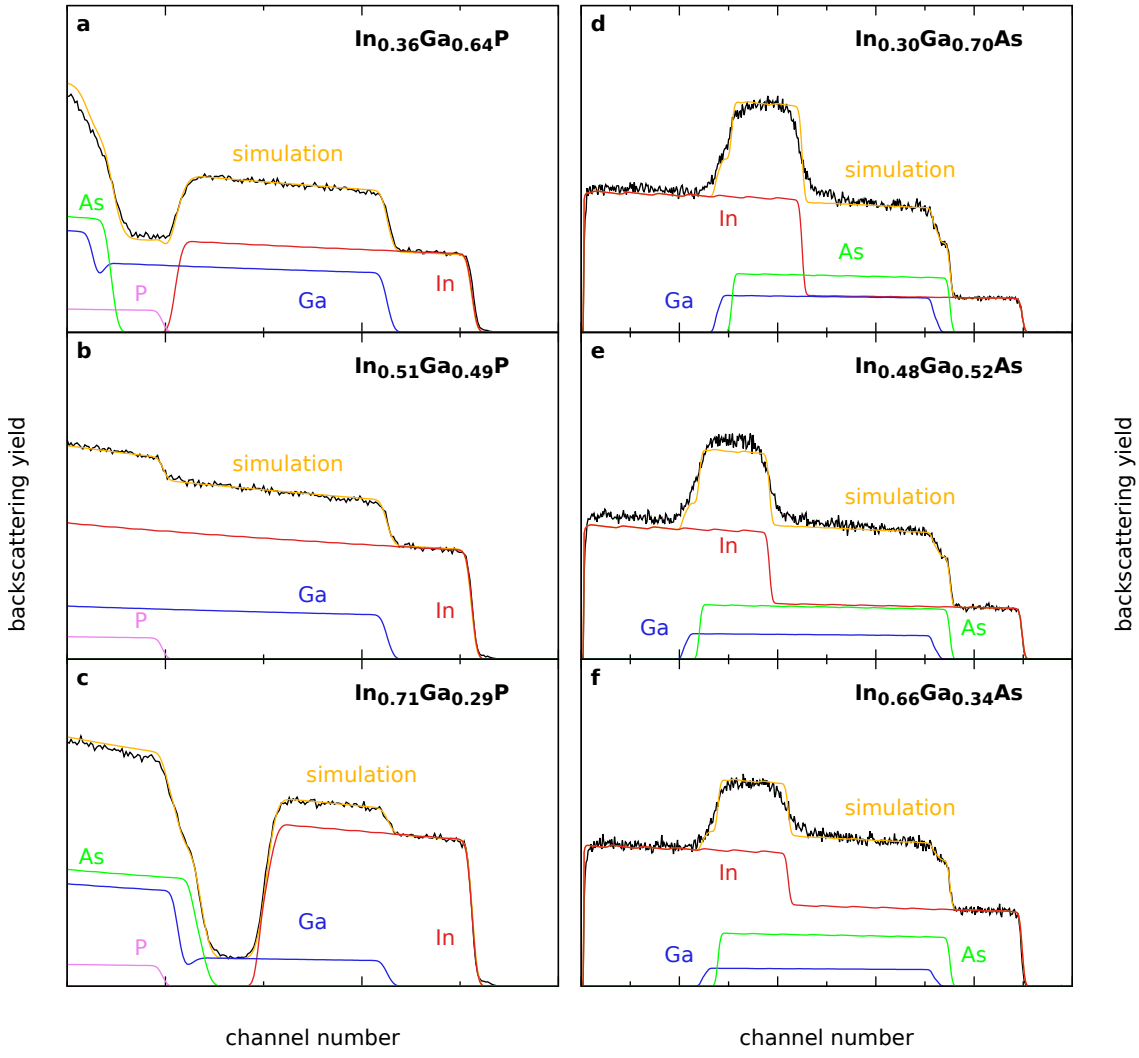

Figure B.3: Fit of RBS spectra in random configuration a-c, The random RBS spectra of (In,Ga)P were fitted using the Rump code [39, 108] to determine the In content In/(In+Ga). The contributions of the individual elements were calculated using the *Spektrenverwaltungsprogramm*, written by Ulrich Barth from the Institute of Solid State Physics in Jena, assuming the compositions determined from Rump. The As contribution visible in panels a and c stems from the AlAs intermediate layer and the GaAs substrate. The small thickness of the films with composition In/(In+Ga) = 0.36 and 0.71 leads to the drop of the backscattering yield corresponding to the position of the AlAs intermediate layer. The P surface signal is clearly visible only in panel b, since it overlays with the drop of the In signal corresponding to the end of the film and the start of the As and Ga signal of the GaAs substrate in panel a and c, respectively. **d-f,** The random RBS spectra of (In,Ga)As were fitted using the *Spektrenverwaltungsprogramm* to determine the In content and III/V ratio. The second increase of the In signal is due to the InP substrate.

B.3 Particle size in the (In,Ga)As EXAFS samples

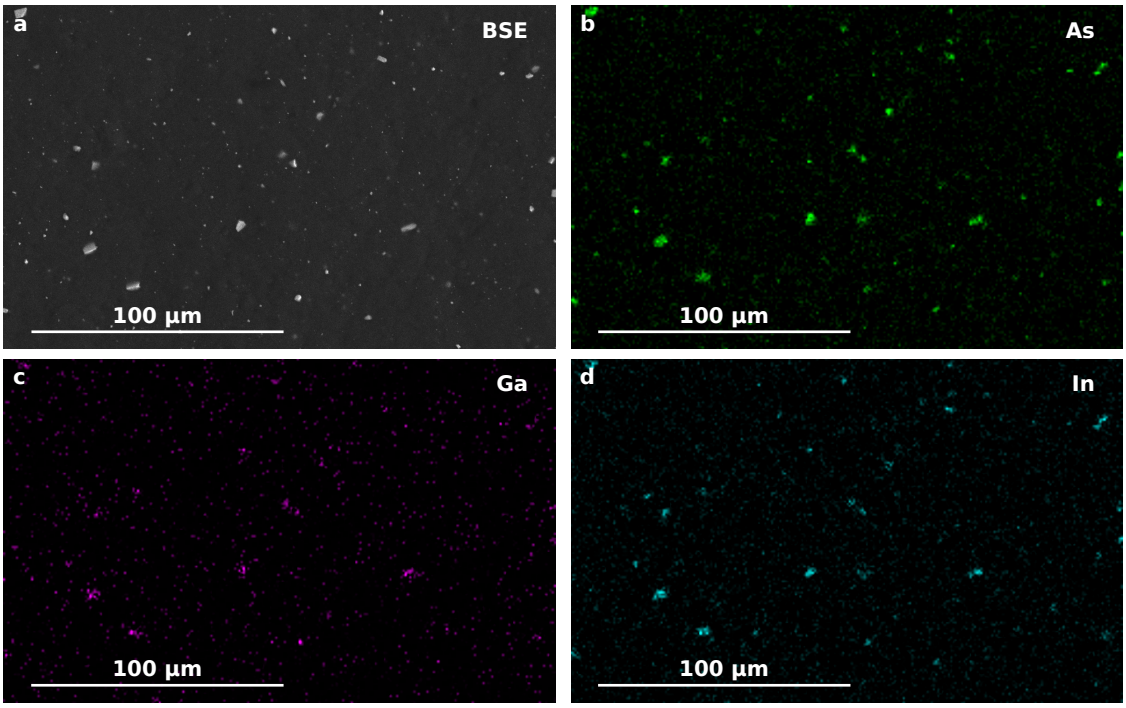

Figure B.4: Particle size in the pressed pellet for the $In_{0.48}Ga_{0.52}As$ sample. a, The (In,Ga)As particles with a size of up to 5 µm are visible as light spots against the dark graphite matrix in the SEM backscattering electron image. **b-d,** The attribution was confirmed by EDX using the As-L, Ga-K and In-L lines.

C Analysis details

C.1 Cumulant formulas used in the path parametrisation

The functions to calculate the temperature dependence of the cumulants are based heavily on the standard LARCH function `sigma2_eins`, but implement the formulas including anharmonic contributions up to the fourth order [47]. How many anharmonic contributions should be used, can be selected by the parameter terms.

```
def C2_anharm(T,k0,k3,k4,terms=6,rmass=None,path=None,_larch=None):
    """calculate anharmonic second cumulant as in Yokoyama99 and Haug08

    Parameters:
    ------------
    t       sample temperature (in K)
    k0, k3,k4 force constants
    path    FeffPath to calculate sigma2 for [None]

    if path is None, the 'current path'
    (_sys.paramGroup._feffdat) is used.

    """
    if rmass is None:
        if path is None:
            try:
                path = _larch.symtable._sys.paramGroup
            except:
                pass
        try:
            rmass = path._feffdat.rmass
        except:
            return 0.00

    if T < 1.e-5: T = 1.e-5

    omega = np.sqrt(k0/(rmass*consts.atomic_mass)) # 1/s
    sig02 = consts.hbar/(2*(rmass*consts.atomic_mass)*omega) #Js/(kg/s) = m2
    beta = 1/(consts.k*T)
    lnz = -beta*consts.hbar*omega
    z = np.exp(lnz)
```

```
    k3=k3*1.e10 #kg/(s^2 AA) -> kg/(s^2 m)
    k4=k4*1.e20 #N/(m * AA^2) -> N/(m^3)

    C20 = sig02*(1+z)/(1-z)
    C21 = -k4*sig02**3/(consts.hbar*omega)*12*(1+z)**2/((1-z)**2) - k4*sig02**3/(consts.
        k*T)*24*z*(1+z)/((1-z)**3)
    C22a = k3**2*sig02**4/((consts.hbar*omega)**2)*4*(13*z**2+58*z+13)/((1-z)**2) + k3
        **2*sig02**4/(consts.hbar*omega*consts.k*T)*120*z*(1+z)/((1-z)**3)
    C22b= k4**2*3*(consts.hbar**3*omega**3)/(8*k0**5)*((5*(1+z)*(7+z*(20+7*z)))/((1-z)
        **3)-(12*z*(8+z*(21+8*z))*lnz)/((1-z)**4)+(12*z*(1+z)*(1+z*(8+z))*lnz**2)/((1-z)
        **5))
    C23a= -k3**2*k4*3*(consts.hbar*omega)**3/(8*k0**6)*(((1+z)*(275+z*(1976+275*z)))
        /((1-z)**3)-(12*z*(71+z*(209+71*z))*lnz)/((1-z)**4)+(60*z*(1+z)*(1+z*(8+z))*lnz
        **2)/((1-z)**5))
    C23b= -k4**3*9*(consts.hbar*omega)**4/(8*k0**7)*((4*(1+z)**2*(37+z*(176+37*z)))/((1-
        z)**4)-(z*(1-z)*(535+z*(2072+535*z))*lnz)/((1-z)**5)+(12*z*(6+z*(93+z*(205+93*z
        +6*z**2)))*lnz**2)/((1-z)**6)-(4*z*(1+z)*(1+z*(38+z*(144+z*(38+z))))*lnz**3)
        /((1-z)**7))
    termlist = [C20,C21,C22a,C22b,C23a,C23b]
    return sum(termlist[0:terms])*1.e20 #m2 -> AA2
#enddef
```

```
def C3_anharm(T,k0,k3,k4,terms=6,rmass=None,path=None,_larch=None):
    """calculate anharmonic third cumulant as in Yokoyama99 and Haug08

    Parameters:
    ------------
    t       sample temperature (in K)
    k0, k3 force constants
    path    FeffPath to calculate C3 for [None]

    if path is None, the 'current path'
    (_sys.paramGroup._feffdat) is used.

    """
    if rmass is None:
        if path is None:
            try:
                path = _larch.symtable._sys.paramGroup
            except:
                pass
        try:
            rmass = path._feffdat.rmass
        except:
            return 0.00

    if T < 1.e-5: T = 1.e-5

    omega = np.sqrt(k0/(rmass*consts.atomic_mass))
    sig02 = consts.hbar/(2*(rmass*consts.atomic_mass)*omega)
    beta = 1/(consts.k*T)
    lnz = -beta*consts.hbar*omega
    z = np.exp(lnz)
```

```
    k3=k3*1.e10 #kg/(s^2 AA) -> kg/(s^2 m)
    k4=k4*1.e20 #N/(m * AA^2) -> N/(m^3)

    C31 = k3*sig02**3/(consts.hbar*omega)*4*(z**2+10*z+1)/((1-z)**2)
    C32 = -k3*k4*3*(consts.hbar*omega)**3/(4*k0**5)*(((1+z)*(17+z*(224+17*z)))/((1-z)
        **3)-(12*z*(2+z*(9+2*z))*lnz)/((1-z)**4))
    C33a= k3**3*3*(consts.hbar*omega)**3/(8*k0**6)*(((1+z)*(41+z*(680+41*z)))/((1-z)**3)
        -(60*z*(2+z*(9+2*z))*lnz)/((1-z)**4))
    C33b= k3*k4**2*(consts.hbar*omega)**4/(16*k0**7)*((4717+z*(92234+z*(215994+z
        *(92234+4717*z))))/((1-z)**4)-(180*z*(1+z)*(68+z*(497+68*z))*lnz)/((1-z)**5)
        +(216*z*(2+z*(49+z*(124+z*(49+2*z))))*lnz**2)/((1-z)**6))
    C34a= -k3**3*k4*3*(consts.hbar*omega)**4/(16*k0**8)*((5483+z*(134182+z*(333174+z
        *(134182+5483*z))))/((1-z)**4)-(36*z*(1+z)*(572+z*(4483+572*z))*lnz)/((1-z)**5)
        +(360*z*(2+z*(49+z*(124+z*(49+2*z))))*lnz**2)/((1-z)**6))
    C34b= -k3*k4**3*3*(consts.hbar*omega)**5/(32*k0**9)*((5*(1+z)*(15035+z*(378526+z
        *(1265526+z*(378526+15035*z)))))/((1-z)**5)-(12*z*(23215+z*(310531+z*(668432+z
        *(310531+23215*z))))*lnz)/((1-z)**6)+(144*z*(1+z)*(97+z*(3564+z*(13435+z
        *(3564+97*z))))*lnz**2)/((1-z)**7)-(144*z*(2+z*(187+z*(1712+z*(3404+z*(1712+z
        *(187+2*z))))))*lnz**3)/((1-z)**8))
    termlist = [C31,C32,C33a,C33b,C34a,C34b]
    return sum(termlist[0:terms])*1.e30 #m3 -> AA3
#enddef
```

```
def C4_anharm(T,k0,k3,k4,terms=4,rmass=None,path=None,_larch=None):
    """calculate anharmonic fourth cumulant as in Yokoyama99 and Haug08

    Parameters:
    ------------
    t       sample temperature (in K)
    k0, k3, k4 force constants
    path    FeffPath to calculate C3 for [None]

    if path is None, the 'current path'
    (_sys.paramGroup._feffdat) is used.

    """
    if rmass is None:
        if path is None:
            try:
                path = _larch.symtable._sys.paramGroup
            except:
                pass
        try:
            rmass = path._feffdat.rmass
        except:
            return 0.00

    if T < 1.e-5: T = 1.e-5

    omega = np.sqrt(k0/(rmass*consts.atomic_mass))
    sig02 = consts.hbar/(2*(rmass*consts.atomic_mass)*omega)
    beta = 1/(consts.k*T)
```

```
    lnz = -beta*consts.hbar*omega
    z = np.exp(lnz)

    k3=k3*1.e10 #kg/(s^2 AA) -> kg/(s^2 m)
    k4=k4*1.e20 #N/(m * AA^2) -> N/(m^3)

    C41 = -k4*sig02**4/(consts.hbar*omega)*12*(z**3+9*z**2+9*z+1)/((1-z)**3) - k4*sig02
        **4/(consts.k*T)*144*z**2/((1-z)**4)
    C42 = k3**2*sig02**5/(consts.hbar**2*omega**2)*12*(5*z**3+109*z**2+109*z+5)/((1-z)
        **3) + k3**2*sig02**5/(consts.hbar*omega*consts.k*T)*720*z**2/((1-z)**4)
    C43a= -k3**2*k4*9*(consts.hbar*omega)**4/(16*k0**7)*((237+z*(5930+z*(15482+z
        *(5930+237*z))))/((1-z)**4)-(4*z*(1+z)*(92+z*(1613+92*z))*lnz**2)/((1-z)**5)
        +(120*z**2*(5+z*(16+5*z))*lnz**2)/((1-z)**6))
    C43b= -k4**3*3*(consts.hbar*omega)**5/(32*k0**8)*(((1+z)*(3707+z*(59310+z*(133046+z
        *(59310+3707*z)))))/((1-z)**5)-(12*z*(861+z*(13803+z*(29524+3*z*(4601+287*z))))*
        lnz)/((1-z)**6)+(432*z*(1+z)*(1+z*(82+z*(371+z*(82+z))))*lnz**2)/((1-z)**7)
        -(144*z**2*(19+z*(230+z*(492+z*(230+19*z))))*lnz**3)/((1-z)**8))
    termlist=[C41,C42,C43a,C43b]
    return sum(termlist[0:terms])*1.e40 #m4 ->AA4
#enddef
```

C.2 Measurement details

Table C.1: Measurement details for (In,Ga)P at the Ga-K edge (top) and the In-K edge (bottom). In the third region the energy step was increased successively to obtain measurement points distributed uniformly in wave-vector space.

start energy [eV]	end energy [eV]	energy step [eV]	integration time [s]
10117	10337	10	1
10337	10407	0.2	1
10407	11467	0.5-2.6	1-5

start energy [eV]	end energy [eV]	energy step [eV]	integration time [s]
27609	27910	2	1
27910	27980	0.5	1
27980	29040	0.5-2.6	1-5

Table C.2: Measurement details for (In,Ga)As at the Ga-K edge (top) and the In-K edge (bottom).

start energy [eV]	end energy [eV]	energy step [eV]	integration time [s]
10267	10337	5	1
10338	10417	0.5	1
10418	10467	1	2
10468	10667	2	4
10668	10867	3	10
10868	11067	4	15
11068	11267	5	20

start energy [eV]	end energy [eV]	energy step [eV]	integration time [s]
27740	27910	10	1
27911	27990	1	1
27991	28040	1	4
28041	28240	2	10
28241	28440	3	15
28441	28640	4	20
28641	28840	5	25
28841	28940	7	30

C.3 Selected spectra

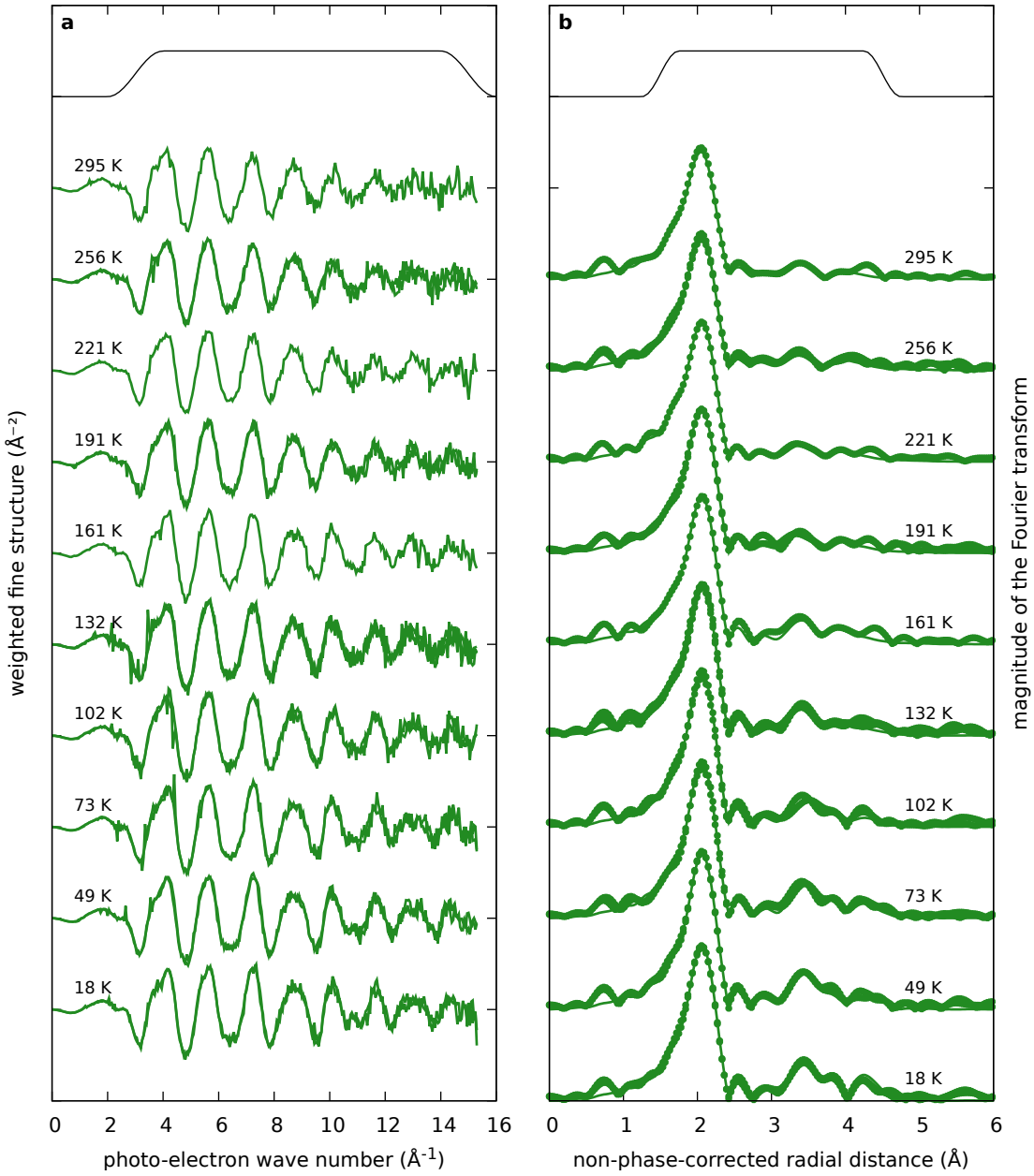

Figure C.1: In-edge spectra of $In_{0.51}Ga_{0.49}P$. Multiple spectra were recorded at selected temperatures. **a,** The fine-structure was weighted with the squared photo-electron wave number to enhance the visibility of the features. The window function used for the subsequent Fourier transformation is shown at the top of the panel. **b,** The magnitude of the Fourier transform resulting from the spectra in panel a (symbols) are compared to the fit of the temperature series using the correlated Einstein model (lines). The fitting range is indicated at the top of the panel.

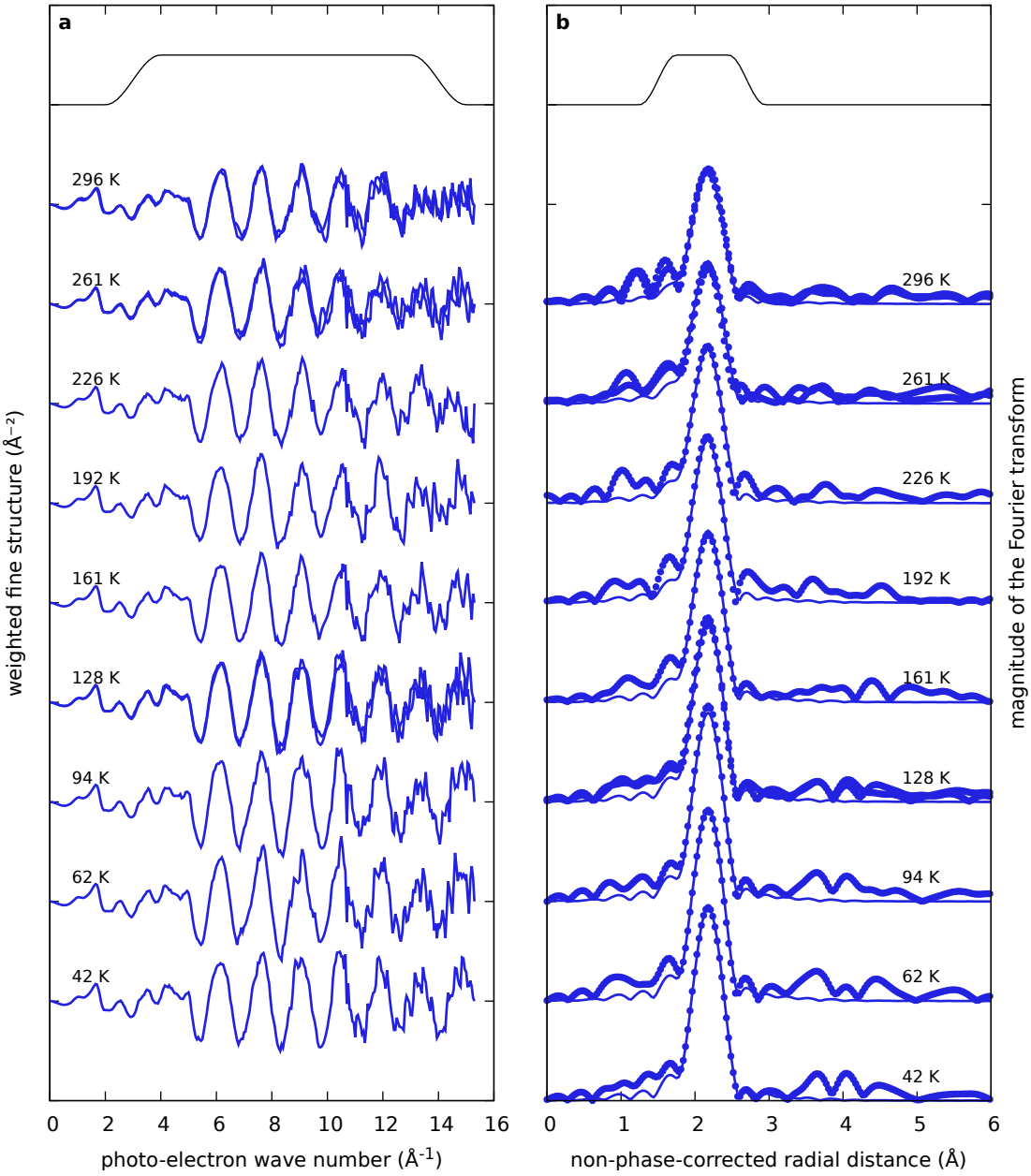

Figure C.2: Ga-edge spectra of $In_{0.48}Ga_{0.52}As$. The description is the same as in Fig. C.1.

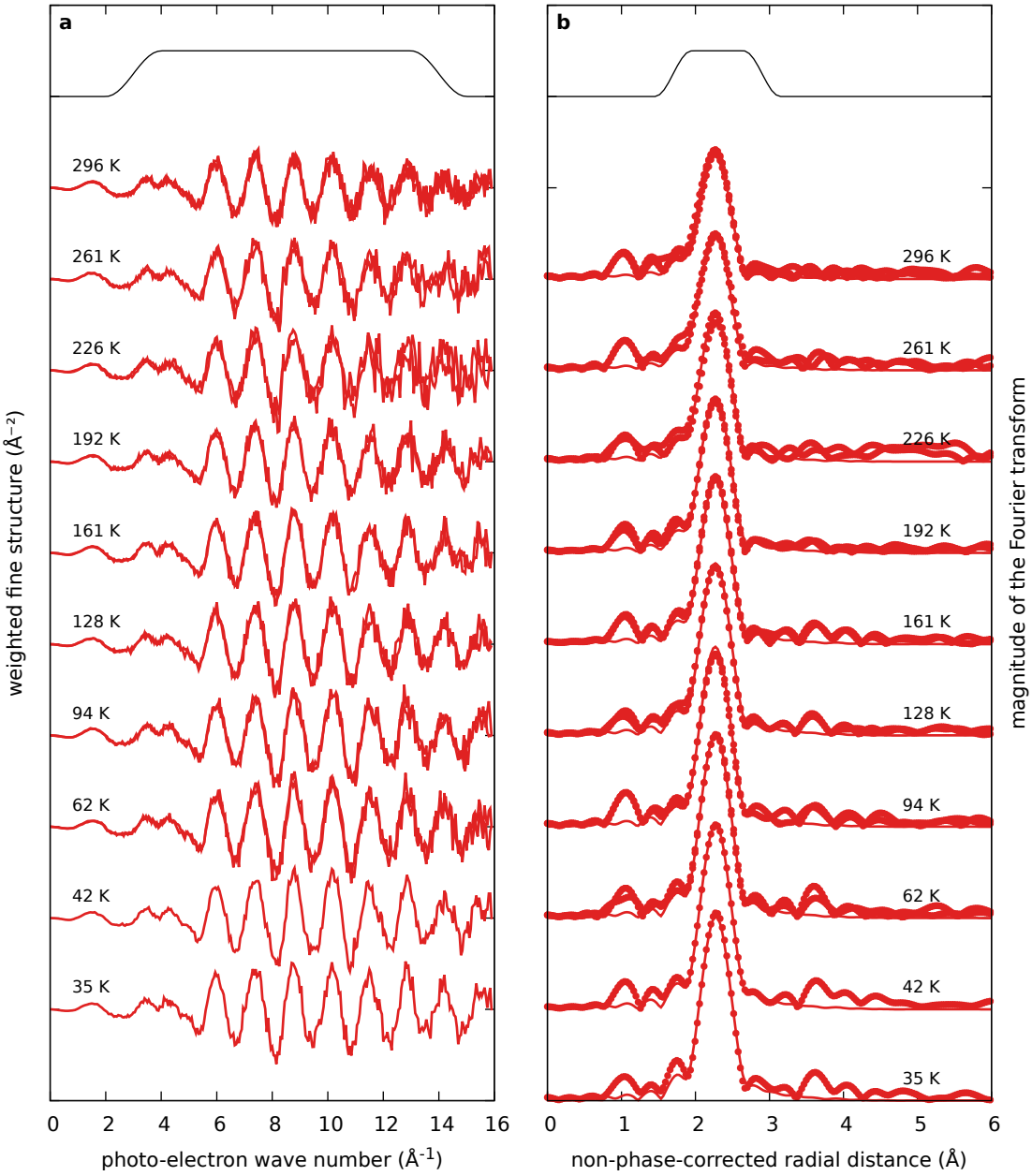

Figure C.3: In-edge spectra of $In_{0.48}Ga_{0.52}As$. The description is the same as in Fig. C.1.

C.4 Test results for ternary alloys

To assess the stability of the fits and to determine the uncertainties for the parameters of interest, the results of the individual fits where plotted as a function of the fit quality parameter R. For the bond-stretching force constants, these plots are shown in chapter 5 as Fig. 5.2 and Fig. 5.4. The plots for several additional parameters are presented here.

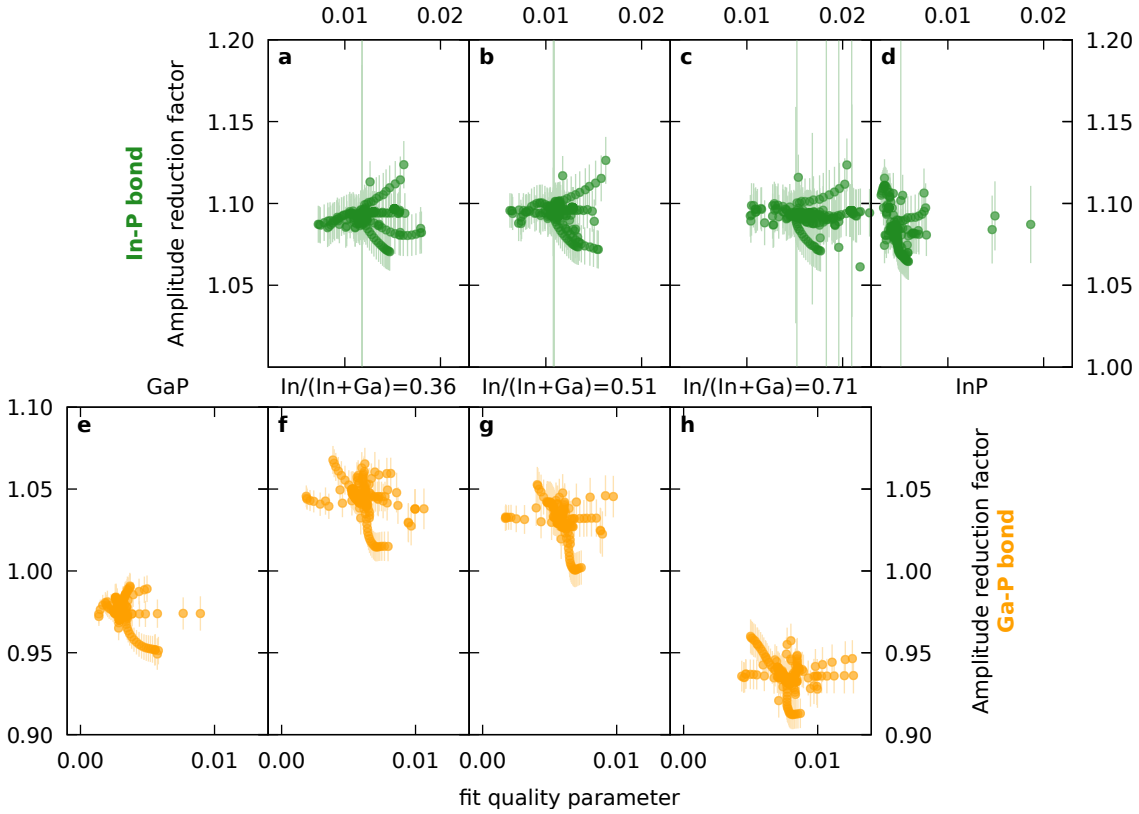

Figure C.4: Amplitude reduction factors in (In,Ga)P. The amplitude reduction factors stemming from individual fits from the same set of tests as in Fig. 5.2 is plotted as a function of the fit quality parameter R. Fits where the amplitude reduction factor was fixed are not shown. While the amplitude reduction factor in its strict theoretical meaning is restricted to values below one, experimental effects can lead to fitted values above one. Differences visible for the Ga edge data are probably caused by differences of the sample properties like the effective thickness or the size distribution of particles. Setting the amplitude reduction factor fixed at the average value of all samples does alter the bond-stretching force constant only within the uncertainties given in Tab. 5.2.

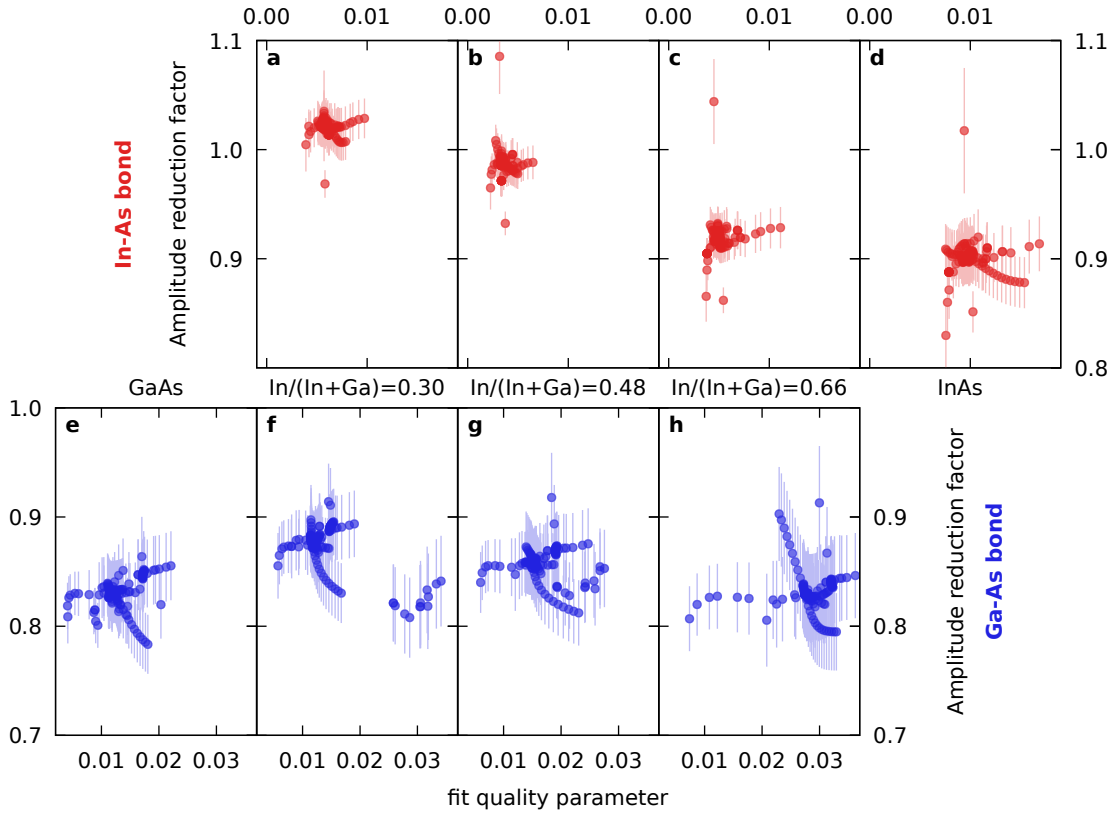

Figure C.5: Amplitude reduction factors in (In,Ga)As. The amplitude reduction factors stemming from individual fits from the same set of tests as in Fig. 5.4 is plotted as a function of the fit quality parameter R. Fits where the amplitude reduction factor was fixed are not shown.

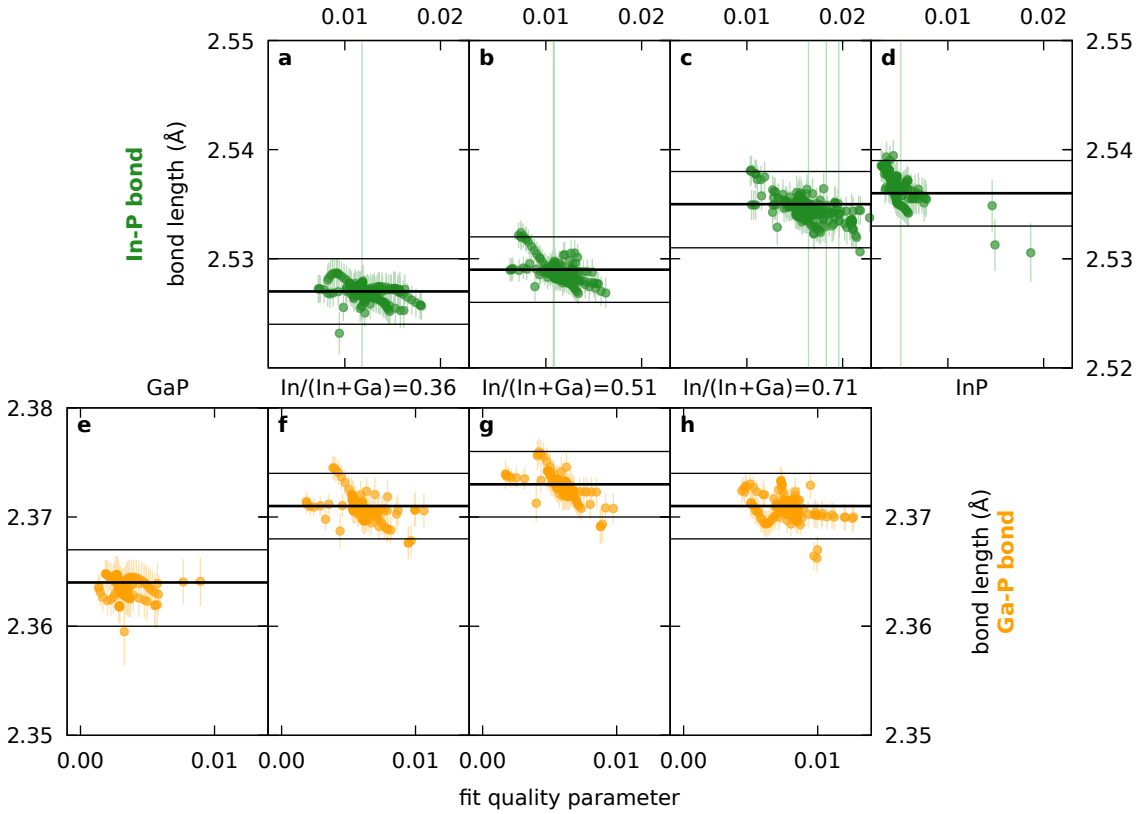

Figure C.6: Bond lengths in (In,Ga)P at 18 K**.** The mean of the 1NN distance distribution (bond length) stemming from the same set of tests as in Fig. 5.2 is plotted as a function of the fit quality parameter R. The temperature of 18 K was chosen for this plot to achieve maximum comparability with the values at 20 K given by Schnohr et al. [31]. As in Fig. 5.2, the thick lines mark one particular fit that gave good results for all samples at one absorption edge, while the thin lines depict the minimum and maximum reasonable values estimated from the whole set. The values determined here, are compared to the literature [31] in Fig. 5.5a.

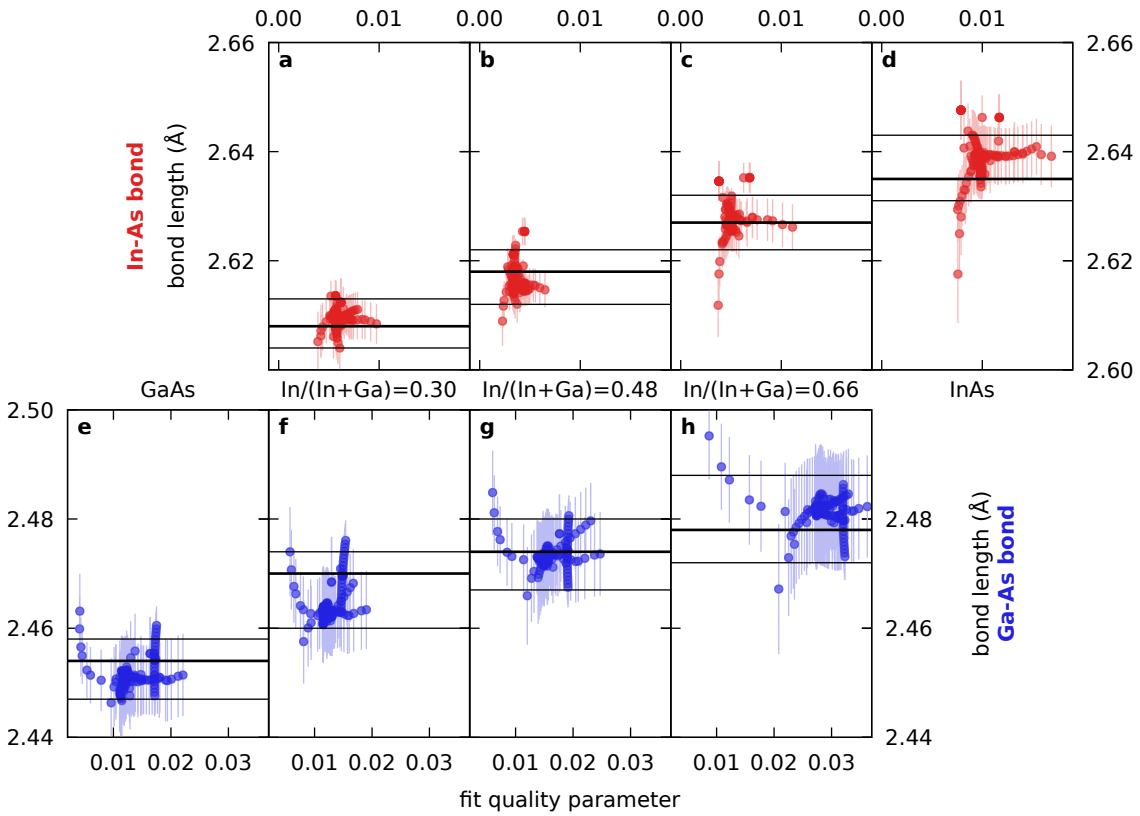

Figure C.7: Bond lengths in (In,Ga)As at 62 K**.** The mean of the 1NN distance distribution (bond length) stemming from the same set of tests as in Fig. 5.4 is plotted as a function of the fit quality parameter R. The temperature of 62 K was chosen for this plot to achieve maximum comparability with the values at 77 K given by Mikkelsen and Boyce [25]. As in Fig. 5.4, the thick lines mark one particular fit that gave good results for all samples at one absorption edge, while the thin lines depict the minimum and maximum reasonable values estimated from the whole set. The values determined here, are compared to the literature [25] in Fig. 5.5b.

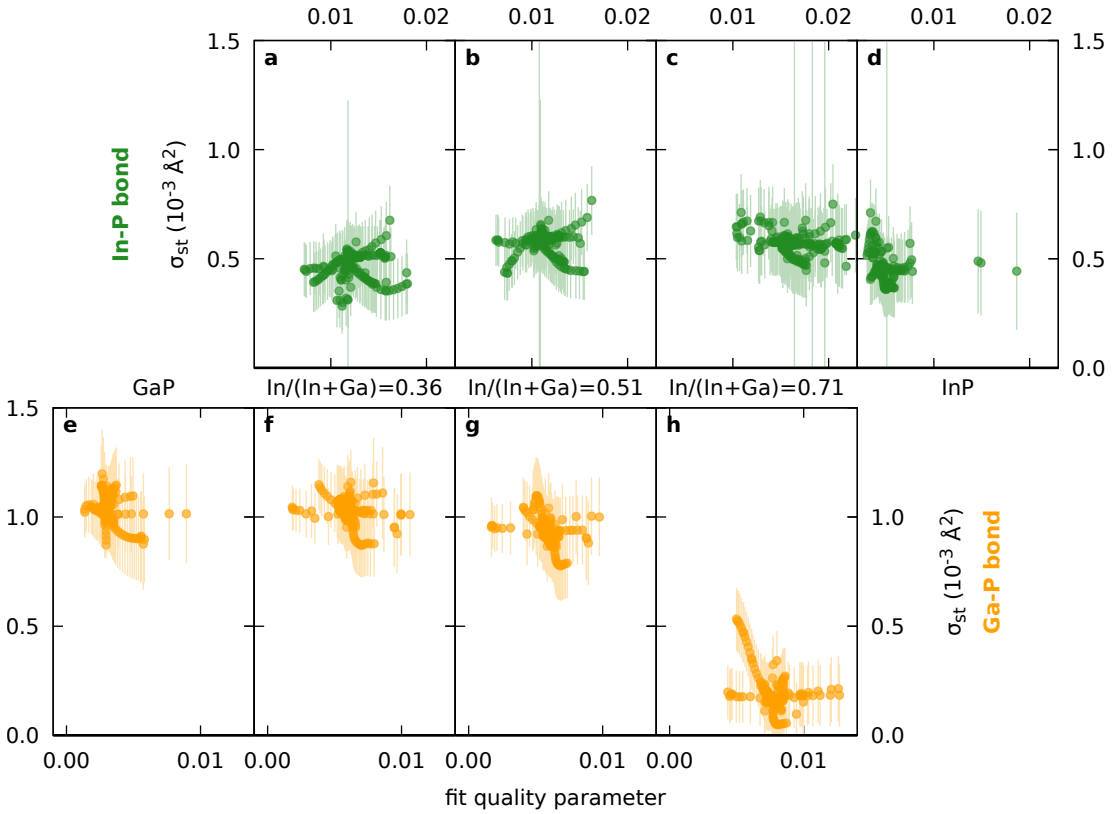

Figure C.8: Static contributions to the variance (σ^2_{st}) in (In,Ga)P. The static contribution to the variance of the 1NN distance distribution is plotted as a function of R factor. The fits shown comprise the same set of tests as in Fig. 5.2 without fitting scenarios where σ^2_{st} was fixed. For GaP the relatively high σ^2_{st} was confirmed by fits including all higher anharmonic contributions given in the literature [47].

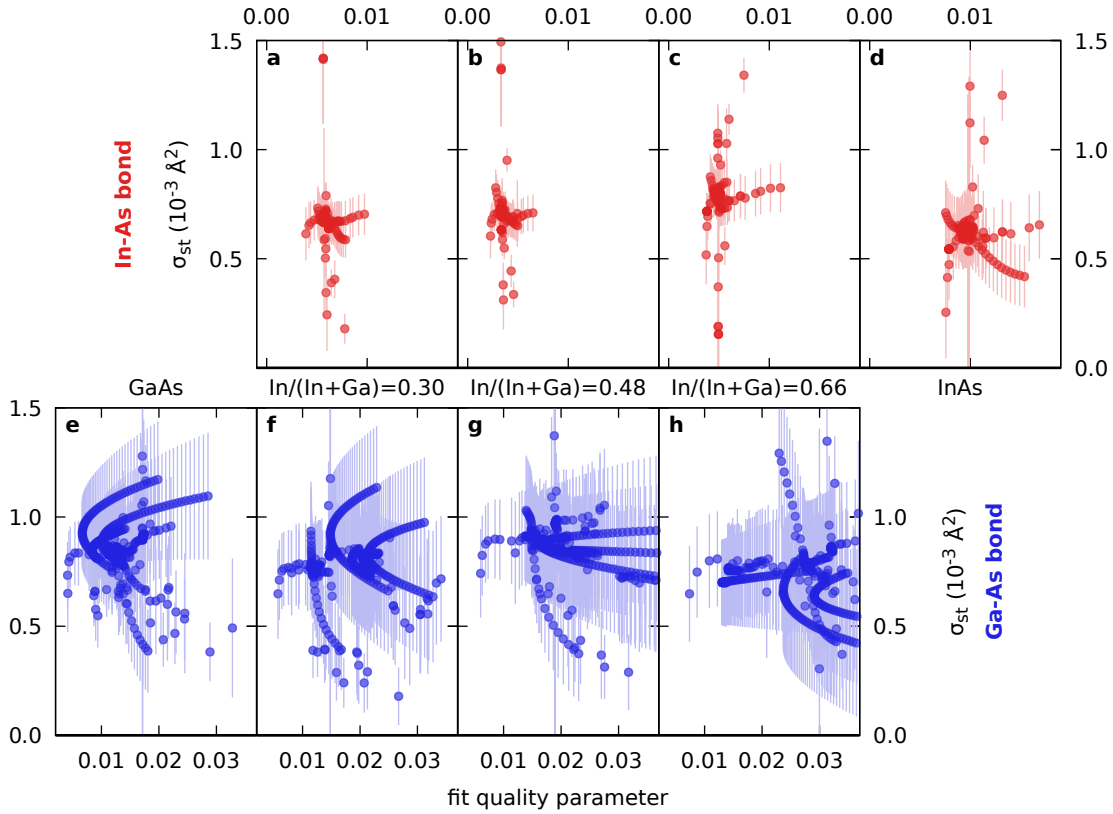

Figure C.9: Static contributions to the variance (σ^2_{st}) in (In,Ga)As. The static contribution to the variance of the 1NN distance distribution is plotted as a function of R factor. The fits shown comprise the same set of tests as in Fig. 5.4 without fitting scenarios where σ^2_{st} was fixed.

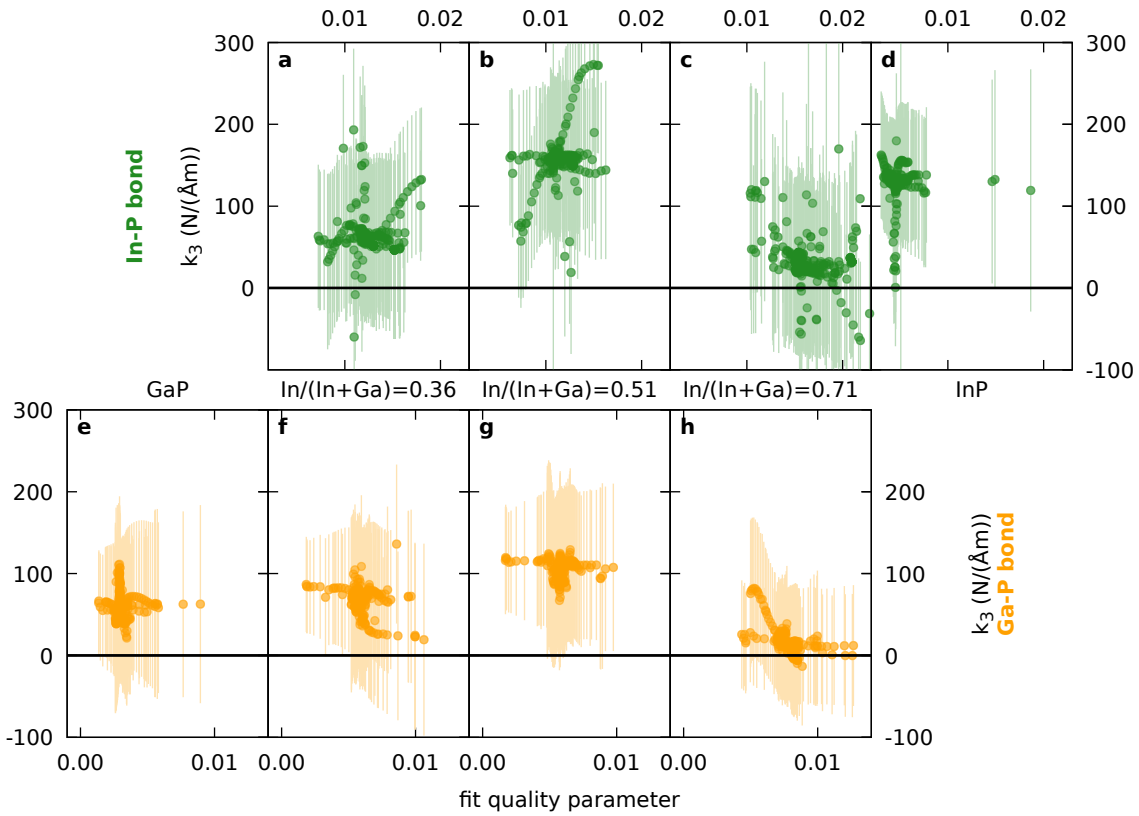

Figure C.10: Cubic force constants in (In,Ga)P. The cubic force constants determined in the same set of fits as in Fig. 5.2 are plotted as a function of the fit quality parameter. Only positive values are physically reasonable. There is no clear trend with composition for neither the Ga edge data nor the In edge data.

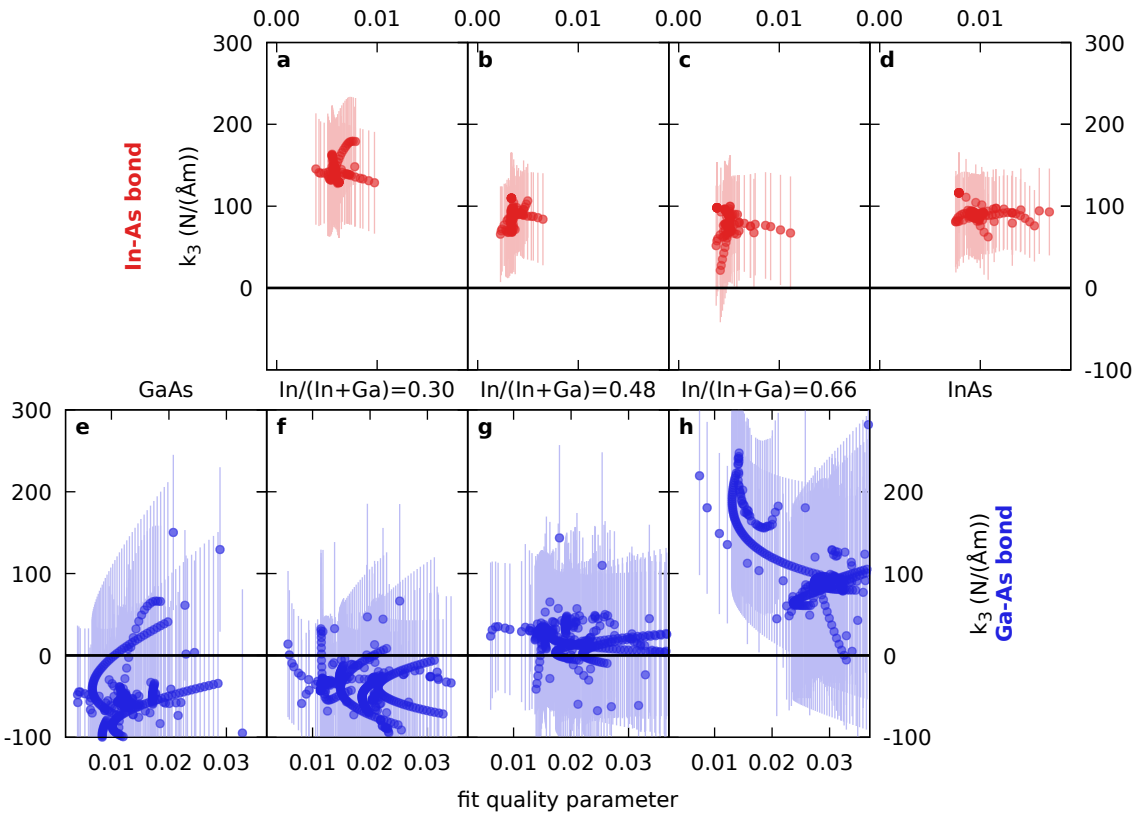

Figure C.11: Cubic force constants in (In,Ga)As. The cubic force constants determined in the same set of fits as in Fig. 5.4 are plotted as a function of the fit quality parameter. Only positive values are physically reasonable. For the In–As bond, there might be a slight decrease of the cubic force constant with increasing In content. The values of the Ga–As bond often lie below zero and feature large uncertainties, probably because the data quality is insufficient for a meaningful determination of the asymmetry parameter.

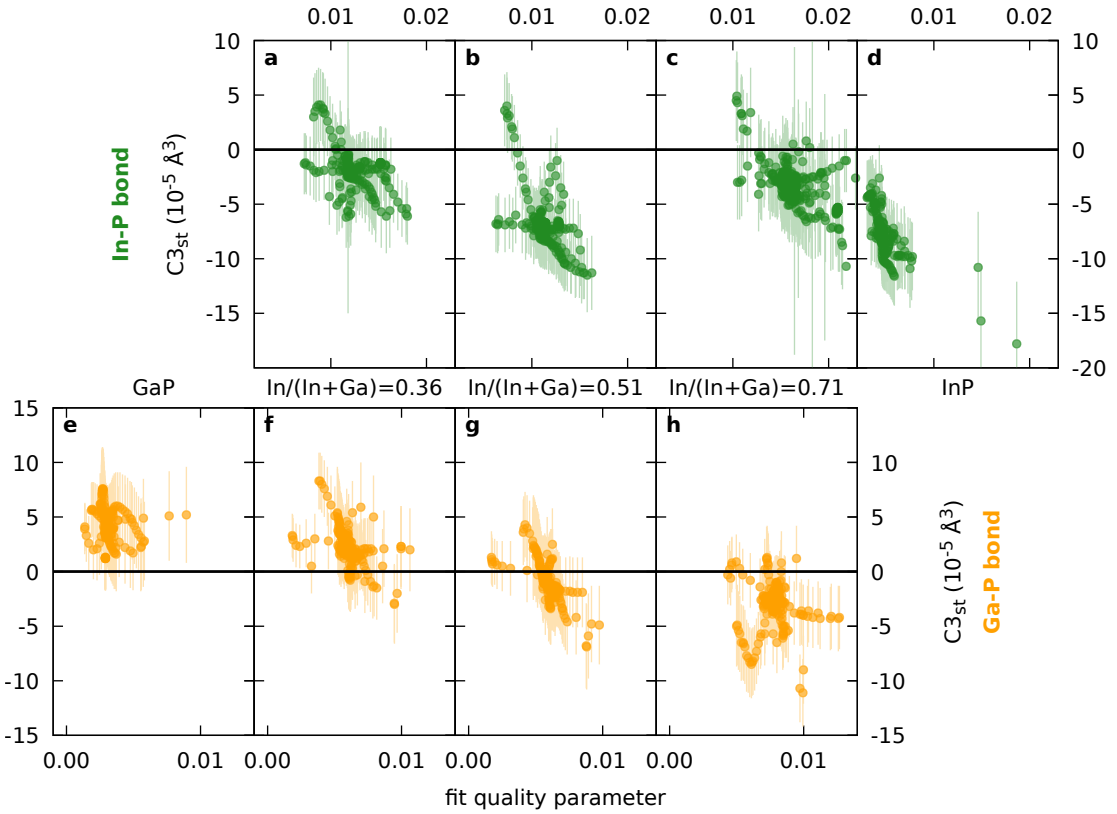

Figure C.12: Static contribution to the third cumulant in (In,Ga)P. The static contribution to the third cumulant C_3 is plotted as a function of the fit quality parameter. The values are from the same set of fits as in Fig. 5.2 but without fit settings where the static contribution to C_3 was fixed at 0. For the Ga–P bond the values suggest a decrease with increasing In content, while no trend is visible for the In–P bond.

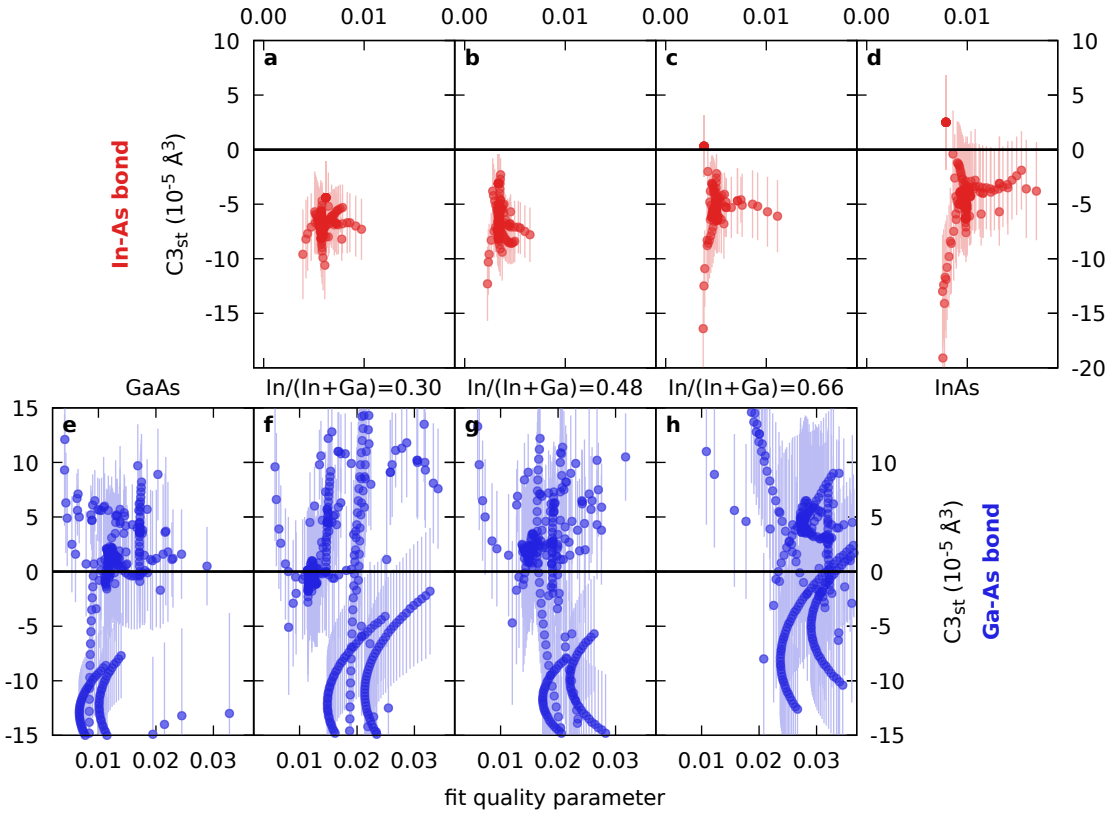

Figure C.13: Static contribution to the third cumulant in (In,Ga)As. The static contribution to the third cumulant C_3 is plotted as a function of the fit quality parameter. The values are from the same set of fits as in Fig. 5.4 but without fit settings where the static contribution to C_3 was fixed at 0. The values at for the In–As bond slightly increase with increasing In content. For the Ga–As bond no conclusion is possible, probably due to insufficient data quality (see also Fig. C.4).

C.5 Test results for binary compounds

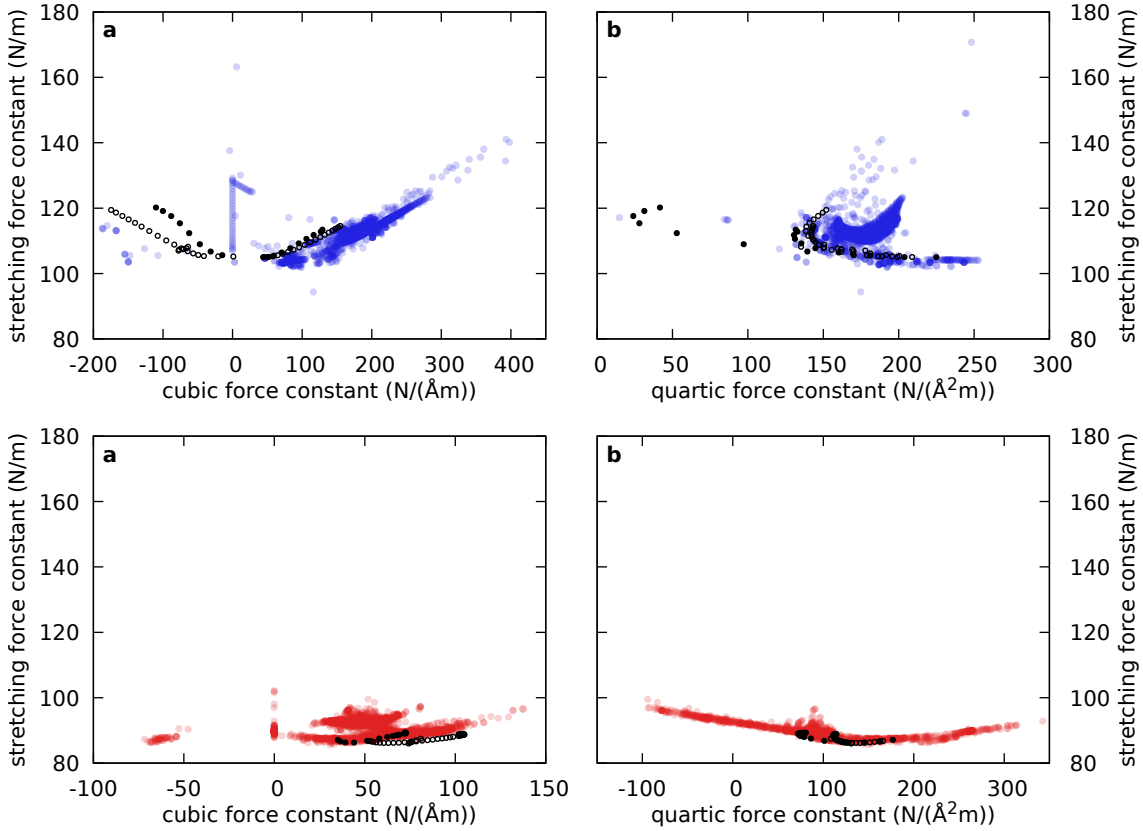

Figure C.14: Correlations between parameters of the effective pair potential for GaAs and InAs measured at SLS. Coloured symbols depict results from the *two-fits* approach, employed for most of the analysis. The results from *all-in-one* fits using literature thermal expansion data (open black symbols) or calculated temperature-dependent bond lengths (solid black symbols) are shown for comparison. The errorbars were omitted for clarity. Negative k_3 are not physically reasonable. For $InAs_{SLS}$ the variation of the bond-stretching force constant is very small, despite the large variation of the quartic force constant. In comparison to this, the larger variation of the bond-stretching force constant in $GaAs_{SLS}$ correlate with a significantly larger variation of the cubic force constant (mind the different scale).

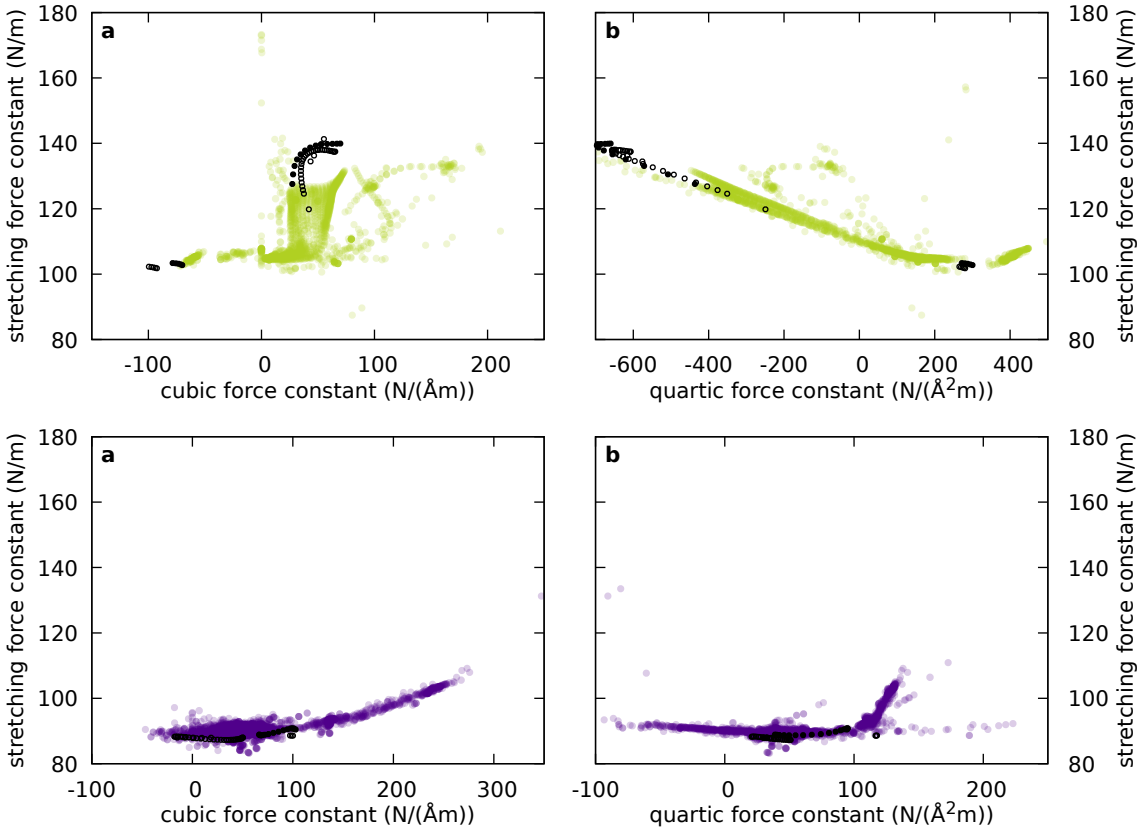

Figure C.15: Correlations between parameters of the effective pair potential for GaSb measured at AS and InSb measured at SLS. Coloured symbols depict results from the *two-fits* approach, employed for most of the analysis. The results from *all-in-one* fits using literature thermal expansion data (open black symbols) or calculated temperature-dependent bond lengths (solid black symbols) are shown for comparison. The errorbars were omitted for clarity. Negative k_3 are not physically reasonable. The variation in the quartic force constant of $GaSb_{AS2}$ is huge. The resulting large variation of the bond-stretching force constant is caused mainly by the considerable increase of the bond-stretching force constant for negative quartic force constants. In contrast, the bond-stretching force constant in $InSb_{SLS}$ varies only moderately and the highest values correlate with large cubic force constants.

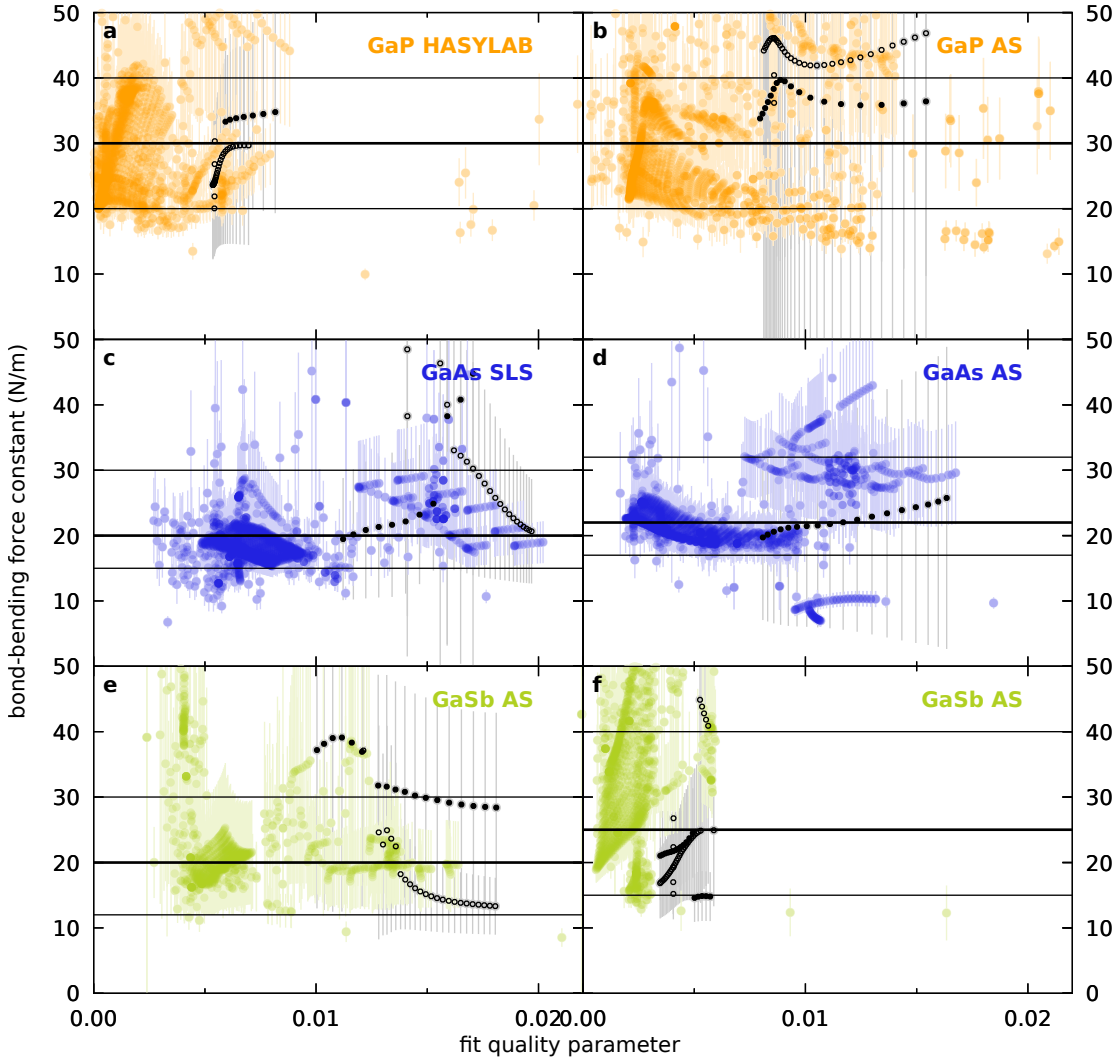

Figure C.16: Uncertainties of the bond-bending force constants in GaP, GaAs and GaSb. The effective bond-bending force constants determined in the same set of fits as in Fig. 6.1 are plotted as a function of the fit quality parameter R from the LARCH fit of the spectra. Coloured symbols depict results from the *two-fits* approach, employed for most of the analysis. The results from *all-in-one* fits using literature thermal expansion data (open black symbols) or calculated temperature-dependent bond lengths (solid black symbols) are shown for comparison. Thick and thin black lines refer to the best, minimum and maximum force constant values given in Tab. 6.2.

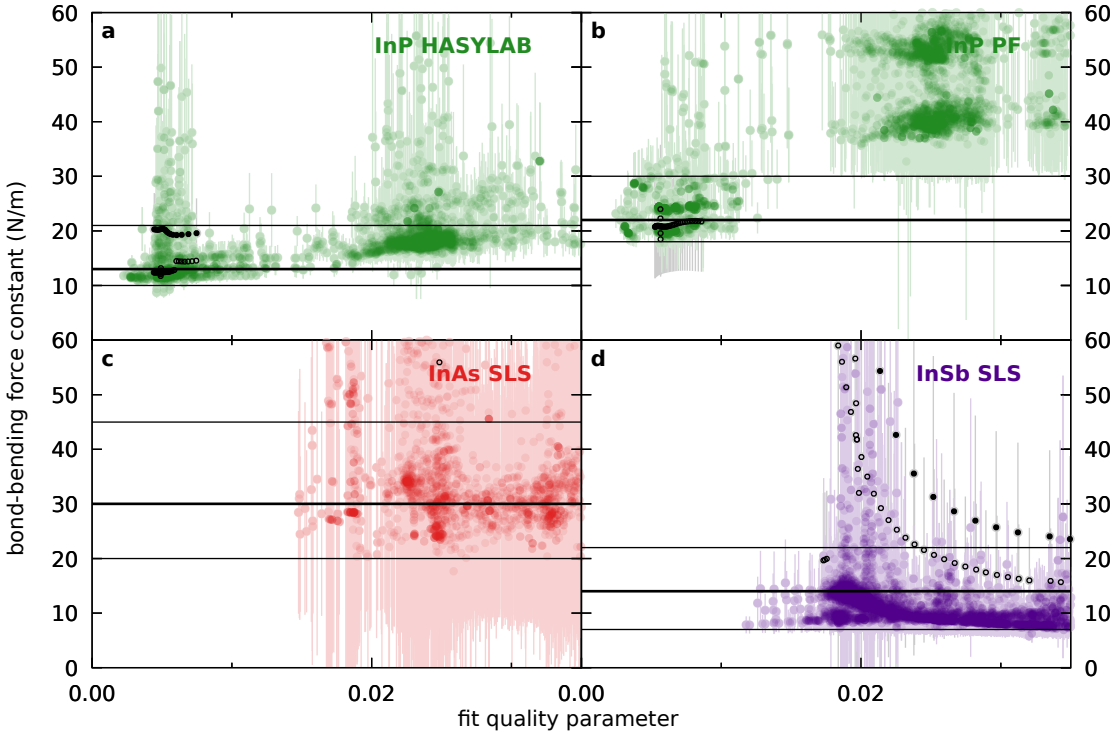

Figure C.17: Uncertainties of the bond-bending force constants in InP, InAs and InSb. The effective bond-bending force constants determined in the same set of fits as in Fig. 6.2 are plotted as a function of the fit quality parameter R from the LARCH fit of the spectra. The description is the same as in Fig. C.16.

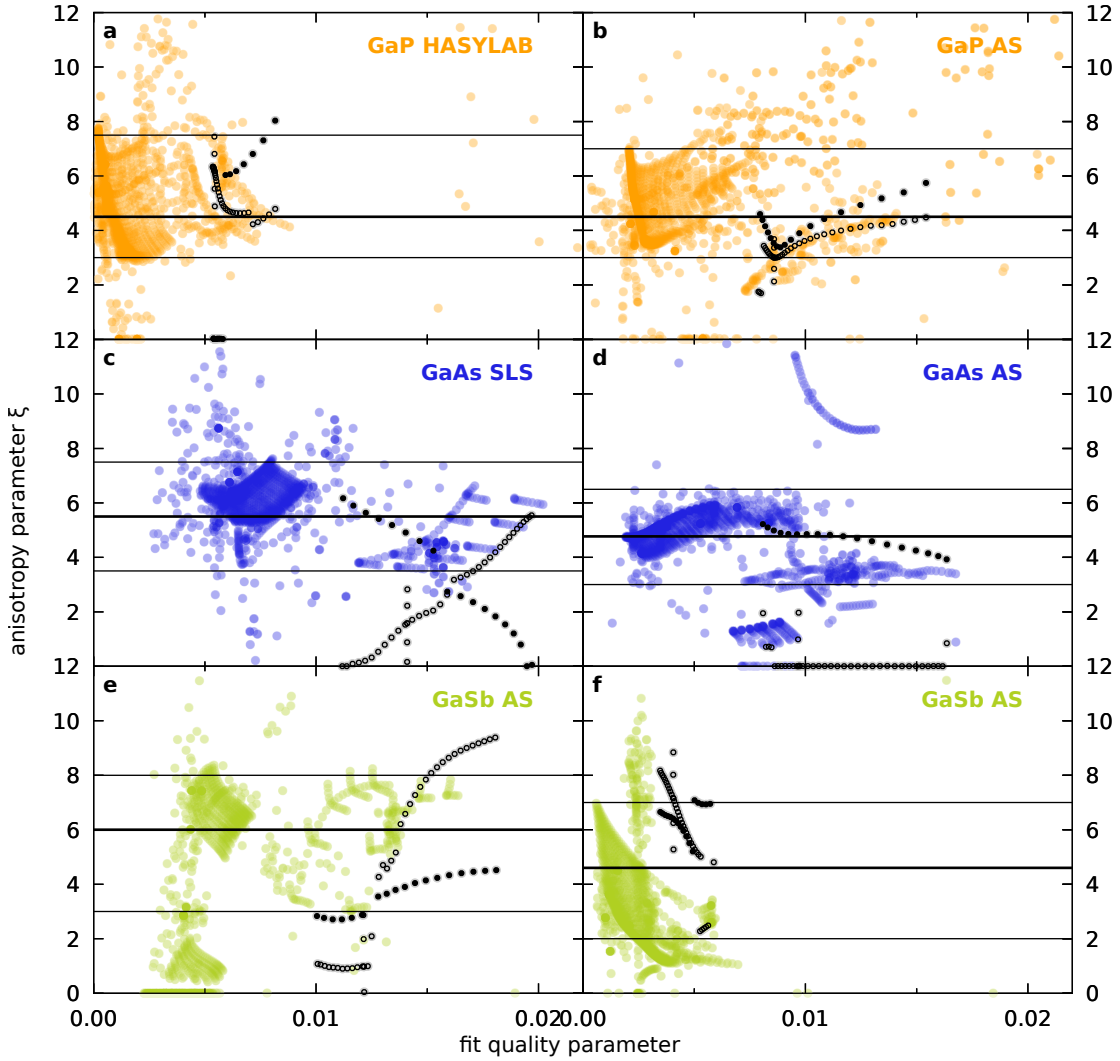

Figure C.18: Anisotropy parameter in GaP, GaAs and GaSb. For each individual fit the anisotropy parameter $\xi = k_{\parallel}/k_{\perp}$ was calculated. These values are plotted as a function of R factor from the first fit (LARCH spectra fit). The symbol description is the same as in Fig. C.16. The errorbars were omitted for clarity. Thick and thin black lines mark the best value and uncertainties which are plotted in Fig. 6.9.

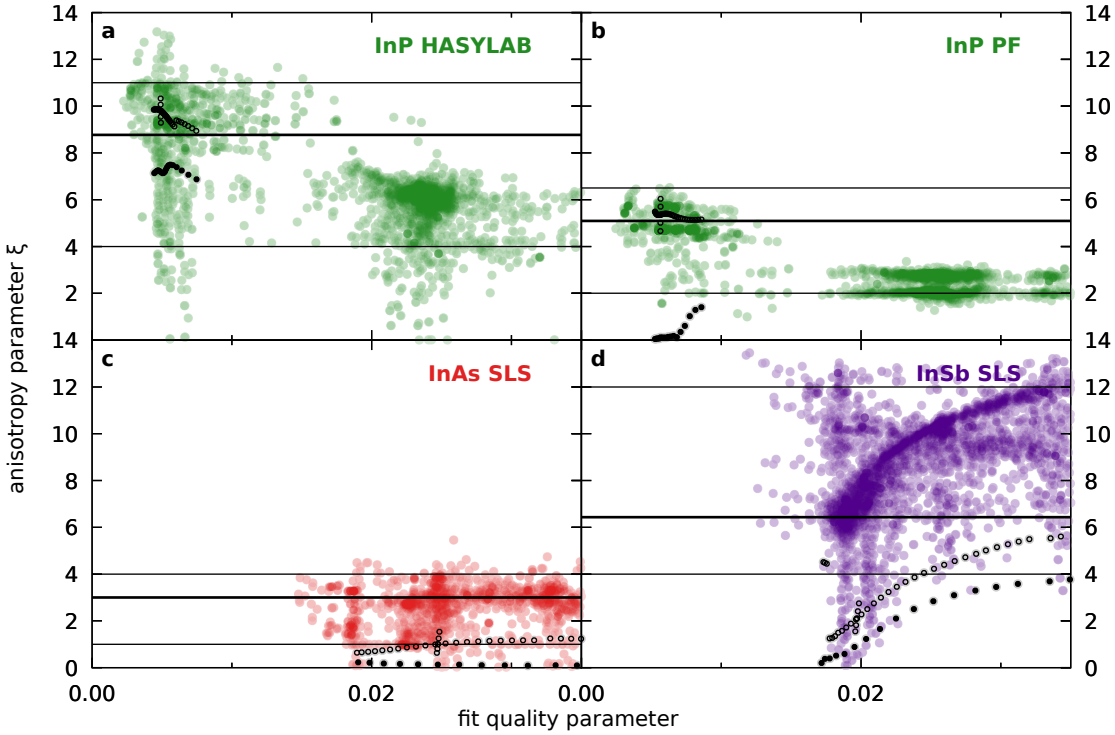

Figure C.19: Anisotropy parameter in InP, InAs and InSb. The anisotropy parameter $\xi = k_{\parallel}/k_{\perp}$ determined for each individual fit is plotted as a function of R factor from the first fit (LARCH spectra fit). The symbol description is the same as in Fig. C.16. The errorbars were omitted for clarity. Thick and thin black lines mark the best value and uncertainties which are plotted in Fig. 6.9.

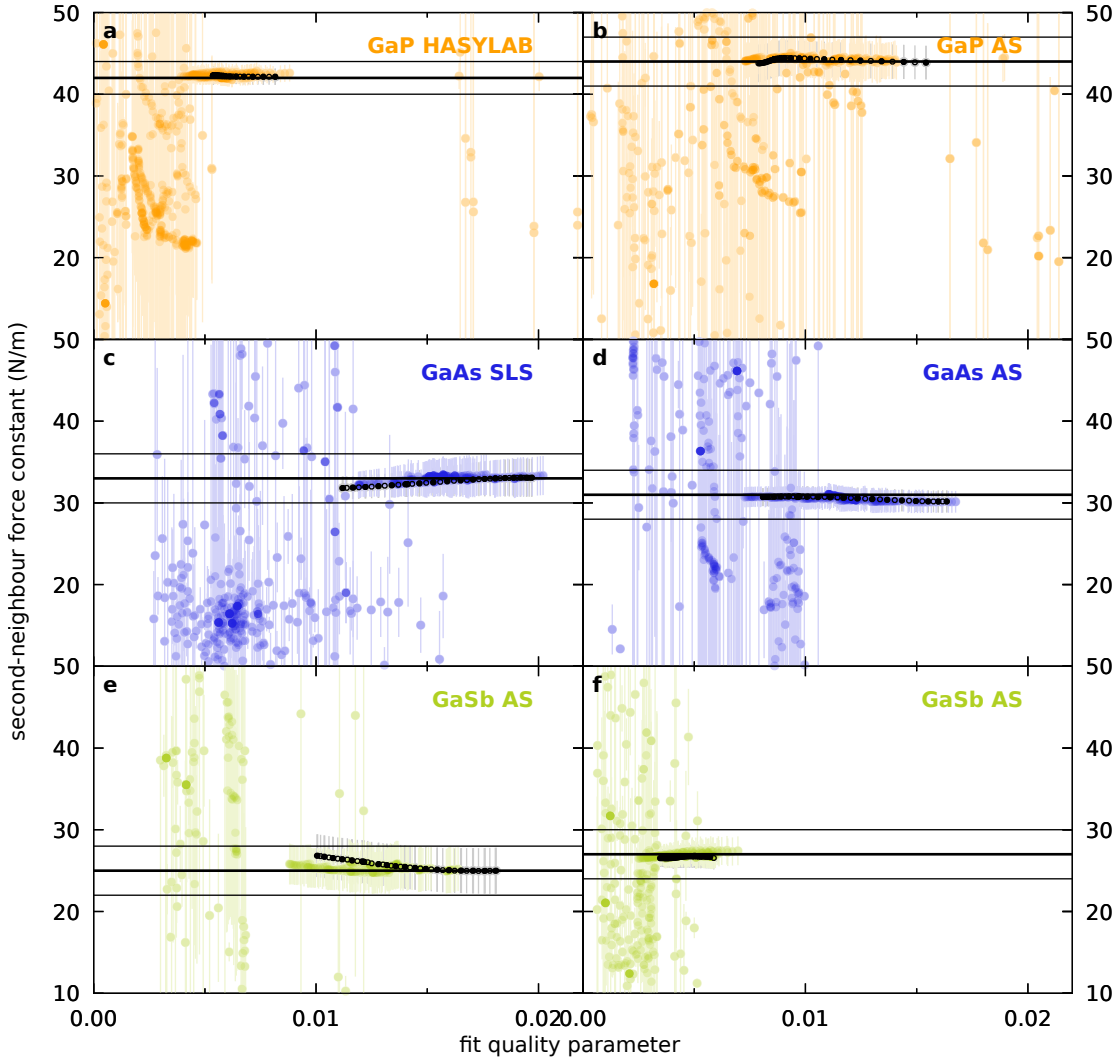

Figure C.20: Uncertainties of the 2NN stretching force constants in GaP, GaAs and GaSb. The effective second-neighbour stretching force constants are plotted as a function of the fit quality parameter R. The set comprises less fits than in Fig. 6.1, since in part of the analysis only the first scattering path was used. The symbol description is the same as in Fig. C.16. Thick and thin black lines refer to the best, minimum and maximum force constant values given in Tab. 6.2. Vastly varying values with huge uncertainties stem from fits were the fitting window did not contain sufficient second shell information for the determination of a meaningful 2NN stretching force constant. These fits mostly show smaller R factors than fits with larger fitting windows, since the R factor is directly dependent on the fitting range.

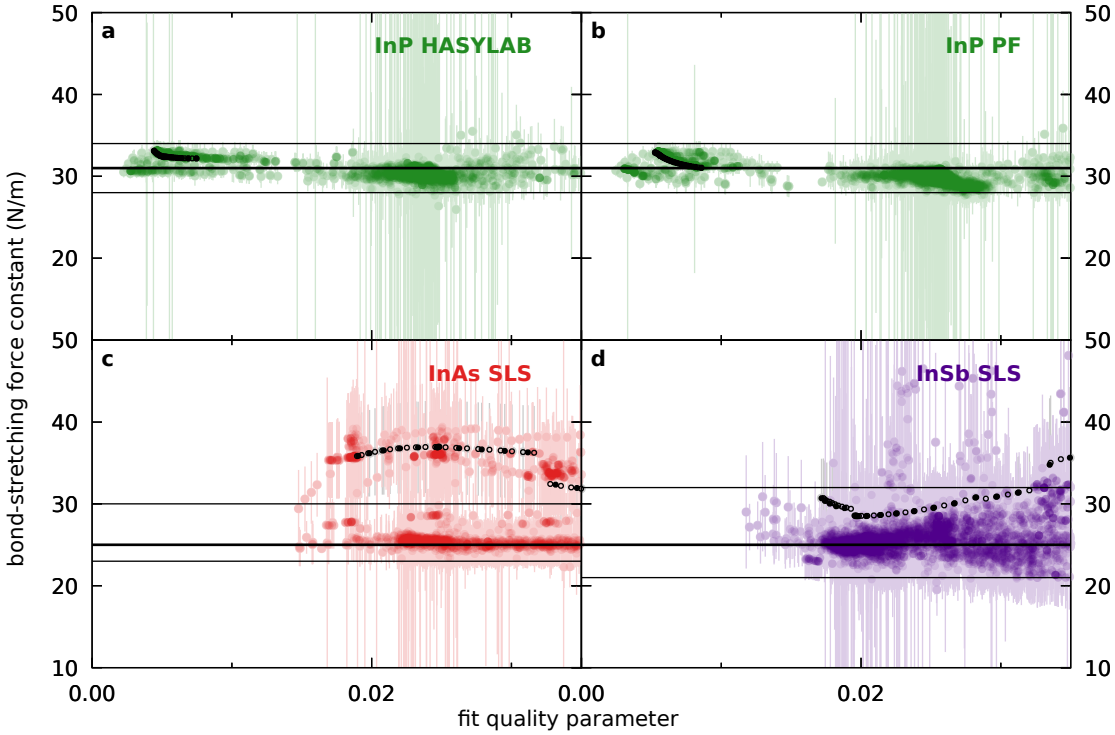

Figure C.21: Uncertainties of the 2NN stretching force constants in InP, InAs and InSb. The effective second-neighbour stretching force constants resulting from the same set of fits as in Fig. 6.2 are plotted as a function of the fit quality parameter R. The symbol description is the same as in Fig. C.16. Thick and thin black lines refer to the best, minimum and maximum force constant values given in Tab. 6.2.

C.6 Influence of over-absorption

When measuring EXAFS in fluorescence mode one should keep in mind, that large differences can occur between the measured property, i.e. the number of fluorescence photons leaving the sample, and the property one is interested in, i.e. the x-ray absorption coefficient, depending on the sample characteristics. These differences are caused by the effect, that the penetration depth differs for different x-ray absorption coefficients and is explained best for an infinitely thick and concentrated sample. In this case, the incident x-ray beam is completely absorbed in the sample and most of the absorption is caused by the element under study. The energy dependence of the x-ray absorption coefficient is then visible as an energy dependence of the mean penetration depth, since a smaller x-ray absorption coefficient is accompanied by a larger penetration depth, while a larger x-ray absorption coefficient causes a smaller penetration depth [35]. Consequently, the fluorescence radiation, on average, has to travel a differing distance in the material to reach the detector. However, the energy of the fluorescence radiation lies below the absorption edge of the material permitting most of it to escape the sample independent from the depth of creation. In the limiting case this completely conceals the fine structure [36]. In reality the fine structure is still visible albeit significantly reduced in amplitude. The over-absorption effect decreases with decreasing sample thickness and decreasing fraction of the x-ray absorption coefficient stemming from the element under study. It vanishes in the limiting cases of thin concentrated and thick diluted samples [36].

In this work, the samples for EXAFS measurements in fluorescence mode where prepared to fall in the thin concentrated case (see section 4.1), since the x-ray absorption coefficient of the graphite used for dilution is negligible at the measurement energies. However, the individual particles of the semiconductor material were shown to have sizes up to 5 μm (see section B.3) representing approximately 30 % of the absorption length for measurements at the Ga-K edge. Therefore, these individual particles do not satisfy the condition of a thin sample enabling the occurrence of over-absorption effects.

To estimate the influence of over-absorption effects on the spectra measured at SLS, the Booth algorithm [38, 144] implemented in ATHENA [124] was used to calculate the correction assuming a compact layer of GaAs or GaSb with a thickness of 5 μm. Since the sample particles diluted in the graphite matrix are mostly smaller than 5 μm (see section B.3), the real distortion should be significantly smaller than in this test case. The two samples $GaAs_{SLS}$ and $GaSb_{SLS}$ were chosen for this test, because the absorption of the sample material is higher at the Ga-K edge compared to the In-K edge. The spectra

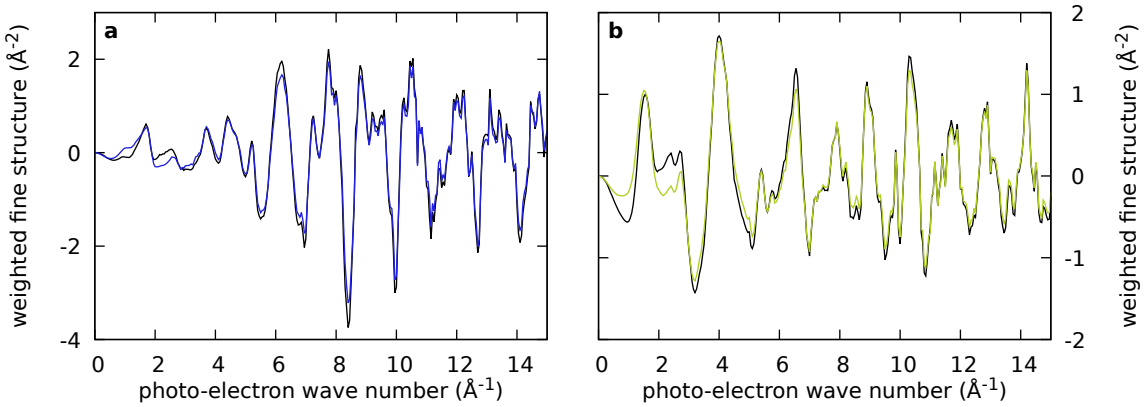

Figure C.22: Influence of the over-absorption correction. The k_e^2 weighted fine structure of GaAs (panel a) and GaSb (panel b) is plotted as a function of k_e for the corrected (black line) and uncorrected (coloured line) spectra taken at 42 K.

of these two samples are therefore most prone to distortions from over-absorption. For $GaSb_{SLS}$, very low amplitude reduction factors were determined in the fit (see discussion in section 6.1.3), hinting at a problem with over-absorption. For the test, the calibrated spectra were imported in ATHENA and corrected using the Booth algorithm. As a result, the amplitude visible in $\chi(k_e)$ and $\chi(R)$ increased by approximately 15 % consistent for all temperatures for both $GaAs_{SLS}$ and $GaSb_{SLS}$. As an example two low-temperature spectra are shown in Fig. C.22. The $\chi(k_e)$ spectra were saved and subsequently processed in the standard fitting procedure. The amplitude reduction factor determined from the corrected spectra is larger than in the standard case. With an increase from (0.85 ± 0.03) to (0.98 ± 0.04) (comparing identical fit settings) the difference is more pronounced for $GaAs_{SLS}$ compared to an increase from (0.42±0.02) to (0.48±0.03) for $GaSb_{SLS}$. All other changes of the fit results are much smaller than their respective individual fit uncertainties.

The test yields to important results: First, possible small distortions of the spectra caused by over-absorption effects are securely absorbed in the amplitude reduction factor. To make this possible, it is important, that each sample is given an individual amplitude reduction factor, as was done in both the analysis of the ternary alloy data (see section 5.2.2) and the analysis of the binary compound data (see section 6.1.2). Secondly, the very small amplitude reduction factors of $GaSb_{SLS}$ can not be explained by over-absorption effects.

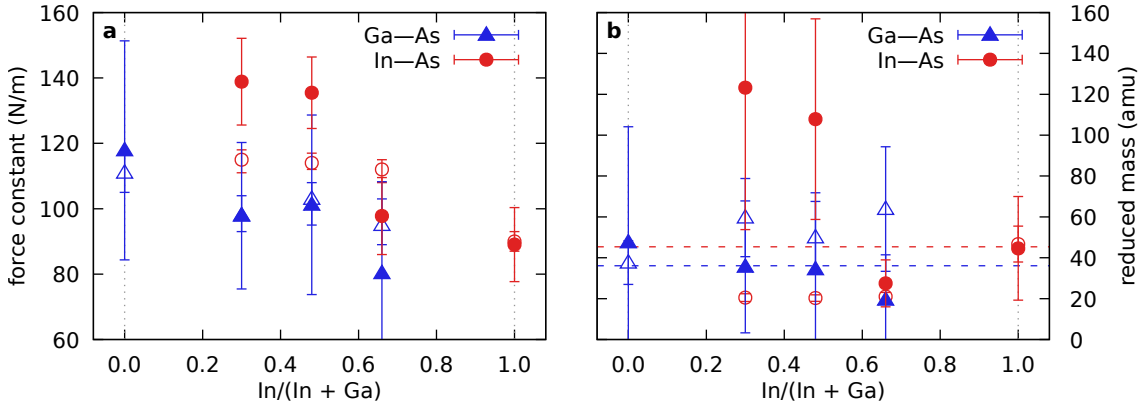

Figure C.23: Bond-stretching force constant and reduced mass of the Ga–As and In–As bonds in (In,Ga)As from fits with varying reduced mass. a, The effective bond-stretching force constants determined in fits where the reduced mass was left free to vary (solid symbols) are compared to the final results (open symbols) presented in Tab. 5.3. **b,** The reduced masses of the bonds determined from fits where the bond-stretching force constant was left free to vary (solid symbols) are compared to the fits where the bond-stretching force constants were fixed to the binary values (open symbols). The dashed lines indicate the values of an isolated bond.

C.7 Variation of the reduced mass of the bond

For the analysis of the ternary materials, it was assumed, that the reduced mass of the bond equals the value expected for an isolated bond over the whole compositional range. Since matrix effects could in principle affect also the reduced mass apparent for an embedded bond, this assumption was tested for the case of (In,Ga)As.

In Fig. C.23 the bond-stretching force constants and the reduced masses are shown as a function of composition. In both panels the results from fits where both parameters were left free are compared to values stemming from fits where the other parameter was fixed. In all the fits shown here, the static contribution to the variance was left free to vary. Setting the static contribution to zero shifts all bond-stretching force constants down by $10\,\mathrm{N\,m^{-1}}$ to $20\,\mathrm{N\,m^{-1}}$ and results in reduced masses of approximately half the values of an isolated bond.

Naturally, the introduction of an additional free parameter highly correlated with the bond-stretching force constant increases the uncertainties reported by Larch. Keeping this correlation and the large uncertainties in mind, the bond-stretching force constants determined for the binary material reproduce very well the values obtained from fits with fixed reduced mass. This indicates, that the reduced mass of an isolated bond can safely

be used in the description of the vibrational behaviour of the binary materials.

For the ternary alloys the bond-stretching force constant of the Ga–As bond is in good agreement with the results of fits with fixed reduced mass. This can also be seen in the only moderate change of the reduced mass when it is left free depicted in Fig. C.23b. In contrast, the results for the In–As bond change drastically for both the bond-stretching force constant and the reduced mass. However, the composition dependence of the In–As effective bond-stretching force constants is even more pronounced when using a freely varying reduced mass. Since the reduced masses vary significantly further than their difference between the binary materials and there is no theoretical explanation for such a pronounced compositional trend, the only reasonable approach is to fix the reduced masses in the ternary alloys to their isolated-bond values.

List of publications

Publications related to the content of this thesis

[1] S. Eckner, A. Johannes, M. Gnauck, H. Kämmer, T. Steinbach, S. Schönherr, R. Chernikov, E. Welter, M. C. Ridgway and C. S. Schnohr. "Bond-stretching force constants and vibrational frequencies in ternary zinc-blende alloys: A systematic comparison of (In,Ga)P, (In,Ga)As, and Zn(Se,Te)". *Europhys. Lett.* (accepted).

[2] S. Eckner, K. Ritter, P. Schöppe, E. Haubold, E. Eckner, J. Rensberg, R. Röder, M. C. Ridgway and C. S. Schnohr. "Bond-strength inversion in (In,Ga)As semiconductor alloys". *Phys. Rev. B* **97**, (2018), 195202.

Further publications

[3] E. Haubold, P. Schöppe, S. Eckner, S. Lehmann, I. Colantoni, F. d'Acapito, F. di Benedetto, S. Schorr and C. S. Schnohr. "Short-range versus long-range structure in Cu(In,Ga)Se_2, Cu(In,Ga)$_3Se_5$, and Cu(In,Ga)$_5Se_8$". *J. Alloy. Compd.* **774**, (2019), 803.

[4] C. S. Schnohr, S. Eckner, P. Schöppe, E. Haubold, F. d'Acapito, D. Greiner and C. A. Kaufmann. "Reversible correlation between subnanoscale structure and Cu content in coevaporated Cu(In,Ga)Se_2 thin films". *Acta Mat.* **153**, (2018), 8.

[5] P. Schöppe, C. S. Schnohr, M. Oertel, A. Kusch, A. Johannes, S. Eckner, M. Burghammer, G. Martínez-Criado, U. Reislöhner and C. Ronning. "Improved Ga grading of sequentially produced Cu(In,Ga)Se 2 solar cells studied by high resolution X-ray fluorescence". *Appl. Phys. Lett.* **106**, (2015), 013909.

[6] S. Eckner, H. Kämmer, T. Steinbach, M. Gnauck, A. Johannes, C. Stephan, S. Schorr and C. S. Schnohr. "Atomic-scale structure, cation distribution, and bandgap bowing in Cu(In,Ga)S2 and Cu(In,Ga)Se2". *Appl. Phys. Lett.* **103**, (2013), 081905.

[7] J. Sommerfeld, J. Richter, R. Niepelt, S. Kosan, T. F. Keller, K. D. Jandt and C. Ronning. "Protein adsorption on nano-scaled, rippled TiO_2 and Si surfaces". *Biointerfaces* **7**, (2012), 55.

Oral contributions at conferences

1. Bond strength inversion in (In,Ga)As
   S. Eckner, K. Ritter, Ph. Schöppe, E. Haubold, E. Eckner, Mark C. Ridgway, and Claudia S. Schnohr
   Talk at the EMRS Fall Meeting, Warshaw, Poland, 2017

2. Bond strength inversion in (In,Ga)As
   S. Eckner, K. Ritter, Ph. Schöppe, E. Haubold, S. Bauer, E. Eckner, Mark C. Ridgway, and Claudia S. Schnohr
   Talk at the DPG Spring Meeting, Dresden, Germany, 2017

3. Bond stretching force constants in (In,Ga)P
   S. Eckner, M. Gnauck, A. Johannes, H. Kämmer, T. Steinbach, Mark C. Ridgway, and Claudia S. Schnohr
   Talk at the DPG Spring Meeting, Berlin, Germany, 2015

Ehrenwörtliche Erklärung

Ich erkläre hiermit ehrenwörtlich, dass ich die vorliegende Arbeit selbständig, ohne unzulässige Hilfe Dritter und ohne Benutzung anderer als der angegebenen Hilfsmittel und Literatur angefertigt habe. Die aus anderen Quellen direkt oder indirekt übernommenen Daten und Konzepte sind unter Angabe der Quelle gekennzeichnet. Bei der Auswahl und Auswertung folgenden Materials haben mir die nachstehend aufgeführten Personen in der jeweils beschriebenen Weise unentgeltlich geholfen:

- Die (In,Ga)P und (In,Ga)As Dünnschichten wurden von H. H. Tan an der Australian National University gewachsen.
- Die SEM und EDX Messungen wurden von Sven Schönherr und Michael Oertel durchgeführt.
- Die RBS Messungen erfolgten durch Claudia Schnohr, Emanuel Schmidt und Ulrich Barth.
- Die RBS Daten wurden von Claudia Schnohr ausgewertet. Die Aufbereitung der RBS Daten zur graphischen Darstellung wurde von Jura Rensberg unterstützt.
- Die Präparation der EXAFS Proben ausgehend von den (In,Ga)P Schichten erfolgte durch Claudia Schnohr.
- Die EXAFS Proben der binären Vergleichsmaterialien GaP und InP für die HASYLAB Strahlzeiten wurden von Helena Kämmer präpariert.
- Zum erforderlichen Zeitpunkt der Probenvorbereitung für die EXAFS Strahlzeiten am SLS war mir nach Mutterschutzgesetz § 4 die Laborarbeit verboten. Deshalb erfolgte die Präparation der (In,Ga)As Proben und binären Proben GaP, GaAs, und GaSb, für die Messungen an der Ga-Kante durch Claudia Schnohr und Erik Haubold. Die Präparation der (In,Ga)As Proben, sowie der binären Proben InP, InAs, und InSb, für die Messungen an der In-Kante wurde von Erich Eckner durchgeführt.

- An den HASYLAB-Strahlzeiten waren neben mir beteiligt: Helena Kämmer, Andreas Johannes, Martin Gnauck, Tobias Steinbach, und Claudia Schnohr. Die Messungen wurden von den Beamline-Verantwortlichen Roman Chernikov und Edmund Welter unterstützt.

- An den SLS-Strahlzeiten waren neben mir beteiligt: Erik Haubold, Konrad Ritter, Sven Bauer, Philipp Schöppe, und Claudia Schnohr. Die Messungen wurden von den Beamline-Verantwortlichen Maarten Nachtegaal und Olga Safonova unterstützt.

- Die zusätzlichen EXAFS Daten binärer III-V Halbleiter wurden von Mark Ridgway (Australian National University) zur Verfügung gestellt.

Weitere Personen waren an der inhaltlich-materiellen Erstellung der vorliegenden Arbeit nicht beteiligt. Insbesondere habe ich hierfür nicht die entgeltliche Hilfe von Vermittlungs- bzw. Beratungsdiensten (Promotionsberater oder andere Personen) in Anspruch genommen. Niemand hat von mir unmittelbare oder mittelbare geldwerte Leistungen für Arbeiten erhalten, die im Zusammenhang mit dem Inhalt der vorgelegten Dissertation stehen.
Die Arbeit wurde bisher weder im In- noch im Ausland in gleicher oder ähnlicher Form einer anderen Prüfungsbehörde vorgelegt.
Die geltende Promotionsordnung der Physikalisch-Astronomischen Fakultät der Friedrich-Schiller-Universität Jena ist mir bekannt.
Ich versichere ehrenwörtlich, dass ich nach bestem Wissen die reine Wahrheit gesagt und nichts verschwiegen habe.

Jena, den 04.12.2018

_____

(Stefanie Eckner)

Danksagung

Ich möchte mich an dieser Stelle bei allen bedanken, die zum Gelingen dieser Arbeit beigetragen haben. Mein besonderer Dank gilt:

- Claudia Schnohr, für die Bereitstellung des interessanten Themas; für die Betreuung meiner Arbeit; für die Aufgaben an denen ich wachsen konnte; für die regelmäßige Erinnerung an das Wesentliche, wenn ich mich in den Details verlor; und für das Vorleben des Ideals eines guten Wissenschaftlers;
- Carsten Ronning, für die organisatorische Unterstützung meiner Arbeit und grundlegende Fragen in den Gruppenrunden;
- den Unterstützern der Strahlzeiten, für die erfolgreiche gemeinsame Arbeit;
- Jura, für die reibungslose Büropartnerschaft und die humorvolle Unterstützung (nicht nur) während der Veröffentlichungsodyssee des InGaAs-Papers;
- den Kollegen im Roten Haus, für das angenehme Arbeitsklima und angeregte Diskussionen;
- Erich, für die immerwährende Unterstützung bei der Behebung von Computerproblemen;
- den Korrekturlesern dieser Arbeit, insbesondere Jura, Anne, Stephan, und Konrad, für gestellte Fragen und hilfreiche Anmerkungen.